DISSERTATION

ON THE STRUCTURE OF CLIMATE VARIABILITY NEAR THE TROPOPAUSE AND ITS RELATIONSHIP TO EQUATORIAL PLANETARY WAVES

Submitted by

Kevin M. Grise

Department of Atmospheric Science

In partial fulfillment of the requirements

For the Degree of Doctor of Philosophy

Colorado State University

Fort Collins, Colorado

Fall 2011

Doctoral Committee:

Advisor: David W. J. Thompson

Thomas Birner
Richard E. Eykholt
David A. Randall
William J. Randel

ABSTRACT

ON THE STRUCTURE OF CLIMATE VARIABILITY NEAR THE TROPOPAUSE AND ITS RELATIONSHIP TO EQUATORIAL PLANETARY WAVES

The tropopause is an important interface in the climate system, separating the unique dynamical, chemical, and radiative regimes of the troposphere and stratosphere. Previous studies have demonstrated that the long-term mean structure and variability of the tropopause results from a complex interaction of stratospheric and tropospheric processes. This project provides new insight into the processes involved in the global tropopause region through two perspectives: 1) a high vertical resolution climatology of static stability and 2) an observational analysis of equatorial planetary waves.

High vertical resolution global positioning system radio occultation profiles are used to document fine-scale features of the global static stability field near the tropopause. Consistent with previous studies, a region of enhanced static stability, known as the tropopause inversion layer (TIL), exists in a narrow layer above the extratropical tropopause and is strongest over polar regions during summer. However, in the tropics, the TIL possesses a unique horizontally and vertically varying structure with maxima located at ~17 and ~19 km. The upper feature peaks during boreal winter and has its largest magnitude between 10º and 15º latitude in both hemispheres; the lower feature exhibits a weaker seasonal cycle and is centered at the Equator. The spatial structure of both features resembles the equatorial planetary wave response to the climatological distribution of deep convection.

Equatorial planetary waves not only dominate the climatological-mean general circulation near the tropical tropopause but also play an important role in its intraseasonal and interannual variability. The structure of the equatorial planetary waves emerges as the leading pattern of variability of the zonally asymmetric tropical atmospheric circulation. Regressions on an index of the equatorial planetary waves reveal that they are associated with a distinct pattern of equatorially symmetric climate variability characterized by variations in: 1) the distribution of convection in the deep tropics; 2) the eddy momentum flux convergence and the zonal-mean zonal wind in the tropical upper troposphere; 3) the mean meridional circulation of the tropical and subtropical troposphere; 4) temperatures in the tropical upper troposphere, the tropical lower stratosphere, and the subtropical troposphere of both hemispheres; and 5) the amplitude of the upper tropospheric anticyclones that straddle the Equator over the western tropical Pacific Ocean.

The pulsation of the equatorial planetary waves in time provides a framework for interpreting a broad range of climate phenomena. Variability in the equatorial planetary waves is associated with variability in the tropical TIL and is linked to both the El Niño-Southern Oscillation and the Madden-Julian Oscillation (MJO). Evidence is presented that suggests that the MJO can be viewed as the linear superposition of: 1) the pulsation of the equatorial planetary waves at a fixed location and 2) a propagating component. Variability in the equatorial planetary waves may also contribute to variability in troposphere/stratosphere exchange and the width of the tropical belt.

ACKNOWLEDGMENTS

The author would like to thank Dr. David W. J. Thompson of the Department of Atmospheric Science at Colorado State University for his support as my advisor and his invaluable guidance throughout this entire project; and Drs. Thomas Birner and David A. Randall of the Department of Atmospheric Science at Colorado State University, Dr. William J. Randel of the National Center for Atmospheric Research, and Dr. Richard E. Eykholt of the Department of Physics at Colorado State University for serving on the graduate advisory committee for this dissertation. Drs. Eric D. Maloney, Lorenzo M. Polvani, Rei Ueyama, John M. Wallace, and Volkmar Wirth also provided valuable comments on the research presented in this dissertation.

This material is based upon work supported under National Science Foundation grants ATM-0613082 and AGS-0936255. The material is also based in part upon the following published work, which is © Copyright 2010 American Meteorological Society (AMS) and is subject to the AMS copyright policy listed at http://www.ametsoc.org/PUBS/copyrightinfo/ams_copyright_policy_2010.pdf:

Grise, K. M., D. W. J. Thompson, and T. Birner, 2010: A global survey of static stability in the stratosphere and upper troposphere. *J. Climate*, **23**, 2275–2292.

TABLE OF CONTENTS

CHAPTER 1: INTRODUCTION AND BACKGROUND

Earth's atmosphere below ~50 km is commonly classified as two layers: the troposphere and the stratosphere. The troposphere lies directly above Earth's surface and is characterized by decreasing temperatures with altitude, low ozone and high water vapor concentrations, and rapid vertical mixing from convection and eddies. The stratosphere overlies the troposphere and is characterized by constant or increasing temperatures with altitude, high ozone and low water vapor concentrations, and relatively slow vertical motions. The boundary between the troposphere and stratosphere is known as the tropopause.

The tropopause stretches from an altitude of ~9 km in polar regions to ~17 km in the tropics and separates the distinct dynamical, chemical, and radiative regimes of the troposphere and stratosphere. Thus, the tropopause plays a crucial role in the coupling of dynamics between the troposphere and stratosphere, the exchange of chemical constituents between the two layers, and the radiative balance of Earth's atmosphere. Changes in the long-term mean behavior of the tropopause may also be an important indicator of anthropogenic climate change (e.g., Santer et al. 2003).

This dissertation encompasses a series of observational studies that describe key features and processes near the tropopause that have not been appreciated in prior literature. In this chapter, Section 1.1 briefly reviews the current understanding of why the tropopause exists and what governs its altitude. The subsequent sections then introduce a body of literature that suggests that the tropopause should not be viewed as a single level but rather as a shallow layer with both tropospheric and stratospheric properties. The relevant processes in this layer are discussed in detail, both for the extratropics (Section 1.2) and the tropics (Section 1.3). Section 1.4 concludes the chapter and presents an outline for the remainder of the dissertation.

1.1 Tropopause basics

Around the turn of the 20th Century, balloon soundings by Léon Teisserenc de Bort in Paris and Richard Assmann in Berlin indicated a layer of nearly isothermal temperatures in the upper atmosphere. These early observations were initially dismissed as measurement errors but were later published as the first evidence for the existence of a tropopause and stratosphere (see review by Hoinka 1997). It is now well known that the radiative properties of the upper atmosphere require the presence of a tropopause and stratosphere. The strong absorption of shortwave radiation by ozone in the stratosphere balances the emission of longwave radiation by carbon dioxide, ozone, and water vapor and leads to isothermal or negative lapse rates throughout the stratosphere (e.g., Manabe and Strickler 1964). (The term *lapse rate* refers to the decrease in temperatures with altitude.)

Although radiative equilibrium provides a reasonable approximation for temperatures in the stratosphere, it severely overestimates lapse rates in the troposphere, producing warmer temperatures near the surface and cooler temperatures in the upper troposphere (Figure 1.1, left). In fact, the tropospheric lapse rates associated with radiative equilibrium would be unstable to convection in the real atmosphere. Thus, tropospheric processes must act to redistribute heat from the lower troposphere to the upper troposphere to account for the observed tropospheric lapse rates. As such, Held (1982) proposed that, while stratospheric lapse rates are governed by a radiative constraint, tropospheric lapse rates must be fixed by a dynamical constraint. In this viewpoint, the tropopause is the lowest level in the atmosphere at which radiative equilibrium holds.

In the tropics, the dynamical constraint on the tropospheric lapse rate is given by moist convection. The observed tropical tropospheric lapse rate is approximately moist adiabatic (e.g., Xu and Emanuel 1989), so a radiative-convective equilibrium solution (Figure 1.1, second panel) is a reasonable approximation for the tropical troposphere. In a radiative-convective equilibrium solution, radiative warming of the surface is communicated to the atmosphere through longwave radiation, sensible heat fluxes, and latent heat fluxes. Convection then redistributes the heat vertically throughout the troposphere to reduce the tropospheric lapse rate. The convective heating of the troposphere is balanced primarily by the emission of longwave radiation by water vapor (e.g., Manabe and Strickler 1964).

In the extratropics, the dynamical constraint on the tropospheric lapse rate is less clear. Observed lapse rates in the extratropical troposphere are often less than those predicted by radiative-convective equilibrium (e.g., Schneider 2007; Figure 1.1, third panel), so the dynamical constraint for the extratropics is commonly linked to baroclinic eddies (Held 1982; Schneider 2004; Schneider 2007). Baroclinic eddies form near the surface in regions of large horizontal temperature gradients and efficiently transfer heat upward and poleward in the extratropical troposphere. For example, an early modeling study by Stone (1972) showed that the transport of heat by baroclinic eddies was sufficient to reduce the tropospheric lapse rate to realistic values. More recent modeling work has supported the role of baroclinic eddies in governing the height of the extratropical tropopause (e.g., Egger 1995; Haynes et al. 2001).

The dynamical constraint on the extratropical tropospheric lapse rate has also been linked to moist convection. Because baroclinic eddies do not preclude moist convection from forming in the extratropical troposphere, Juckes (2000) argued that sporadic moist convection in the warm sectors of baroclinic eddies is a key factor in determining extratropical tropospheric lapse rates. Subsequent modeling work by Frierson et al. (2006) and Frierson (2008) has supported the role of moist convection in governing extratropical tropospheric lapse rates.

Overall, the radiative and dynamical constraints proposed by Held (1982) provide a useful context within which to understand the height of the tropopause. However, the underlying assumption that the stratospheric lapse rates are in radiative equilibrium is not valid in the real atmosphere. In fact, the observed stratosphere is cooler than radiative equilibrium in the tropics and warmer than radiative equilibrium at high latitudes (e.g., Andrews et al. 1987). The departure of the stratosphere from radiative equilibrium is attributable to the large-scale equator-to-pole overturning circulation in the stratosphere, which is commonly referred to as the Brewer-Dobson circulation (Brewer 1949; Dobson 1956). The Brewer-Dobson circulation is characterized by rising motion and adiabatic cooling at low latitudes, poleward motion in the lower stratosphere, and sinking motion and adiabatic warming at high latitudes (Figure 1.2; see Appendix A for a review of stratospheric dynamics). Thus, the stratospheric circulation acts to raise the tropopause in the tropics and lower the tropopause at high latitudes (Kirk-Davidoff and Lindzen 2000; Thuburn and Craig 2000; Birner 2010).

The above theoretical arguments are useful in understanding the long-term mean height of the tropopause, but the observed height of the tropopause exhibits strong spatial and temporal variability with both the seasonal cycle and intraseasonal variability. Not surprisingly, the key processes that contribute to the long-term mean height of the tropopause in theoretical studies also contribute to its observed variability: moist convection in the tropics (see Section 1.3), heat fluxes by baroclinic eddies in the extratropics (Son et al. 2007), and the strength of the Brewer-Dobson circulation in both the tropics (e.g., Yulaeva et al. 1994; Highwood and Hoskins 1998; Gettelman and Forster 2002) and the extratropics (Zängl and Hoinka 2001; Son et al. 2007). But other processes are also associated with variability in the height of the tropopause. In the tropics, variability in the height of the tropopause has been linked to the quasi-biennial oscillation (QBO; e.g., Randel et al. 2000; Zhou et al. 2001), convectively coupled equatorial wave activity (e.g., Randel et al. 2003; Ratnam et al. 2006; Ryu et al. 2008; Fueglistaler et al. 2009), volcanic eruptions (Randel et al. 2000), and the Madden-Julian oscillation (MJO; Son and Lee 2007). In the extratropics, variability in the height of the tropopause has been linked to the sign of tropospheric relative vorticity (e.g., Zängl and Wirth 2002).

1.2 Extratropical upper troposphere and lower stratosphere

Within the last decade, the availability of high vertical resolution datasets has allowed studies to focus on fine-scale features surrounding the tropopause. From these studies, it has become apparent that the extratropical tropopause often behaves more as a layer rather than as a single level. Observations have shown that temperatures increase sharply with height in a narrow layer above the extratropical tropopause known as the tropopause inversion layer (TIL). Observations have also revealed that the extratropical tropopause encompasses a mixing layer (the extratropical tropopause transition layer or ExTL) with both stratospheric and tropospheric properties. Both layers are discussed below. As will be shown, the layers are not necessarily independent of one another.

1.2.1 Tropopause inversion layer (TIL)

Using high vertical resolution radiosonde data, Birner et al. (2002) and Birner (2006) identified a sharp temperature inversion in a narrow (~2 km) layer directly above the extratropical tropopause (Figure 1.1, right; see also schematic in Figure 1.2). This region of enhanced vertical temperature stratification, or static stability, is commonly referred to as the tropopause inversion layer (TIL). The TIL had not been widely recognized in prior literature because 1) averaging with respect to a tropopause-relative vertical coordinate makes it easier to distinguish the TIL (Birner et al. 2002) and 2) the TIL tends to be smeared out in reanalysis products based on data assimilation (Birner et al. 2006). More recent studies have examined the TIL using global positioning system (GPS) radio occultation temperature profiles (Randel et al. 2007a; Schmidt et al. 2010; Son et al. 2011), the interpolation of conventional radiosonde data (Bell and Geller 2008), and idealized general circulation model experiments (Son and Polvani 2007).

The existence of the TIL has important implications for the dynamical and chemical coupling between the extratropical stratosphere and troposphere. Because static stability is central to the dispersion relations for atmospheric gravity and Rossby waves, the TIL may act to inhibit atmospheric wave propagation across the extratropical tropopause (see discussion in Birner 2006) and thus could play a role in the dynamical coupling between extratropical stratospheric and tropospheric flow (e.g., Baldwin and Dunkerton 2001). The enhanced static stability of the TIL may also limit the chemical exchange between the extratropical troposphere and stratosphere to only sporadic wave-breaking events (see discussion in Birner 2006).

The physical explanation for the existence of the TIL is still subject to debate. One leading theory is that the TIL is dynamically driven. Wirth (2003) argued that 1) anticyclonic systems are associated with stronger static stability than cyclonic systems near the tropopause level and 2) anticyclonic systems dominate the zonal average because the static stability anomaly in anticyclonic systems is much stronger and sharper than the static stability anomaly in comparable cyclonic systems. Wirth and Szabo (2007) have subsequently argued that the vertical velocity convergence associated with the formation of anticyclonic systems is responsible for the TIL. However, the vertical velocity convergence associated with the Brewer-Dobson circulation may also play an important role in forcing the TIL at mid-latitudes during winter (Birner 2010). Heat fluxes by baroclinic eddies could also be a key factor in forcing the TIL (Birner 2006).

A contrasting view is that the TIL is radiatively driven. Randel et al. (2007a) hypothesized that the TIL exists because, in the lower stratosphere, radiative heating due to ozone dominates in a layer just above where radiative cooling due to water vapor is important. Subsequent studies have revealed that the radiative cooling effects of water vapor are likely more important (Kunz et al. 2009; Hegglin et al. 2009), particularly in polar regions where the seasonal cycle in the strength of the TIL is quite large (Randel and Wu 2010). These results have also shown that the enhanced static stability of the TIL coincides with a well-mixed region of both stratospheric and tropospheric properties, the ExTL (Kunz et al. 2009).

1.2.2 Extratropical tropopause transition layer (ExTL)

Observations of stratospheric tracers, such as ozone, and tropospheric tracers, such as water vapor and carbon monoxide, reveal the existence of a transition layer across the extratropical tropopause with both stratospheric and tropospheric properties. The layer is commonly referred to as the extratropical tropopause transition layer (ExTL) and extends from ~1 km below the tropopause to ~3 km above the tropopause (Hegglin et al. 2009; see also schematic in Figure 1.2).

The ExTL reflects a mixture of air from both stratospheric and tropospheric sources. Stratospheric air is transported downward by the Brewer-Dobson circulation, whereas tropospheric air is transported either quasi-horizontally (i.e., along isentropes) or vertically (i.e., across isentropes) into the tropopause region through stratosphere-troposphere exchange (Figure 1.2). Quasi-horizontal stratosphere-troposphere exchange occurs between the tropical upper troposphere and extratropical lower stratosphere and is commonly associated with synoptic-scale baroclinic disturbances (e.g., Holton et al. 1995). Vertical stratosphere-troposphere exchange involves the transport of constituents by turbulent mixing and convective processes (e.g., Hegglin et al. 2009).

As discussed in Section 1.2.1, the ExTL is not independent of the TIL because 1) mixing events on seasonal timescales are associated with high static stability values characteristic of the TIL (Kunz et al. 2009) and 2) the composition of the ExTL has important implications for the hypothesized radiative driving of the TIL (e.g., Randel et al. 2007a). However, the composition of the ExTL may also have important implications for tropospheric climate. Because of the large difference in temperatures between the tropopause and surface, small changes in the downwelling longwave radiation emitted by chemical constituents in the tropopause region can lead to strong radiative effects on surface climate (e.g., Forster and Shine 1997). The changes in downwelling longwave radiation may also force attendant changes in tropospheric dynamics (see discussion in Grise et al. 2009). Unfortunately, many of the stratosphere-troposphere exchange processes involved in determining the chemical composition of the ExTL remain highly uncertain and are an area of active research (e.g., Pan et al. 2010).

1.3 Tropical tropopause layer (TTL)

As in the extratropics (Section 1.2), the tropical tropopause is characterized by a layer with a mixture of stratospheric and tropospheric properties. This layer is commonly referred to as the tropical tropopause layer (TTL) and is often defined as stretching from the lapse rate minimum level at ~12 km to the cold point tropopause at ~17 km (Gettelman and Forster 2002; see also schematic in Figure 1.2).

The lower boundary of the TTL, the lapse rate minimum level, marks the level at which: 1) the tropical tropospheric lapse rate begins to depart from the moist adiabatic lapse rate, 2) convective outflow maximizes, and 3) radiative processes begin to take over from convective processes (Gettelman and Forster 2002). Thus, the lower boundary of the TTL is strongly tied to deep convection and is highest over deep convective regions, such as the Maritime Continent, Indian monsoon region, and South America (Gettelman and Forster 2002). However, the lower boundary of the TTL can also be defined in terms of the level of zero net radiative heating (~14 km), above which ambient air parcels ascend into the stratosphere and below which ambient air parcels descend into the troposphere (e.g., Fueglistaler et al. 2009). In this case, the lower boundary of the TTL is highly dependent upon the radiative properties of the various chemical constituents and clouds within the TTL (see Sections 1.3.2 and 1.3.3).

The upper boundary of the TTL, the cold point tropopause, marks the coldest point on the tropical temperature sounding. The cold point tropopause is a key interface in tropical stratosphere-troposphere exchange because it largely determines the concentration of water vapor entering the stratosphere (see Section 1.3.2). The cold point tropopause is influenced by a complex combination of tropospheric and stratospheric processes and is thus discussed further in Section 1.3.1.

Idealized modeling experiments are able to capture the TTL. In fact, Thuburn and Craig (2002) have argued that the separation of convective outflow from the cold point tropopause is expected from radiative-convective equilibrium as a result of the radiative properties of water vapor, carbon dioxide, and ozone within the TTL. Alternatively, Kuang and Bretherton (2004) simulated the TTL in a cloud-resolving model and concluded that it serves as an expected entrainment layer between a turbulently mixed troposphere and a stable stratosphere.

1.3.1 Cold point tropopause

The upper boundary of the TTL, the cold point tropopause, is characterized by a distinct seasonal cycle. The cold point tropopause is highest and coldest during Northern Hemisphere (NH) winter and lowest and warmest during NH summer (e.g., Highwood and Hoskins 1998; Gettelman and Forster 2002; Figure 1.3). The seasonal cycle in the cold point tropopause is accompanied by a similar seasonal cycle in tropical lower stratospheric vertical velocity (Rosenlof 1995). Because of the long radiative timescales in the tropical tropopause region, changes in vertical velocity are capable of producing large changes in temperatures, particularly on seasonal timescales (Randel et al. 2002). Thus, the seasonal cycle in cold point tropopause temperatures is commonly attributed to the seasonal cycle in upwelling near the tropical tropopause. Yet, the nature of the upwelling remains somewhat uncertain and has been a topic of much research.

Early theories for the seasonal cycle in cold point tropopause temperatures involved the seasonality in the strength of the NH branch of the Hadley circulation, which has stronger upward motion during NH winter (Reed and Vlcek 1969). Reid and Gage (1981) subsequently attributed the seasonal cycle in Hadley cell upwelling to the annual cycle in Earth's distance from the sun and the attendant changes in sea surface temperatures and tropical convection. However, due to the limited meridional extent of the Hadley circulation (equatorward of ~30º latitude), rising motion and adiabatic cooling near the tropical tropopause should be compensated by subsidence and adiabatic warming near the subtropical tropopause. This is not observed.

The prevailing theory for the seasonal cycle in cold point tropopause temperatures involves the Brewer-Dobson circulation (see Appendix A for a review of stratospheric dynamics). The Brewer-Dobson circulation is generally considered to be driven by the momentum deposition from planetary-scale Rossby wave breaking in the extratropical stratosphere. Such planetary waves are excited by topography and large-scale land-sea temperature contrast and can propagate into the stratosphere when the stratospheric zonal-mean zonal winds are weak and westerly (Charney and Drazin 1961). The momentum forcing by the planetary waves is strongest during NH winter and thus appears to drive the seasonal cycle in tropical upwelling and cold point tropopause temperatures through the "extratropical pump" of the Brewer-Dobson circulation (e.g., Yulaeva et al. 1994; Holton et al. 1995; Ueyama and Wallace 2010). Strictly speaking, the steady-state response to the extratropical wave forcing should be confined directly below the forcing in the extratropics (e.g., Haynes et al. 1991; Holton et al. 1995). Therefore, it has been argued that planetary wave breaking must occur at subtropical latitudes in order to influence the steady-state upwelling in the deep tropical lower stratosphere (Plumb and Eluszkiewicz 1999). However, the episodic nature of the wave forcing may render the steady-state solution invalid and thus permit the extratropical influence to extend into the tropics (Ueyama and Wallace 2010).

Tropical wave forcing may also influence the seasonal cycle in cold point tropopause temperatures. Several recent studies have proposed that tropical upwelling is driven, at least in part, by the eddy momentum flux convergence associated with equatorial planetary waves (Boehm and Lee 2003; Kerr-Munslow and Norton 2006; Norton 2006; Randel et al. 2008; Ryu and Lee 2010). Equatorial planetary waves are forced by the latent heat release from deep convection and are characterized by an equatorially trapped Rossby wave response to the west of the convective heating and a

Kelvin wave response to the east of the heating (e.g., Gill 1980; Highwood and Hoskins 1998; see Appendix B for a review of the relevant dynamics). In the upper troposphere, the equatorial Rossby wave pattern is tilted meridionally, such that the Rossby waves propagate out of the deep tropics and flux westerly momentum into the equatorial upper troposphere (e.g., Dima et al. 2005). Thus, from this perspective, the seasonal cycle in tropical upwelling and cold point tropopause temperatures is due not to the seasonal cycle in NH stratospheric wave breaking but rather to either the seasonal cycle in the latitude of tropical convection (Norton 2006) or the seasonal cycle in the height of the tropical convection and its associated wave response (Randel et al. 2008). To date, the exact role of equatorial planetary waves in tropical upwelling remains unresolved.

In contrast to the above studies, several theories have argued that the presence of the cold point tropopause is simply a direct response to tropical tropospheric convection. Kuang and Bretherton (2004) suggested that the presence of the cold point tropopause is expected from the cooling associated with overshooting convection in the TTL. Holloway and Neelin (2007) have alternatively proposed that divergence, rising motion, and adiabatic cooling above deep convection is required to reduce the hydrostatic pressure perturbations associated with convective heating in the troposphere.

Overall, a wide variety of tropospheric and stratospheric processes have been hypothesized to explain the long-term mean structure of the cold point tropopause. Not surprisingly, variability in cold point tropopause temperatures is similarly linked to a wide variety of processes: the QBO (e.g., Randel et al. 2000; Zhou et al. 2001), the El Niño-Southern Oscillation (ENSO; Randel et al. 2009), volcanic eruptions (Randel et al. 2000), extratropical wave driving of the Brewer-Dobson circulation (Randel et al. 2002;

Dhomse et al. 2008), the MJO (Hendon and Liebmann 1990b), and convectively coupled equatorial wave activity (Randel et al. 2003; Randel and Wu 2005; Ryu et al. 2008). The diverse processes that affect the cold point tropopause also play an integral role in tropical stratosphere-troposphere exchange.

1.3.2 Tropical stratosphere-troposphere exchange

One of the key constituents involved in tropical stratosphere-troposphere exchange is water vapor. Although methane oxidation serves as an appreciable source of water vapor in the upper stratosphere (e.g., Le Texier et al. 1988), water vapor in the lower stratosphere primarily results from transport across the tropopause. Because the TTL represents the dominant intake region of tropospheric air into the stratosphere through the upwelling branch of the Brewer-Dobson circulation (Figure 1.2), the concentration of water vapor in the lower stratosphere is largely controlled by transport across the cold point tropopause (e.g., Brewer 1949; Mote et al. 1996; Fueglistaler et al. 2009), where the cold temperatures act to "freeze-dry" the air due to the dependence of saturation vapor pressure on temperature. Thus, stratospheric water vapor concentrations are quite small (~5 ppmv) but nonetheless are a significant factor in the radiative forcing of stratospheric and surface temperatures (Forster and Shine 1999; Smith et al. 2001; Solomon et al. 2010) and in stratospheric ozone chemistry (Solomon et al. 1986).

Because water vapor concentrations in the lower stratosphere are primarily a function of the cold point tropopause temperature, tropical tropopause temperature anomalies are imparted to water vapor concentrations as they enter the stratosphere and are then advected upward by the large-scale vertical motion of the Brewer-Dobson circulation (Figure 1.3). This so-called tape recorder signal in stratospheric water vapor is observed with both the seasonal cycle (Mote et al. 1996) and interannual variability (Randel et al. 2004) in cold point tropopause temperatures. Consequently, variability in stratospheric water vapor concentrations is governed by processes similar to those that influence variability in cold point tropopause temperatures: the QBO (Geller et al. 2002; Randel et al. 2004; Fueglistaler and Haynes 2005; Fujiwara et al. 2010), ENSO (Randel et al. 2004; Fueglistaler and Haynes 2005), volcanic eruptions (Fueglistaler and Haynes 2005), and extratropical wave driving of the Brewer-Dobson circulation (Dhomse et al. 2008). The water vapor tape recorder signal is generally preserved from attenuation by mixing processes in the tropical lower stratosphere (above the TTL) due to its relative isolation from the extratropics (i.e., the so-called “tropical pipe”; Plumb 1996; see also schematic in Figure 1.2).

The relationship between the cold temperatures at the cold point tropopause and the associated small values of water vapor entering the stratosphere is well known, but the exact dehydration processes involved remain highly uncertain. Newell and Gould-Stewart (1981) suggested that the zonal-mean tropopause temperatures in the tropics are too warm to explain stratospheric water vapor concentrations and postulated the existence of a “stratospheric fountain” over the western tropical Pacific Ocean and Indian monsoon region where temperatures are cold enough to explain the observed stratospheric water vapor concentrations. Holton and Gettelman (2001) later argued that it is the quasi-horizontal processing of air parcels through the “cold trap” region of the western tropical Pacific Ocean and the subsequent slow vertical ascent by the Brewer-Dobson circulation that determines stratospheric water vapor concentrations. Subsequent air parcel trajectory simulations have supported this hypothesis (Fueglistaler et al. 2005). In contrast, other studies have suggested that the rapid dehydration of air in deep overshooting convective cloud tops in the TTL (Figure 1.2) is more important than large-scale processes (Danielsen 1982; Sherwood and Dessler 2000). Yet, overshooting convection is relatively uncommon in the TTL (e.g., Fueglistaler et al. 2009), and the evidence remains unclear as to whether it actually acts to moisten or dehydrate the TTL region (e.g., Kuang and Bretherton 2004; Corti et al. 2008; Fueglistaler et al. 2009).

Water vapor is only one of a number of key constituents that are involved in tropical stratosphere-troposphere exchange. For example, ozone has important radiative properties near the tropopause (e.g., Forster and Shine 1997), and its concentration in the tropical lower stratosphere varies strongly with the strength of tropical upwelling. Because ozone is a stratospheric tracer that is primarily produced photochemically at stratospheric levels (Jacob 1999), ozone concentrations are smallest in the tropical lower stratosphere during NH winter when the upwelling of tropospheric air by the Brewer-Dobson circulation is largest (Folkins et al. 2006; Randel et al. 2007b). In contrast, tropospheric tracers, such as carbon monoxide, exhibit much larger concentrations during periods of enhanced tropical upwelling (e.g., Randel et al. 2007b). However, convective outflow may also contribute to changes in tropospheric and stratospheric tracers in the TTL region (Folkins et al. 2006).

1.3.3 Cirrus clouds

Another key aspect of the TTL region is the presence of optically thin cirrus clouds, often referred to as subvisible cirrus (Figure 1.2). These clouds are formed from remnants of convective anvils or from homogeneous freezing and are most common above deep convective regions of the tropics (e.g., Jensen et al. 1996; Massie et al. 2002; Virts and Wallace 2010). Due to their ambient environment, the clouds contain small amounts of water and are generally less than 1 km in depth. Yet, they can stretch over hundreds of kilometers and persist on timescales of a day (e.g., Fueglistaler et al. 2009), so they may play a crucial role in the radiative budget of the climate system. The clouds are generally thought to produce a strong radiative heating effect due to their absorption of upwelling longwave radiation (e.g., Fueglistaler et al. 2009). However, when situated above optically thick convective anvils, they may instead produce a radiative cooling effect (Hartmann et al. 2001). Consequently, cirrus clouds may play an important factor in the dehydration of TTL air in the "cold trap" region (Hartmann et al. 2001; Holton and Gettelman 2001).

1.4 Outline of dissertation

The tropopause serves as a critical interface for the chemical, dynamical, and radiative coupling between the stratosphere and troposphere in both the extratropics and the tropics. As summarized in this chapter, past studies have demonstrated that 1) the long-term mean structure and variability of the tropopause results from the complex interaction of stratospheric and tropospheric processes and 2) the extratropical and tropical tropopauses can be viewed as layers consisting of both tropospheric and stratospheric properties. This dissertation provides new insight into the processes involved in the global tropopause region through two perspectives: 1) a high vertical resolution climatology of the global tropopause and the surrounding vertical temperature stratification and 2) an observational analysis of equatorial planetary waves, a key dynamical forcing in the TTL region. Chapter 2 describes the data and methods used in the dissertation. Chapter 3 then presents a global survey of the static stability in the stratosphere and upper troposphere using high vertical resolution GPS radio occultation temperature data. Given the results of Chapter 3, the remainder of the dissertation focuses on the role of equatorial planetary waves in the TTL and the broader climate system. Chapter 4 uses statistical methods to isolate the signature of equatorial planetary waves in atmospheric variability, and Chapter 5 interprets climate variability and trends within the context of the equatorial planetary waves. Chapter 6 summarizes the key findings of the dissertation and outlines future work.

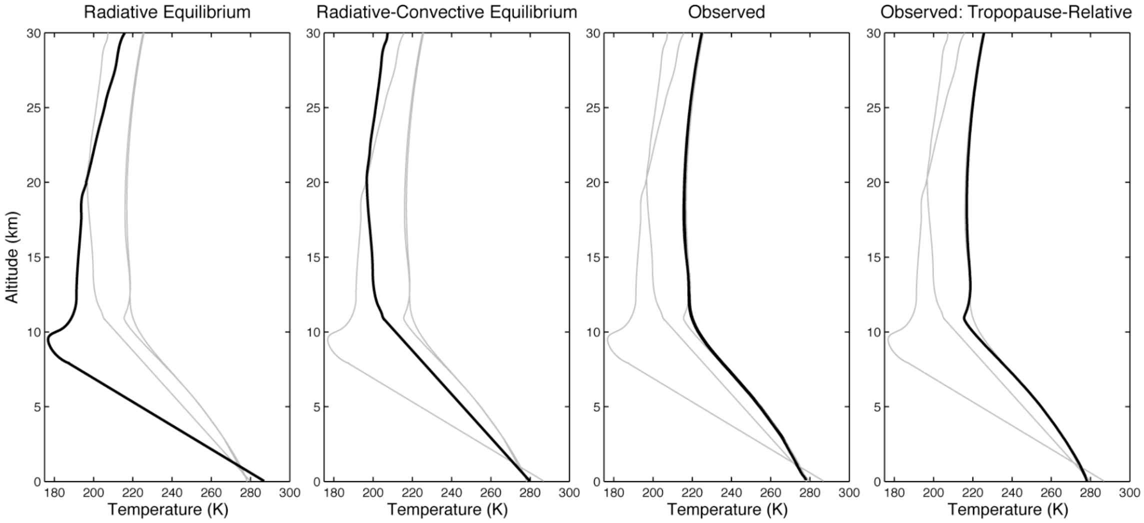

Figure 1.1: Schematic of vertical temperature profiles for the extratropics: (left panel) radiative equilibrium, (second panel) radiative-convective equilibrium with fixed tropospheric lapse rate of 6.5 K km^{-1}, (third panel) observed annual mean, and (right panel) observed annual mean in tropopause-relative vertical coordinates. The thin gray lines in each panel reproduce the temperature profiles from the other panels for comparison. The radiative and radiative-convective equilibrium profiles are adapted from Schneider (2007), and the observed temperature profiles are adapted from April 2002 – March 2008 CHAMP GPS radio occultation temperature profiles (see Section 2.1.1) at 47.5°N.

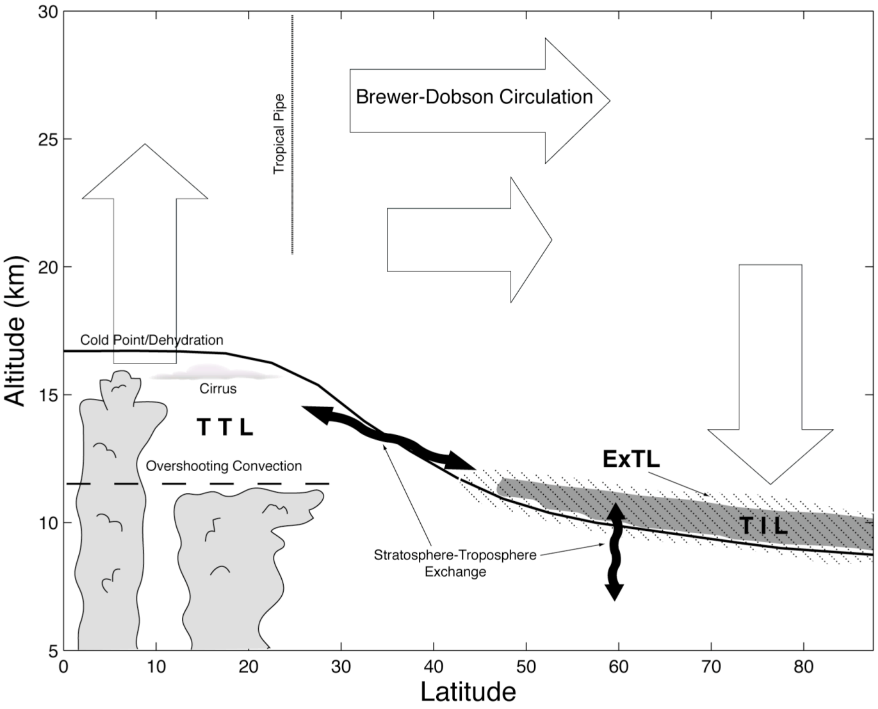

Figure 1.2: Schematic of the upper troposphere–lower stratosphere processes discussed in Chapter 1. The thick solid line represents the height of the thermal tropopause (as defined in Section 2.2.2), and the thick dashed line in the tropics represents the lapse rate minimum level. All other features are labeled in the figure. The schematic is adapted from Holton et al. (1995), Fueglistaler et al. (2009), and Pan et al. (2010).

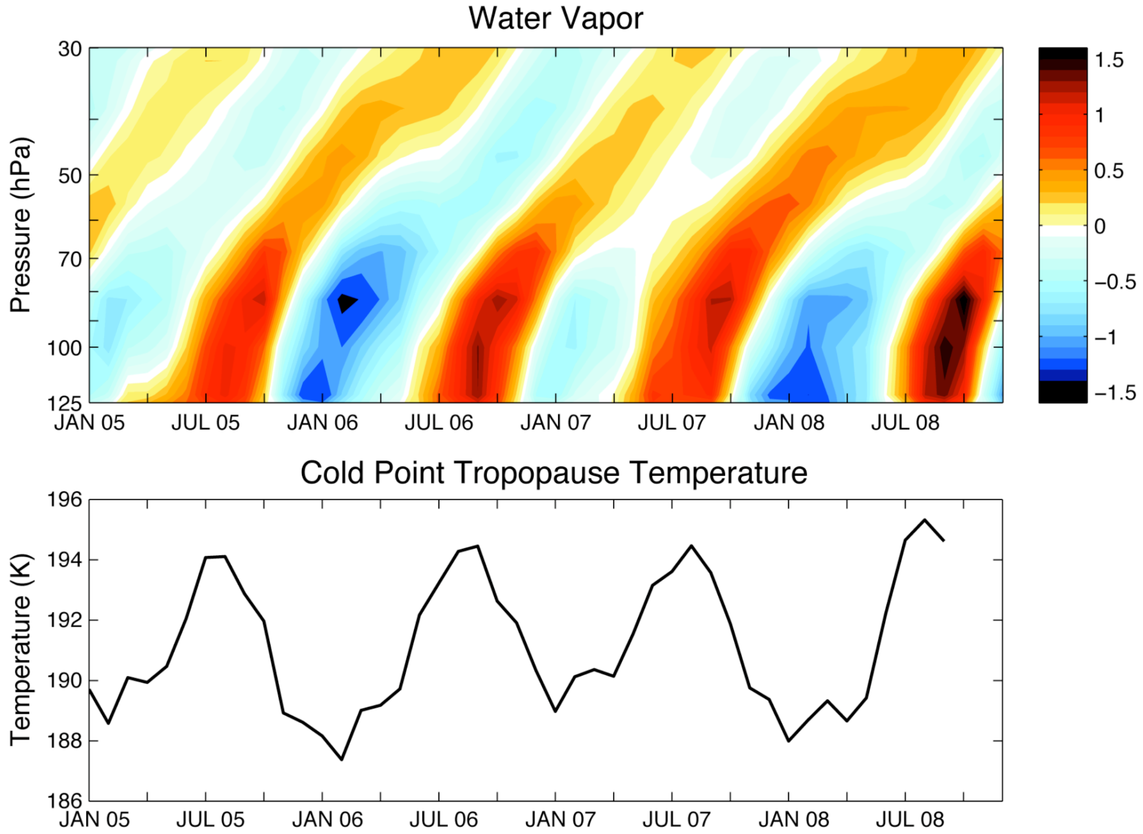

<u>Figure 1.3:</u> 2005–2008 time series of monthly-mean (top) water vapor mixing ratio averaged over 20°N–20°S and (bottom) cold point tropopause temperature averaged over 10°N–10°S. The time mean has been removed from the water vapor data, and the contour interval is 0.1 ppmv. The water vapor data are derived from Aura MLS (see Section 2.1.3), and the cold point tropopause temperatures are derived from CHAMP GPS radio occultation temperature profiles (see Section 2.1.1).

CHAPTER 2: DATA AND METHODS

2.1 Data

2.1.1 GPS radio occultation temperature profiles

The primary satellite data used in this dissertation are the GPS radio occultation temperature profiles derived from the Challenging Minisatellite Payload (CHAMP) satellite (Wickert et al. 2001). The data are freely available from the University Corporation for Atmospheric Research (UCAR)'s Constellation Observing System for Meteorology, Ionosphere, and Climate (COSMIC) program and are provided at 100-m vertical resolution from the surface to ~40 km altitude. Over the globe, approximately 200 CHAMP profiles are available per day. The data record extends from 19 May 2001 to 4 October 2008, but the number of daily profiles is much lower prior to 10 March 2002 (cf. Figure 9 of Hajj et al. 2004). Consequently, this dissertation focuses only on data for the period following 10 March 2002. The more recent COSMIC mission provides an order of magnitude increase in the number of global profiles per day (Anthes et al. 2008). The COSMIC data record, which begins in 2006, is used in Section 5.4.

The GPS temperature dataset offers the only global, high vertical resolution measurements of atmospheric temperature: select radiosondes have comparable vertical resolution but cover only a fraction of the globe; other satellite temperature products provide global coverage but have coarse vertical resolution. The GPS temperature profiles are derived using the GPS radio occultation technique. The technique uses a low-earth orbiting receiver to measure the time delay of the radio signal emitted by a GPS transmitter satellite as it passes through Earth's atmosphere. The refraction of the radio signal through the atmosphere is then used to derive the atmospheric temperature profile through an inversion method and the vertical integration of the hydrostatic equation (e.g., Kursinski et al. 1996; Hajj et al. 2004).

GPS radio occultation temperature retrievals are independent of weather conditions but are affected by water vapor. However, the biases in the GPS data due to water vapor are very small in regions where temperatures are colder than 250 K (Kursinski et al. 1996). This dissertation focuses on the GPS data between 5 km and 30 km altitude where 1) water vapor is known to have little effect on the GPS temperature retrievals and 2) the GPS temperature profiles compare well with those derived from reanalysis and radiosonde data products (e.g., Kursinski et al. 1996; Wickert et al. 2001).

2.1.2 NCEP–NCAR reanalysis

Another major data source for this dissertation is winds, geopotential heights, and temperatures from the National Centers for Environmental Prediction (NCEP) – National Center for Atmospheric Research (NCAR) reanalysis data set (Kalnay et al. 1996). The reanalysis data are obtained from the Physical Sciences Division of the National Oceanic and Atmospheric Administration (NOAA)'s Earth System Research Laboratory. The data are available from 1948 to the present and are provided in a 2.5° x 2.5° latitude-longitude grid at seventeen pressure levels ranging from 1000 hPa to 10 hPa.

The NCEP–NCAR reanalysis assimilates data from both satellite and in-situ sources within the context of a 210-km resolution climate model (Kalnay et al. 1996).

However, the reanalysis data prior to 1979 are considered to have questionable accuracy (particularly at levels above 200 hPa and at Southern Hemisphere high latitudes) due to the lack of Television Infrared Observational Satellite (TIROS) Operational Vertical Sounder (TOVS) satellite data in the reanalysis data assimilation scheme (Kalnay et al. 1996; Kistler et al. 2001). Thus, the reanalysis data used in this dissertation are truncated to the period following 1979.

2.1.3 Additional data sources

Outgoing longwave radiation (OLR) data are taken from the NOAA Interpolated OLR data set (Liebmann and Smith 1996). The data are obtained from the Physical Sciences Division of the NOAA Earth System Research Laboratory and are available from June 1974 to the present in a 2.5° x 2.5° latitude-longitude grid. The OLR data are derived from NOAA polar orbiting satellites and are processed using a spatial and temporal interpolation technique.

Sea surface temperatures are taken from the NOAA Optimal Interpolation Version 2 sea surface temperature data set (Reynolds et al. 2002). The data are obtained from the Physical Sciences Division of the NOAA Earth System Research Laboratory and are available from December 1981 to the present in a 1° x 1° latitude-longitude grid. The sea surface temperature data are derived from the interpolation of irregularly spaced ship, buoy, and Advanced Very High Resolution Radiometer satellite measurements. Passive microwave satellite measurements are also used to correct for the presence of sea ice in polar regions.

Water vapor concentrations in the stratosphere and upper troposphere are taken from the Earth Observing System Aura Microwave Limb Sounder (MLS) version 2.2 water vapor data (Lambert et al. 2007; Read et al. 2007). The data are obtained from the National Aeronautics and Space Administration Jet Propulsion Laboratory and begin in August 2004. The MLS instrument measures water vapor concentrations using naturally occurring thermal emissions from the microwave spectrum (190 GHz) and provides approximately 3500 profiles per day covering the region equatorward of 82 degrees latitude in each hemisphere. The vertical resolution of the instrument is ~3.5 km around the tropopause.

2.2 Methods

2.2.1 Definitions

Static stability is defined as (2.1), where *g* is the acceleration of gravity (9.81 m s^{-2}) and θ is the potential temperature:

$$N^2 = \frac{g}{\theta}\frac{\partial\theta}{\partial z} \tag{2.1}$$

The static stability is expressed in terms of the buoyancy frequency *N*, which measures the frequency of the vertical oscillation of an air parcel that is displaced adiabatically from an equilibrium state in a stably stratified atmosphere (e.g., Andrews et al. 1987).

Eddy kinetic energy is defined as (2.2), where *u* is the zonal wind, *v* is the meridional wind, and the asterisks represent deviations from the zonal mean.

$$\frac{1}{2}\left(u^{*2} + v^{*2}\right) \qquad (2.2)$$

The horizontal and vertical eddy momentum fluxes are similarly defined as u^*v^* and u^*w^*, where w is the vertical velocity. Both the eddy kinetic energy and eddy momentum fluxes are calculated using six-hourly NCEP–NCAR reanalysis data and then converted into daily and monthly means as required. Six-hourly data is used to compute the eddy quantities because the eddy momentum fluxes, in particular, exhibit substantial variability on timescales shorter than one day.

The mean meridional mass streamfunction is defined as (2.3), where a is Earth's radius (6.37 x 10^6 m), ϕ is the latitude, and the brackets indicate the zonal mean.

$$\frac{2\pi a \cos\phi}{g}\int_0^p [v]\,dp \qquad (2.3)$$

The values of the streamfunction are constrained to vanish at the lower boundary.

Throughout this dissertation, the term *anomaly* refers to data that have been deseasonalized and detrended so that the variance associated with the annual cycle and long-term trends does not contribute to the results. The term *standardized* refers to a time series with a mean of zero and a standard deviation of one.

2.2.2 Tropopause definitions and tropopause-relative vertical coordinates

In this dissertation, the height of the tropopause is identified using thermal criteria. The thermal tropopause is identified as the lowest level at which 1) the atmospheric lapse rate is 2 K km^{-1} or less and 2) does not exceed 2 K km^{-1} between that level and all higher levels within 2 km (WMO 1957). The tropopause can also be identified using potential vorticity (WMO 1986), isentropic potential vorticity gradients (Kunz et al. 2011), ozone (Bethan et al. 1996), or the cold point temperature (see Section 1.3.1). But these alternative criteria are not appropriate for this project because either: 1) they cannot be derived solely from the GPS temperature profiles or 2) they are not applicable globally (i.e., the potential vorticity criteria are only relevant at extratropical latitudes and the cold point criterion is only relevant in the tropics).

The results of this project derived from the GPS data are calculated in both a conventional vertical coordinate system (i.e., fixed altitude) and a tropopause-relative vertical coordinate system (e.g., Birner et al. 2002; Birner 2006). In the case of tropopause-relative coordinates, all GPS temperature profiles are shifted vertically so that the thermal tropopause for all profiles is located at a fixed value on the ordinate axis. The premise behind tropopause-relative coordinates is that the height of the tropopause fluctuates as a function of time and space (see Section 1.1), so fine-scale features near the tropopause are masked in long-term averages based on conventional altitude or pressure coordinate systems. Note that because the thermal tropopause is not easily detected during winter over Antarctica (e.g., Zängl and Hoinka 2001), results using tropopause-relative coordinates are difficult to interpret there (Tomikawa et al. 2009).

2.2.3 Linear regression analysis

Linear regression of a dependent variable x_2 on an independent variable x_1 models the relationship between the variables as a straight line:

$$\hat{x}_2 = a_1 x_1 + a_0 \tag{2.4}$$

In (2.4), $\hat{x}_2$ is the estimate of x_2 predicted from the linear regression relationship. Typically, a_0 and a_1 are chosen to minimize the square of the error between $\hat{x}_2$ and x_2. The formulas for a_0 and a_1 for this so-called linear least squares best-fit relationship are given by (2.5) and (2.6), where the overbar denotes the mean and the primes denote departures from the mean.

$$a_0 = \overline{x_2} - a_1 \overline{x_1} \tag{2.5}$$

$$a_1 = \frac{\overline{x_1' x_2'}}{\overline{x_1'^2}} \tag{2.6}$$

The regression coefficient a_1 is the ratio of the covariance between x_1 and x_2 to the variance of x_1. The regression coefficient represents the slope of the linear regression line and characterizes the amplitude of the linear relationship between x_1 and x_2.

The statistical significance of the regression coefficient a_1 is estimated by testing whether the associated linear correlation coefficient r is significantly different from zero.

$$r = \frac{\overline{x_1' x_2'}}{\sqrt{\overline{x_1'^2}}\sqrt{\overline{x_2'^2}}} \tag{2.7}$$

The correlation coefficient r is the ratio of the covariance between x_1 and x_2 to the product of the standard deviations of x_1 and x_2. The square of the correlation coefficient measures the fraction of the variance in x_2 explained by the linear regression relationship with x_1.

The statistical significance test for the correlation coefficient between two time series is performed using Student's *t*-statistic with $n^* - 2$ degrees of freedom:

$$t = r\sqrt{\frac{n^* - 2}{1 - r^2}} \tag{2.8}$$

An effective sample size n^* is used so that persistence in the data does not inflate the statistical significance of the linear relationship. n^* is estimated using the relation:

$$n^* = n\frac{1 - r_1 r_2}{1 + r_1 r_2} \tag{2.9}$$

where n is the number of samples and r_i is the lag-one autocorrelation for the time series i (Bretherton et al. 1999). The term *lag-one autocorrelation* refers to the correlation of a time series with itself at a lag of one time step. The lag-one autocorrelation serves as an effective measure of the persistence in a time series.

A useful application of linear regression analysis is the filtering of x_2 into two components: 1) a component that is linearly congruent with x_1 and 2) a component that is linearly unrelated to x_1. For example, consider x_1 and x_2 as two time series. The component of the x_2 time series that is linearly congruent with x_1 is found by multiplying the regression coefficient between x_2 and x_1 by the x_1 time series. The residual time series, the component of the x_2 time series that is linearly unrelated to x_1, is then found by subtracting the congruent time series from the full x_2 time series.

2.2.4 Empirical orthogonal function (EOF) analysis

Empirical orthogonal function (EOF) analysis is used to isolate the pattern that explains the largest possible fraction of the variance in a field of data (i.e., the so-called leading EOF or EOF 1). For example, consider a data matrix A of anomalous data (i.e., the data have been deseasonalized and detrended) with dimensions M in time by N in space. To prepare the data for EOF analysis, each element of A is weighted by 1) the square root of the cosine of the latitude (if the data contain a meridional spatial dimension) and 2) the square root of the long-term mean density (if the data contain a vertical spatial dimension). The square root weighting is applied so that the covariance matrix C is weighted by the cosine of the latitude and the long-term mean density as necessary.

$$C = \frac{1}{M} A^T A \tag{2.10}$$

The EOFs are then found by eigenanalyzing C:

$$CE = EL \tag{2.11}$$

The eigenvectors e_i of C are contained in the columns of the matrix E, and the corresponding eigenvalues λ_i are contained in the diagonal matrix L. The eigenvectors are referred to as EOFs, and the fraction of the variance explained by each EOF e_i is given by:

$$\frac{\lambda_i}{\sum_{j=1}^{N} \lambda_j} \tag{2.12}$$

By convention, EOF 1 is the spatial pattern that explains the largest possible fraction of variance in A, EOF 2 is the spatial pattern that explains the second most variance in A, and so on. Because the eigenanalysis constrains the EOFs to be orthogonal to one another, the physical significance of the spatial patterns described by the EOFs diminishes with the order of the EOF (i.e., EOF 2 is constrained to be orthogonal to EOF 1, EOF 3 is constrained to be orthogonal to both EOF 1 and EOF 2, etc.).

The statistical significance of the EOFs is assessed using the criterion of North et al. (1982), where N^* represents the number of degrees of freedom in A:

$$\Delta\lambda = \lambda\sqrt{\frac{2}{N^*}} \tag{2.13}$$

According to this criterion, an EOF e_i is considered to be significant (or "well separated" from other EOFs) if the error bounds $\Delta\lambda_i$ on its corresponding eigenvalue λ_i do not overlap with the error bounds associated with all other eigenvalues. The significance of the EOFs can also be assessed by testing whether they are reproducible in subsets of A.

The temporal evolution of each EOF pattern is defined by the associated principal component (PC) time series. The PC time series for each EOF is found by projecting the weighted data matrix A onto the associated eigenvector e_i. The resulting PC time series is typically standardized and then used as a basis in linear regression analysis.

2.2.5 Spectral analysis and temporal filtering

Spectral analysis identifies the dominant temporal frequencies that contribute to variability in a time series. To compute the power spectra shown in this dissertation, a full time series of length M is divided into subsets of length T, which overlap each other by length $T/2$. A Hanning (cosine bell) window of length T is then applied to taper the edges of the subsets. To do this, each subset is multiplied by the weighting function:

$$W(t) = \begin{cases} \dfrac{1}{T-1}\left(1 + \cos\dfrac{2\pi t}{T-1}\right) & \text{for } 0 \le |t| \le \dfrac{T-1}{2} \\ 0 & \text{for } |t| > \dfrac{T-1}{2} \end{cases} \tag{2.14}$$

The full time series is divided into subsets and weighted for the following reasons. First, the mean power spectrum derived from averaging the power spectra from subsets of a time series is more robust and reproducible than the raw power spectrum derived from the full time series alone. Second, the application of the Hanning window avoids spurious negative side lobes that appear in a power spectrum when no window (i.e., a boxcar window) is used. The length of the subsets is chosen to 1) maximize the number of degrees of freedom in the power spectrum but 2) maintain the necessary resolution to capture important spectral peaks.

The power spectrum for each subset is estimated by:

$$\Phi(k) = \begin{cases} \dfrac{C_k^{\,2}}{2} & \text{for } k = 1 \text{ to } k = (\dfrac{T}{2} - 1) \\ A_k^{\,2} & \text{for } k = \dfrac{T}{2} \end{cases} \tag{2.15}$$

where $C_k^2 = A_k^2 + B_k^2$. For a given wavenumber k, A_k and B_k are the regression coefficients for a subset of length T regressed upon $\cos(2\pi kt/T)$ and $\sin(2\pi kt/T)$ respectively, where k ranges from 1 to $T/2$ and t ranges from 1 to T. Equivalently, C_k^2 can be found using a fast Fourier transform routine. The power spectrum Φ is found for each of the subsets, and these spectra are averaged together to find a mean power spectrum. The mean power spectrum is then normalized using (2.16) such that the area under the Φ curve is one.

$$\Phi_{j,normalized} = \frac{\Phi_j}{(\Delta x)\sum_j \Phi_j} \tag{2.16}$$

Here, Δx is the interval of separation (bandwidth) between successive elements j on the abscissa of the power spectrum.

The statistical significance of a power spectrum is estimated by testing whether it is significantly different from red noise. The theoretical red noise spectrum Φ_R is given by (2.17), where τ is the e-folding timescale of the full time series and ω is the angular frequency.

$$\Phi_R(\varpi) = \frac{2\tau}{1+\tau^2\varpi^2} \tag{2.17}$$

The *e*-folding timescale is defined as $\tau = -\Delta t/(\ln r_1)$, where r_1 is the lag-one autocorrelation of the full time series and Δt is the length of a time step; the angular frequency is defined as $\omega = 2\pi k/T$ and ranges from $2\pi/T$ to π at the interval $2\pi/T$. In order to be significantly different from red noise at a particular wavenumber or frequency, a power spectrum must cross the 95% significance threshold. The threshold is equal to the red noise spectrum Φ_R multiplied by an F-statistic with M/m^* degrees of freedom for the power spectrum and infinite degrees of freedom for the red noise spectrum. Here, m^* is the number of independent spectral estimates (in this case, $T/2$).

Temporal filtering isolates select frequencies in a time series. In this dissertation, temporal filtering is conducted using the Butterworth filter. The Butterworth filter is a recursive filter:

$$g(t) = \sum_{i=0}^{K+1} a(i) f(t - i\Delta t) + \sum_{j=0}^{K+1} b(j) g(t - j\Delta t) \tag{2.18}$$

where $f(t)$ is the original unfiltered time series, $g(t)$ is the filtered time series, a is the weighting function of length K+1 for the unfiltered input, and b is the weighting function of length K+1 for the filtered input. The Butterworth filter is dependent on past values of both the unfiltered and filtered time series. Thus, it is run forward and then backward over the data to prevent an erroneous phase shift from occurring in the filtered time series. Additionally, the first and last $2K$ time steps are removed from the filtered time series because the impulse response to the Butterworth filter is not negligible at these data points.

2.2.6 Indices of climate variability

To characterize intraseasonal dynamic variability in the Northern Hemisphere extratropical stratospheric flow, an index time series is defined using the standardized leading PC time series of the NCEP–NCAR reanalysis daily-mean 10-hPa geopotential height anomalies calculated for the months of November–April between 1979 and 2008 and for the region 20°N–90°N. The PC time series describes intraseasonal variability in the strength of the stratospheric polar vortex and is referred to herein as the Northern Annular Mode (NAM) index at 10 hPa. By definition, positive values of the 10-hPa NAM index are associated with stronger-than-normal flow along 60°N, and negative values of the 10-hPa NAM index are associated with an anomalously weak stratospheric polar vortex (see also Baldwin and Dunkerton 2001). Hence, large negative values of the 10-hPa NAM index are linked to sudden stratospheric warmings (see Appendix A). The results based on the 10-hPa NAM index are not sensitive to changes in the index used to characterize stratospheric variability; virtually identical results are derived from an index based on the 10-hPa zonal-mean zonal wind at 60°N.

To characterize temporal variability in the QBO, a QBO index time series is defined using the standardized 1979–2008 NCEP–NCAR reanalysis daily-mean, zonal-mean 50-hPa zonal wind anomalies averaged over the region 20°N–20°S. By definition, the QBO index time series is positive (negative) when the 50-hPa zonal wind in the tropics is westerly (easterly).

To characterize ENSO variability, an ENSO index time series is defined using the standardized leading PC time series of monthly-mean sea surface temperature anomalies over the tropical Pacific Ocean (30ºN–30ºS, 120ºE–60ºW) (e.g., Hoerling et al. 2001). By definition, positive values of the ENSO index time series correspond to the warm phase of the ENSO cycle, with anomalously warm sea surface temperatures over the cold tongue region of the equatorial eastern Pacific Ocean.

To characterize MJO variability, paired MJO indices are obtained from the Bureau of Meteorology Research Centre of The Centre for Australian Weather and Climate Research. The MJO index time series (i.e., the so-called "real-time multivariate MJO indices," or RMM1 and RMM2) represent the first two PCs of the combined 15ºN–15ºS-averaged 850-hPa zonal wind, 200-hPa zonal wind, and OLR fields with the interannual variability removed (Wheeler and Hendon 2004).

CHAPTER 3: A GLOBAL SURVEY OF STATIC STABILITY IN THE STRATOSPHERE AND UPPER TROPOSPHERE

This chapter presents the first global survey of the vertical temperature stratification, or static stability, near the tropopause as a function of latitude, longitude, and season using high vertical resolution GPS radio occultation temperature data. Because static stability is proportional to the vertical gradient in temperature (equation 2.1), temperature data with low vertical resolution inevitably smooth – or even fail to resolve – key aspects of the static stability field. For this reason, robust but fine-scale features in the global static stability field, including the shallow but pronounced tropopause inversion layer (TIL), are most clear in high vertical resolution temperature data sets (see Section 1.2.1 for a review of the TIL).

Previous papers have documented the existence of the TIL in the extratropics in high vertical resolution radiosonde data (Birner et al. 2002; Birner 2006; Bell and Geller 2008) and GPS radio occultation data (Randel et al. 2007a). They have also described the seasonal cycle of the TIL in the extratropics (Birner 2006; Randel et al. 2007a) and have provided an example of the TIL at a single tropical radiosonde station (Bell and Geller 2008). This chapter extends previous studies by: 1) documenting and examining the seasonally, zonally, and vertically varying structure of the static stability field in the stratosphere and upper troposphere on a global scale; 2) exploring the detailed structure of near-tropopause static stability in the tropics; and 3) examining the processes that are associated with week-to-week and month-to-month variability in the strength of the TIL at tropical and polar latitudes. Subsequent studies (Schmidt et al. 2010; Son et al. 2011) have supported the key findings of this chapter.

The results of this chapter are centered around two themes. The chapter first focuses on the zonal-mean climatology of the global static stability field in the stratosphere and upper troposphere: Section 3.1 examines the annual-mean, zonal-mean climatology of static stability and discusses the sensitivity of the results to the choice of vertical coordinate system; Section 3.2 examines the seasonal cycle of the zonal-mean static stability field. The chapter then focuses on the processes associated with spatial and temporal variability in the TIL: Section 3.3 examines the longitudinal structure of the TIL; Section 3.4 identifies processes linked to weekly and monthly variability in the TIL. Conclusions are provided in Section 3.5.

3.1 The annual-mean, zonal-mean static stability field

This section documents the annual-mean, zonal-mean structure of static stability in the stratosphere and upper troposphere. The results are examined using both conventional vertical coordinates and tropopause-relative vertical coordinates.

3.1.1 Conventional vertical coordinates

The top panel in Figure 3.1 shows annual-mean, zonal-mean values of static stability in the stratosphere and upper troposphere using altitude as the vertical coordinate. The solid black line represents the annual-mean, zonal-mean height of the thermal tropopause.

The most prominent feature in the global static stability field is the abrupt vertical transition across the tropopause between tropospheric values ($N^2 \approx 1.0 \times 10^{-4}\ \mathrm{s}^{-2}$) and stratospheric values ($N^2 \approx 5.0 \times 10^{-4}\ \mathrm{s}^{-2}$) (e.g., Peixoto and Oort 1992). In the extratropics, this feature is superposed by a shallow local maximum located approximately 1–2 km above the tropopause. The local maximum represents the signature of the TIL in conventional vertical coordinates (Birner 2006). In the annual mean, the strength of the TIL is larger at Northern Hemisphere (NH) high latitudes than it is at Southern Hemisphere (SH) high latitudes because of the virtual disappearance of the TIL during SH polar winter (e.g., Tomikawa et al. 2009). (The seasonal cycle of the TIL is discussed in Section 3.2.) The extratropical static stability decreases rapidly with height just above the TIL and then slowly increases with height through the mid-stratosphere.

In the tropics, the annual-mean static stability field is characterized by three principal features: a minimum in the upper troposphere, paired off-equatorial maxima immediately above the tropopause, and a broad region of high static stability values throughout the lower and mid-stratosphere. In contrast to the extratropics, the static stability in the tropics decreases monotonically with height above the near-tropopause maxima. Several of the features in the tropical static stability field have long been established: the minimum in the tropical upper troposphere reflects the lapse rate minimum level at which tropospheric temperatures depart from the moist adiabatic lapse rate (e.g., Gettelman and Forster 2002; Fueglistaler et al. 2009; see also Section 1.3), and the high values of static stability throughout the tropical stratosphere reflect the effects of radiative heating due to ozone (e.g., Kiehl and Solomon 1986; Andrews et al. 1987;

Fueglistaler et al. 2009). But the robustness of the shallow maxima in static stability immediately above the tropopause has not been established. As demonstrated in this chapter, the paired shallow maxima in static stability above the tropical tropopause appear to be a ubiquitous feature of the tropical atmosphere.

3.1.2 Tropopause-relative vertical coordinates

The bottom panel of Figure 3.1 shows the same results as those in the top panel of Figure 3.1, but for tropopause-relative vertical coordinates (as defined in Section 2.2.2). The dominant features in the global static stability field are reproducible in both coordinate systems, including the static stability minimum in the tropical upper troposphere, the paired shallow static stability maxima in the lowermost tropical stratosphere, and the increase in static stability with height in the extratropical mid-stratosphere. The TIL is clearly evident in both coordinate systems in the extratropics, but it is generally shallower and stronger in tropopause-relative coordinates (see also Birner 2006) and is accompanied by a more clearly defined static stability minimum in the mid-latitude upper troposphere (e.g., Schmidt et al. 2010).

The most notable differences between the two coordinate systems are found in association with the TIL in the subtropics and the tropics. In the subtropics, the tropopause fluctuates between tropical and extratropical characteristics, and at certain times, the subtropics are characterized by two tropopauses (Seidel and Randel 2007). There is a hint of the TIL in the subtropics in the bottom panel of Figure 3.1, but the occasional presence of two tropopauses in this region renders results based on tropopause-relative coordinates difficult to interpret there.

In the tropics, the results based on tropopause-relative coordinates reveal that the tropical TIL exhibits a unique horizontally and vertically varying structure. To focus on the tropical TIL, the top two panels in Figure 3.2 reproduce the results from Figure 3.1, but focus on the region between 16 and 22 km. Note that the color bar in Figure 3.2 is different than that in Figure 3.1 so that the fine-scale features near the tropopause are accentuated.

In both conventional vertical coordinates and tropopause-relative coordinates, paired off-equatorial maxima in static stability are centered ~2 km above the tropopause between 10° and 15° latitude (Figure 3.2, top and middle panels). However, in tropopause-relative coordinates, the paired maxima are accompanied by a very narrow maximum in static stability that is centered at the Equator less than 1 km above the tropopause (Figure 3.2, middle). The unique structure of the tropical TIL is even more striking in vertical profiles of static stability averaged over the 10ºN – 20ºN, 5ºN – 5ºS, and 10ºS – 20ºS latitude bands (Figure 3.3, middle). Near the Equator, static stability increases rapidly above the tropopause and decreases monotonically above ~17 km. Between 10° and 20° latitude in both hemispheres, static stability also increases immediately above the tropopause (~17 km) but exhibits a second maximum at ~19 km. The meridional and vertical structure of the tropical TIL shown in the middle panels of Figures 3.2 and 3.3 is also evident in a tropopause-relative coordinate system defined with respect to the cold point tropopause instead of the thermal tropopause (Figure 3.2, bottom; Figure 3.3, right), but the shallow maximum at ~17 km is not apparent in a conventional (i.e., fixed altitude) vertical coordinate system since the height of the tropopause fluctuates in time and space (Figure 3.2, top; Figure 3.3, left). As evidenced in Figures 3.2 and 3.3, the details of the shallow static stability maximum at ~17 km change slightly depending on the definition of the tropopause used to define tropopause-relative coordinates. However, the differences are minor and have no bearing on the conclusions of this project. For this reason, only the thermal tropopause is used to define tropopause-relative coordinates throughout this dissertation.

Figure 3.1 establishes that both conventional and tropopause-relative vertical coordinates are capable of capturing key features in the long-term mean static stability field, including fine-scale features such as the TIL. However, Figure 3.1 also reveals that fine-scale features near the tropopause are accentuated in the tropopause-relative framework, particularly the magnitude of the extratropical TIL and the detailed structure of the tropical TIL. For this reason, the remainder of this chapter focuses on results based on the tropopause-relative coordinate system.

3.2 The seasonal cycle in the zonal-mean static stability field

Figure 3.4 shows meridional cross sections of zonal-mean static stability in tropopause-relative coordinates as a function of season. The black contours show the corresponding seasonal means of the zonal-mean zonal wind. Overall, the most pronounced features in the seasonal cycle of zonal-mean static stability include the following:

1. In the polar lower stratosphere, the TIL is strongest during the summer season in both hemispheres (see also Birner 2006; Randel et al. 2007a; Randel and Wu 2010).

2. In the polar mid-stratosphere, static stability peaks on the poleward flanks of the stratospheric polar night jets, particularly in the SH.
3. In the mid-latitude lower stratosphere, the TIL is deepest and most clearly defined during the winter season (see also Bell and Geller 2008).
4. In the tropical lower stratosphere, the largest values of static stability occur during the NH cold season.

The above features are evident in Figure 3.4 but are more readily apparent by dividing the data into latitude bands with similar static stability characteristics. The remainder of this section explores these and other aspects of the seasonal cycle of zonal-mean static stability by focusing on three distinct latitude bands: polar regions (60° – 90° latitude), mid-latitudes (40° – 60° latitude), and tropics (equatorward of 20° latitude). The discussion begins with the polar regions.

3.2.1 Polar regions

The top row in Figure 3.5 depicts the seasonal cycle of static stability in the NH (left) and SH (right) polar regions as a function of calendar month and altitude. Note that the abscissa is extended to 18 months so that the seasonal cycle is not truncated at the edges of the figure. The dashed line in each panel signifies the altitude of the maximum zonal-mean zonal flow within the 50° – 75° latitude band.

As documented in Birner (2006), Randel et al. (2007a), and Randel and Wu (2010), the high-latitude TIL is deepest and weakest during winter but shallowest and strongest during summer. The seasonal contrast is larger in the SH, where the TIL is nearly undetectable from July through October (see also Tomikawa et al. 2009). In both hemispheres, static stability in the polar upper troposphere is lowest during periods when static stability in the TIL is highest.

Interestingly, the tropopause exhibits a markedly different seasonal cycle in the two polar regions. In the NH polar regions, the tropopause (solid black line) is highest in summer when the TIL is strongest but lowest in winter when the TIL is weakest. In contrast, in the SH polar regions, the tropopause is lowest in summer when the TIL is strongest but highest in winter when the TIL is weakest. The out-of-phase seasonal cycles of the NH and SH polar thermal tropopauses are consistent with the climatology of the NH and SH polar dynamical (i.e., potential vorticity) tropopauses documented in Zängl and Hoinka (2001).

In the polar mid-stratosphere, the static stability is significantly larger during the cold season, particularly in the SH. The large meridional gradients in static stability in the polar mid-stratosphere (Figure 3.4) are consistent with the requirements of thermal wind balance (3.1) on the poleward flank of the westerly stratospheric polar night jet.

$$\frac{\partial u}{\partial z} \approx -\frac{g}{f\theta}\frac{\partial \theta}{\partial y} \qquad (3.1)$$

To see this more clearly, one can consider the vertical derivative of (3.1) and substitute in the definition of static stability (2.1):

$$\frac{\partial^2 u}{\partial z^2} = -\frac{1}{f}\frac{\partial}{\partial y}\left(N^2\right) \qquad (3.2)$$

(3.2) demonstrates that the meridional gradient of static stability is related to the vertical derivative of the vertical shear of the zonal wind, or equivalently to the vertical curvature of the zonal wind. For example, consider a westerly wind maximum where the vertical shear of the zonal wind is rapidly decreasing with height (i.e., changing from westerly to easterly). (3.2) mandates that a meridional gradient in static stability must exist across such a westerly wind maximum, with static stability increasing toward the pole. However, if the westerly wind maximum were barotropic or linearly changing with height, no meridional gradient in static stability would be present.

Thus, in view of (3.2), the larger meridional gradients in static stability in the SH mid-stratosphere (Figure 3.4) are consistent with the greater vertical curvature of the zonal wind profile associated with the SH stratospheric polar vortex (Figure 3.6). The descending of the region of peak static stability in the SH polar stratosphere corresponds to the seasonal breakdown of the SH stratospheric polar vortex (e.g., Hartmann 1976); as noted in Section 3.4, a similar (but opposite in sign) signal in static stability is found in association with sudden stratospheric warmings.

3.2.2 Mid-latitudes

The middle row in Figure 3.5 documents the seasonal cycle of static stability averaged over the NH (left) and SH (right) mid-latitudes. In contrast to the polar regions, the TIL exhibits a weak seasonal cycle when averaged over the 40° – 60° latitude band (see also Randel et al. 2007a). The reasons for the weak seasonal cycle in Figure 3.5 (middle row) are evidenced in Figure 3.4. During the winter season, the mid-latitude TIL is relatively weak but extends throughout the 40° – 60° latitude band. In contrast, during the summer season, the TIL has large amplitude on the poleward edge of the 40° – 60° latitude band but is poorly defined on the equatorward edge of the 40° – 60° latitude band. Hence, when averaged over the mid-latitudes, the summertime and wintertime magnitudes of the TIL are comparable.

In the mid-latitude mid-stratosphere, the static stability is strongest during the summer season, again in contrast to the seasonal cycle in the polar regions. The seasonal cycle in static stability in the mid-latitude mid-stratosphere is consistent with: 1) the extension of the region of high static stability from the tropics into the mid-latitudes during summer (Figure 3.4); 2) the enhanced radiative heating due to ozone in the mid-latitude stratosphere during summer (e.g., Kiehl and Solomon 1986; Andrews et al. 1987); and 3) the requirements of thermal wind balance on the equatorward flank of the westerly stratospheric polar night jet during winter (equation 3.2; Figure 3.6).

3.2.3 Tropics

Figures 3.4 and 3.5 (bottom row) display the seasonal cycle of static stability in the tropics. As noted in Section 3.1, the most interesting features in static stability in the tropics are found in the vicinity of the tropopause. Hence in Figures 3.7 and 3.8, the results from Figures 3.4 and Figure 3.5 (bottom row) are reproduced to focus on the region between 16 and 22 km. To demonstrate the meridional structure of the tropical features, Figure 3.8 divides the tropics into three latitude bands in which unique static stability structures are evident in the annual mean (see Figures 3.1–3.3): 10°N – 20°N (top panel), 5°N – 5°S (middle panel), and 10°S – 20°S (bottom panel). Note that the color bars in Figures 3.7 and 3.8 are different than those in Figures 3.4 and 3.5 so that the fine-scale features near the tropopause are accentuated.

Figures 3.7 and 3.8 confirm the existence of two distinct features in the tropical TIL: a narrow maximum centered at ~17 km and a broader maximum centered at ~19 km. The narrow static stability maximum centered at ~17 km is strongest in the 5°N – 5°S latitude band (Figure 3.8, middle) and weakly peaks during NH winter. The narrow maximum is weaker in the 10° – 20° latitude bands and peaks during the summer season. The broader static stability maximum near 19 km is more distinct poleward of 10° latitude and peaks during the NH cold season in both hemispheres. The seasonal cycle in static stability at 19 km is consistent with the large amplitude of the seasonal cycles in temperature and ozone over the 16 – 19 km altitude range (Randel et al. 2007b; see Section 1.3), but the existence of the equatorially centered feature near 17 km has not been previously documented. Both features are examined in further detail in the next section.

3.3 Longitudinal structure of near-tropopause static stability

The remainder of this chapter focuses on the zonally and temporally varying aspects of the region of enhanced static stability immediately above the tropopause (i.e., the TIL). This region is examined for several reasons. First, the structure of static stability in the mid-stratosphere has been extensively documented and is consistent with 1) stratospheric radiative heating rates (e.g., Kiehl and Solomon 1986) and 2) the collocation of large temperature gradients and the stratospheric polar vortex. In contrast, the TIL has only recently been recognized in the literature (Birner et al. 2002; Birner

2006), and the mechanisms that drive the TIL are still under investigation. Additionally, the TIL may play a key role in determining both chemical transport and dynamical coupling across the tropopause (see Section 1.2), and it has not been examined in detail in the tropics. This section examines the longitudinal structure of the TIL; the following section examines the dominant forms of weekly and monthly variability that are associated with fluctuations in the magnitude of the TIL.

Figure 3.9 shows global, seasonal-mean maps of static stability averaged over a 1-km layer above the tropopause. The panels thus capture the magnitude of the TIL as a function of latitude, longitude, and season. The dominant features in Figure 3.9 are the meridional gradients in the strength of the TIL between tropical, middle, and polar latitudes. During all seasons, the magnitude of the TIL drops rapidly from tropical to mid-latitudes. In general, the largest meridional gradients in the strength of the TIL are collocated with the flanks of the subtropical jet (Figure 3.9, black contours). During the summer months, the TIL increases in strength from mid- to polar latitudes, with higher values of static stability found in the NH polar regions than in the SH polar regions. In fact, the magnitude of the TIL over the NH polar regions during summer is comparable to that found in certain regions of the tropics (Figure 3.9, top right). During the winter months, the extratropical TIL peaks at mid-latitudes over the northeast Pacific and North Atlantic Oceans in the NH (Figure 3.9, top left), and at nearly all longitudes along ~45 degrees latitude in the SH (Figure 3.9, top right). In the SH, the structure of the wintertime TIL persists into the spring months, particularly at longitudes near New Zealand (Figure 3.9, bottom right). The mid-latitude features in Figure 3.9 are evident throughout the 3-km layer above the tropopause, except for the North Atlantic feature, which is primarily limited to the ~1 km layer above the tropopause (not shown).

The zonal asymmetry of the TIL is most pronounced in the tropics. As highlighted in previous sections, the near-tropopause static stability in the tropics is characterized by two distinct features located at ~17 km and ~19 km (~0–1 km and ~1–3 km above the tropopause). Figure 3.10 shows the same results as those shown in Figure 3.9, but it is focused on these tropical features. Note that the color scale in Figure 3.10 is different than that used in Figure 3.9 to accentuate the zonal structure of the results. As also evidenced in Figures 3.1–3.4 and Figures 3.7–3.8, the tropical static stability maximum located ~0–1 km above the tropopause is centered about the Equator (left panels in Figure 3.10), whereas the static stability maximum located ~1–3 km above the tropopause is centered between 10° and 20° latitude in both hemispheres (right panels in Figure 3.10).

The horizontal distribution of the 0–1 km static stability maximum (Figure 3.10, left column) is consistent with the structure of cold point tropopause temperatures (e.g., Highwood and Hoskins 1998; Randel et al. 2003; Gettelman and Birner 2007; Fueglistaler et al. 2009). The largest static stability values in the 0–1 km layer occur in regions where the cold point tropopause temperatures are coldest (Figure 3.11, left column). Interestingly, the vertical depth and horizontal distribution of the 0–1 km static stability maximum are also reminiscent of the thin cirrus clouds that are observed near the tropical tropopause (see Section 1.3.3; cf. Figure 4 of Virts and Wallace 2010).

Both the 0–1 km and 1–3 km static stability maxima resemble the quasi-stationary equatorial Rossby and Kelvin wave responses to the diabatic heating associated with the climatological distribution of deep convection (e.g., Gill 1980; Highwood and Hoskins 1998; Dima and Wallace 2007; Fueglistaler et al. 2009; see also Appendix B). The largest static stability values in the 1–3 km layer (Figure 3.10, right column) occur in regions characterized by anticyclones in the upper tropospheric geopotential height field (Figure 3.11, right column). Thus, the results in Figures 3.10 and 3.11 suggest that equatorial planetary waves likely play a central role in determining the unique horizontally and vertically varying structure of the tropical TIL. However, establishing the exact relationship between equatorial planetary waves and the static stability features in the tropical TIL requires a more detailed understanding of equatorial planetary waves and their role in the climate system (see Chapters 4 and 5).

3.4 Stratospheric processes associated with variability in the TIL

This section examines the processes that are associated with weekly and monthly variability in the strength of the TIL at polar and tropical latitudes. To do this, an index of the strength of the TIL is created by averaging static stability over the depth of the TIL in each region. Because of the limited spatial and temporal sampling of the CHAMP data, the TIL index time series are based on five-day averaged data only. Results in this section focus on polar and tropical latitudes since the TIL is most robust in those regions (Figure 3.1, bottom).

Figure 3.12 shows plots of the TIL index time series as a function of calendar day based on the layer 0–1 km above the tropopause at polar latitudes, and on the layers 0–1 km and 1–3 km above the tropopause at tropical latitudes. Consistent with Sections 3.1 and 3.2, the amplitude of the seasonal cycle of the TIL is largest in the polar regions, with peak values found during the summer seasons. Interestingly, the year-to-year variance in the polar TIL peaks during winter and summer in the NH, and during spring and summer in the SH. The TIL exhibits a weak variance minimum during the NH fall season in the tropics. The nature of the variance in the TIL index time series for both the polar regions and the tropics is explored below.

3.4.1 Polar regions

The top panel in Figure 3.13 shows the regressions of the five-day-mean CHAMP static stability anomalies (averaged over 60°N – 90°N) upon wintertime values of the NH TIL index time series from Figure 3.12. The index is standardized, and the seasonal cycle is removed prior to calculating the regression coefficients. As evidenced in Figure 3.13 (top), positive anomalies in the strength of the NH polar TIL are associated with oppositely signed static stability anomalies that descend through the mid-stratosphere. The descending static stability anomalies in the mid-stratosphere are reminiscent of wave-driven variability in the NH stratospheric polar vortex (see Appendix A for a review of stratospheric dynamics). To isolate the anomalous static stability signature associated with stratospheric wave-driven variability, the middle panel of Figure 3.13 shows analogous regressions but for static stability regressed on the inverted five-day-mean 10-hPa Northern Annular Mode (NAM) index time series (the 10-hPa NAM index time series has been inverted (i.e., multiplied by –1) so that the signs of the regression coefficients correspond to a sudden stratospheric warming event). For reference, the bottom panel of Figure 3.13 shows the corresponding zonal wind anomalies (averaged over 50°N – 75°N) regressed on the inverted five-day-mean 10-hPa NAM index time series.

Together, the results in all panels of Figure 3.13 reveal that the magnitude of the NH polar TIL is significantly linked to variability in the NH stratospheric polar vortex, with increased static stability in the vicinity of the TIL found during the period immediately following weakenings of the NH stratospheric polar vortex. Hence, whereas radiative processes may play a role in establishing the existence of the TIL (Randel et al. 2007a; Kunz et al. 2009; Hegglin et al. 2009; Randel and Wu 2010), dynamic variability in the NH polar stratosphere appears to contribute to intraseasonal variability in the strength of the NH winter polar TIL. Note that sudden stratospheric warmings are by construction associated with descending static stability anomalies along the lower edge of the stratospheric warming. However, the results shown here illustrate that they are also associated with a rapid sharpening of static stability immediately above the tropopause. Interestingly, the shallow maximum in near-tropopause static stability coincides with the period after a sudden stratospheric warming when coupling between the extratropical stratospheric and tropospheric zonal flow is often observed (e.g., Baldwin and Dunkerton 2001; see Section 3.5 for further discussion).

A similar relationship between the strength of the TIL and stratospheric dynamic variability is also evidenced in the SH polar regions. Because the SH stratospheric polar vortex is more quiescent than its NH counterpart (see Appendix A), two case studies are used to hint at the importance of stratospheric dynamic variability on the SH polar TIL. The first case study is spring 2002, when the SH stratospheric polar vortex experienced an unprecedented sudden stratospheric warming (Shepherd et al. 2005); the second case study is spring 2006, when the SH polar vortex was anomalously strong. Figure 3.14 shows five-day-mean time series of the static stability field (averaged over 60°S – 90°S) during SH spring for both of these cases. As in Figure 3.5 (top row), the dashed line in each panel denotes the altitude at which the mid-latitude jet is maximized. The anecdotal evidence in Figure 3.14 clearly reveals that a narrow TIL formed following the sudden stratospheric warming in 2002 (Figure 3.14, top) but not during the quiescent spring of 2006 (Figure 3.14, bottom), despite the presence of large mid-stratospheric static stability values within the strong polar vortex of 2006. Additionally, note that the earlier seasonal breakdown of the SH stratospheric polar vortex in 2002 coincided with an anomalously strong TIL during early SH summer.

The results in Figures 3.13 and 3.14 demonstrate marked covariability between stratospheric dynamical (i.e., wave-driven) processes and intraseasonal variability in the strength of the polar TIL during the NH winter and SH spring seasons. The results thus suggest that stratospheric dynamical processes give rise to the peak in variance in the polar TIL during those seasons (Figure 3.12). Similar analyses were conducted to examine the dynamical processes associated with the summertime variance maxima in the NH and SH polar TIL. However, no coherent dynamical structures in either the extratropical troposphere or stratosphere were clearly linked to variability in the strength of the polar TIL during the summer months (not shown).

3.4.2 Tropics

Figure 3.15 examines analogous relationships for the tropical TIL. The top left panel shows the regressions of the five-day mean CHAMP static stability anomalies (averaged over 20°N – 20°S) upon the 1–3 km tropical TIL index time series from Figure 3.12. The index is standardized, and the seasonal cycle is removed prior to calculating the regression coefficients. Figure 3.15 (top left) demonstrates that variability in static stability in the layer 1–3 km above the tropical tropopause is linked to descending static stability anomalies in the tropical mid-stratosphere that have a timescale reminiscent of that associated with the quasi-biennial oscillation (QBO; Baldwin et al. 2001). The sign of the results is such that positive static stability anomalies in the layer 1–3 km above the tropical tropopause are preceded by descending positive static stability anomalies in the tropical mid-stratosphere, and vice versa. Interestingly, regressions based on the 0–1 km tropical TIL index time series (Figure 3.15, top right) are less clearly linked to QBO-like static stability anomalies in the tropical mid-stratosphere.

The above results suggest that variability in static stability in the layer 1–3 km above the tropical tropopause is linked to the QBO. To test this, Figure 3.15 (bottom left) shows results formed by regressing static stability onto the inverted five-day-mean QBO index time series. For reference, Figure 3.15 (bottom right) shows the corresponding equatorial zonal wind anomalies regressed on the inverted five-day-mean QBO index time series. The descending static stability anomalies in the mid-stratosphere in Figure 3.15 (bottom left) correspond to the descending warm and cold temperature anomalies that are in thermal wind balance with the zonal wind anomalies in Figure 3.15 (bottom right). As the QBO decays toward the tropopause, the associated static stability anomalies disappear at ~20 km and then strengthen considerably in a narrow layer immediately above the tropopause.

Overall, the results in Figure 3.15 reveal that static stability anomalies in the layer 1–3 km above the tropical tropopause are significantly linked to QBO-driven variability in the tropical mid-stratosphere, with enhanced static stability near the tropical tropopause following the easterly phase of the QBO. Past studies have noted that the easterly phase of the QBO is associated with a cooler and higher tropical tropopause (e.g., Randel et al. 2000; Zhou et al. 2001), and Ratnam et al. (2006) has argued that the tropical tropopause is sharper during the easterly phase of the QBO in the lowermost stratosphere. The results shown here support these previous findings but also highlight the fine-scale nature of the linkages between the QBO and static stability in the lowermost tropical stratosphere: the QBO projects strongly onto static stability in the layer 1–3 km above the tropical tropopause but only weakly onto static stability in the layer 0–1 km above the tropical tropopause.

3.5 Conclusions

Static stability is a fundamental dynamical quantity, particularly for the propagation of atmospheric wave activity. In the long-term mean, the most pronounced feature in the global static stability field is the transition from low values in the troposphere to relatively high values in the stratosphere. In the extratropics, this pattern is accompanied by: 1) a broad static stability maximum in the polar mid-stratosphere and 2) a shallow static stability maximum in the region immediately above the tropopause (Figures 3.1 and 3.4). The large meridional gradients in static stability in the polar mid-stratosphere peak during the cold season (Figures 3.4 and 3.5) and are in thermal wind balance with the stratospheric polar night jet. Hence, they are most pronounced in the SH during winter and descend through the polar stratosphere during spring as the stratospheric vortex breaks down (Figures 3.4 and 3.5). The extratropical shallow static stability maximum reflects the signature of the TIL. As noted in Birner (2006) and Randel et al. (2007a), the TIL is deepest during the cold seasons at mid-latitudes but is strongest during the warm seasons at polar latitudes.

In the tropics, the static stability field is marked by four primary features: 1) a static stability minimum in the upper troposphere, 2) a very shallow static stability maximum centered at the Equator ~0–1 km above the tropopause, 3) paired static stability maxima in the lower stratosphere centered between 10° and 20° latitude in both hemispheres and located ~1–3 km above the tropopause, and 4) a broad region of high static stability values (much higher than those at comparable altitudes in the extratropics) that extend from the tropopause to ~25 km. The upper-tropospheric static stability minimum reflects the change in tropospheric lapse rate near the top of tropical convection (e.g., Gettelman and Forster 2002), and the broad region of high static stability values in the mid-stratosphere is consistent with radiative heating due to ozone (e.g., Kiehl and Solomon 1986; Andrews et al. 1987). But the unique vertically and horizontally varying structure of the static stability field in the vicinity of the tropical tropopause (i.e., the tropical TIL) has not been appreciated in previous studies (e.g., the recent review of the tropical tropopause layer by Fueglistaler et al. (2009) suggests that tropical static stability exhibits a single maximum near 70 hPa).

The fine-scale features in the static stability field in the vicinity of the tropical tropopause are robust. The static stability features centered ~0–1 km and ~1–3 km above the tropical tropopause are reproducible in analyses based on the cold point tropopause

(Figure 3.2, bottom; Figure 3.3, right), they are consistent with the profile of static stability at Yap Island (located at 9°N) presented in Bell and Geller (2008), and they are evidenced in summertime averages of static stability based on high vertical resolution radiosonde data in the NH subtropics (cf. left edge of Fig. 7a (right) of Birner 2006). Both features also exhibit physically meaningful horizontal structures. The lower feature bears resemblance to the patterns of cold point temperatures (e.g., Highwood and Hoskins 1998; Figure 3.11, left column) and tropical tropopause layer cirrus (e.g., Virts and Wallace 2010), and both the lower and upper features are reminiscent of the planetary wave response to the diabatic heating associated with the climatological distribution of tropical convection (e.g., Dima and Wallace 2007; Figure 3.11, right column). Interestingly, the static stability feature located ~0–1 km above the tropical tropopause is stronger during the NH cold season at the Equator, but it peaks during the summer season between 10° and 20° latitude in each hemisphere (Figures 3.8 and 3.10). In contrast, the static stability feature located ~1–3 km above the tropical tropopause peaks during the NH cold season throughout the tropics (Figures 3.8 and 3.10).

The fine-scale static stability features near the tropopause also exhibit substantial variability. In polar regions, the TIL exhibits enhanced variance during the winter and summer seasons in the NH, and during the spring and summer seasons in the SH. The variance maxima during NH winter and SH spring coincide with the “active” seasons for stratosphere–troposphere coupling, and during these seasons the strength of the TIL is coupled to stratospheric dynamic variability (i.e., periods following a weakening of the stratospheric polar vortex are marked by an anomalously strong TIL, and vice versa). The variance maxima during the summer seasons are not linked to any obvious patterns of large-scale atmospheric variability. In the tropics, the amplitude of the static stability feature located ~1–3 km above the tropopause varies in association with the QBO, consistent with the juxtaposition of warm over cold temperature anomalies as the easterly phase of the QBO descends through the lowermost stratosphere. The narrow tropical TIL feature located ~0–1 km above the tropopause is not as clearly linked to the QBO.

There are two prevailing mechanisms thought to give rise to the TIL. Wirth (2003) and Wirth and Szabo (2007) argue that the TIL reflects the effects of sharp static stability gradients above tropospheric anticyclones. In contrast, Randel et al. (2007a), Kunz et al. (2009), Hegglin et al. (2009), and Randel and Wu (2010) argue that the TIL is driven, at least in part, by the radiative cooling due to water vapor near the tropopause.

The results in this chapter suggest that a much broader range of processes govern the existence and variability of the TIL. The dynamical hypothesis proposed by Wirth (2003) applies only to extratropical latitudes, and the radiative hypothesis proposed by Randel et al. (2007a) does not explain the unique structure of the TIL at tropical latitudes. The amplification of the polar TIL during sudden stratospheric warmings occurs on timescales shorter than the radiative timescale near the tropopause and suggests that the extratropical TIL is sensitive to stratospheric dynamics (see also Birner 2010). The horizontal structure of the tropical TIL suggests that it owes its existence at least in part to the planetary waves associated with tropical convection (see also Section 5.4). Hence, the results presented here reveal that the TIL likely arises from a suite of radiative and dynamical processes operating at both stratospheric and tropospheric levels.

The structure and variability of the TIL documented here could be important in the context of stratosphere–troposphere dynamical coupling and chemical exchange. A much larger vertical gradient in static stability above the tropopause following a sudden stratospheric warming could affect the vertical propagation of tropospheric eddies, and thus could contribute to the changes in the tropospheric circulation observed in association with stratosphere–troposphere coupling (Baldwin and Dunkerton 2001). In fact, Simpson et al. (2009) have recently demonstrated the importance of the vertical distribution of static stability near the tropopause in determining the upper-tropospheric eddy momentum flux anomalies in an idealized general circulation model. The sharp gradients in static stability immediately above the tropical tropopause may also play a key role in the propagation of tropical waves and in the exchange of air between the tropical troposphere and stratosphere. The importance of the narrow-scale features in near-tropopause static stability for stratosphere–troposphere coupling and exchange has yet to be determined (see proposed work in Sections 6.2.1 and 6.2.2).

In the remainder of this dissertation, the results focus on one of the key features identified in this chapter: equatorial planetary waves. The following two chapters isolate equatorial planetary waves in atmospheric variability and then link variability in the equatorial planetary wave amplitudes to structures in the tropical TIL and the broader general circulation.

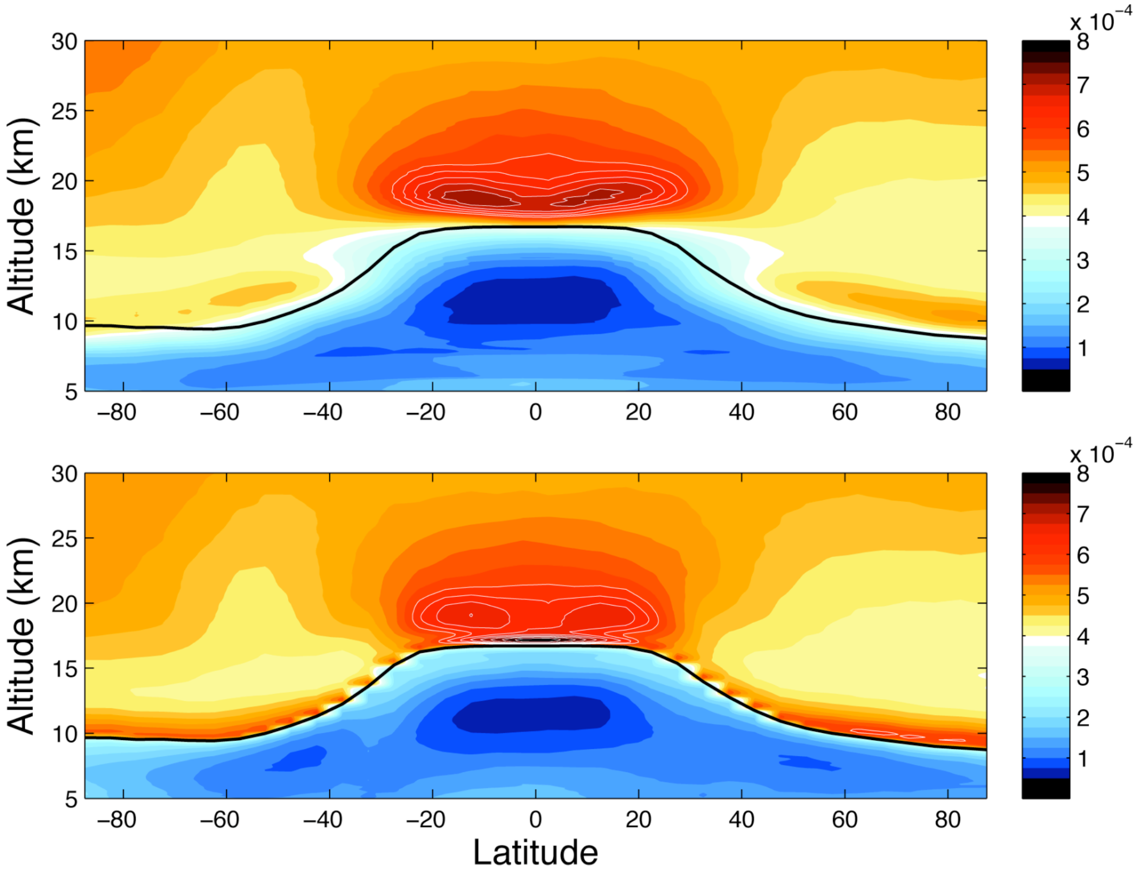

Figure 3.1: Annual-mean, zonal-mean static stability (N^2) in (top panel) conventional vertical coordinates and (bottom panel) tropopause-relative vertical coordinates. The shading interval is 2.5 x 10^{-5} s^{-2}. The thick solid black line is the annual-mean, zonal-mean thermal tropopause height. The thin white contours highlight the shading intervals for values greater than or equal to 6.0 x 10^{-4} s^{-2}. The annual mean is based on data averaged over April 2002 – March 2008. In all figures in this chapter, static stability is calculated using the GPS temperature profiles from the CHAMP satellite.

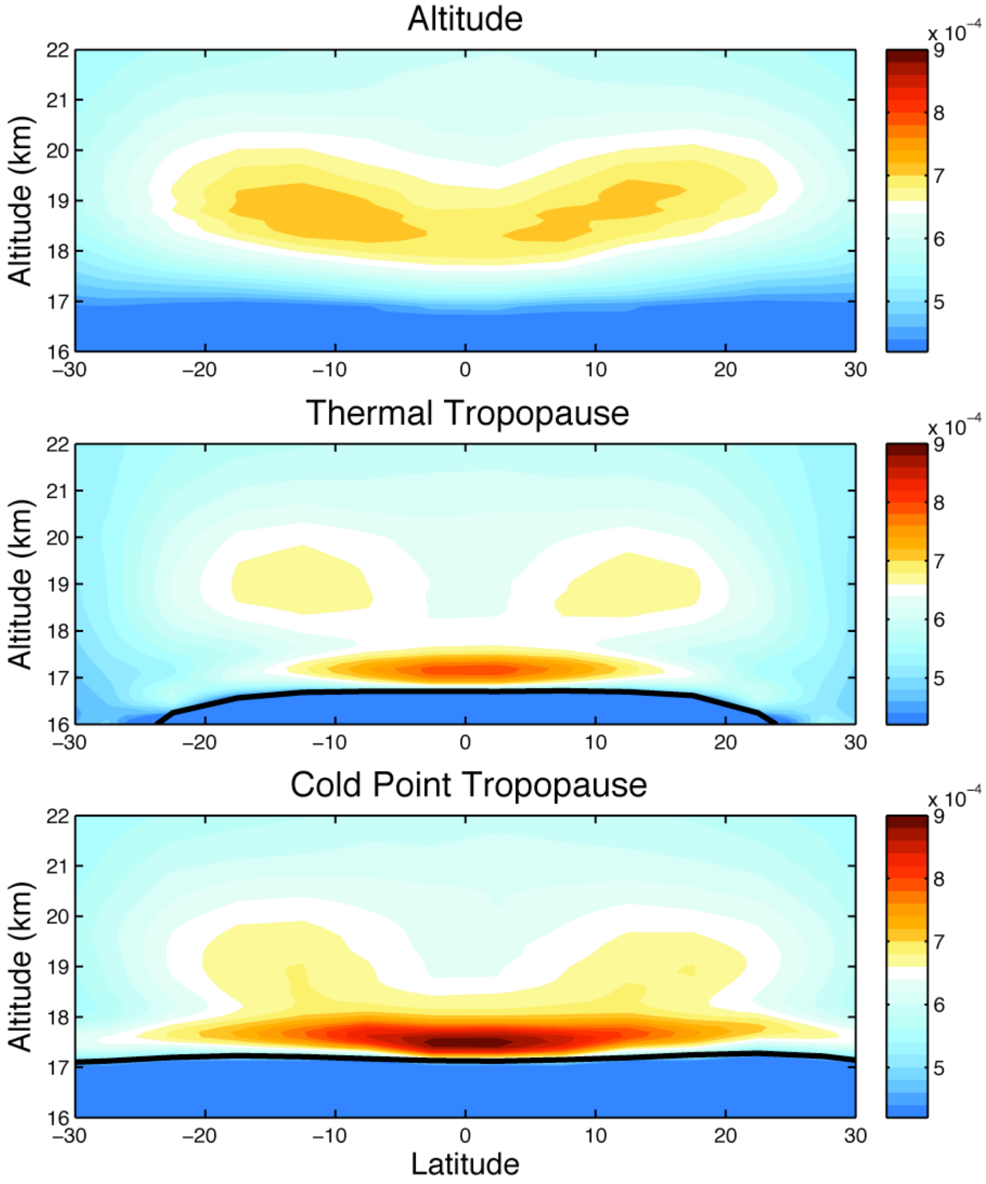

Altitude

Thermal Tropopause

Cold Point Tropopause

Figure 3.2: As in Figure 3.1, but for results focused on the tropical tropopause region in (top panel) conventional vertical coordinates, (middle panel) tropopause-relative vertical coordinates, and (bottom panel) vertical coordinates averaged with respect to the cold point tropopause. The shading interval is 2.0 x 10^{-5} s^{-2}, with values below 4.2 x 10^{-4} s^{-2} not contoured. The thick solid black line is the annual-mean, zonal-mean (middle panel) thermal tropopause height and (bottom panel) cold point tropopause height. Note that the shading interval has been changed from Figure 3.1 to emphasize the vertical structure of the tropical features.

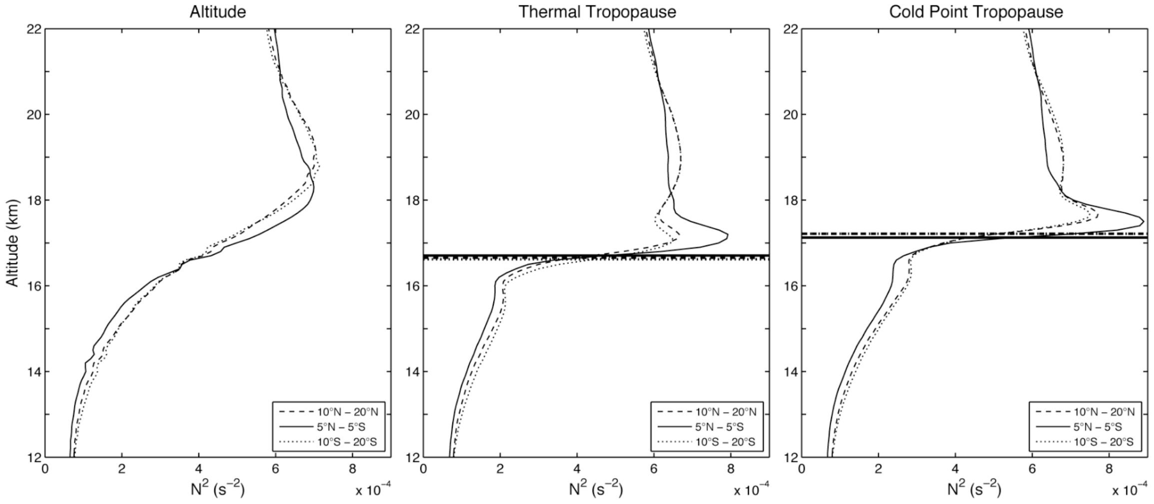

Figure 3.3: Vertical profiles of annual-mean N^2 averaged over the latitude bands indicated in (left panel) conventional vertical coordinates, (middle panel) tropopause-relative vertical coordinates, and (right panel) vertical coordinates averaged with respect to the cold point tropopause. The thick horizontal lines denote the annual-mean (middle panel) thermal tropopause heights and (right panel) cold point tropopause heights for the respective latitude bands.

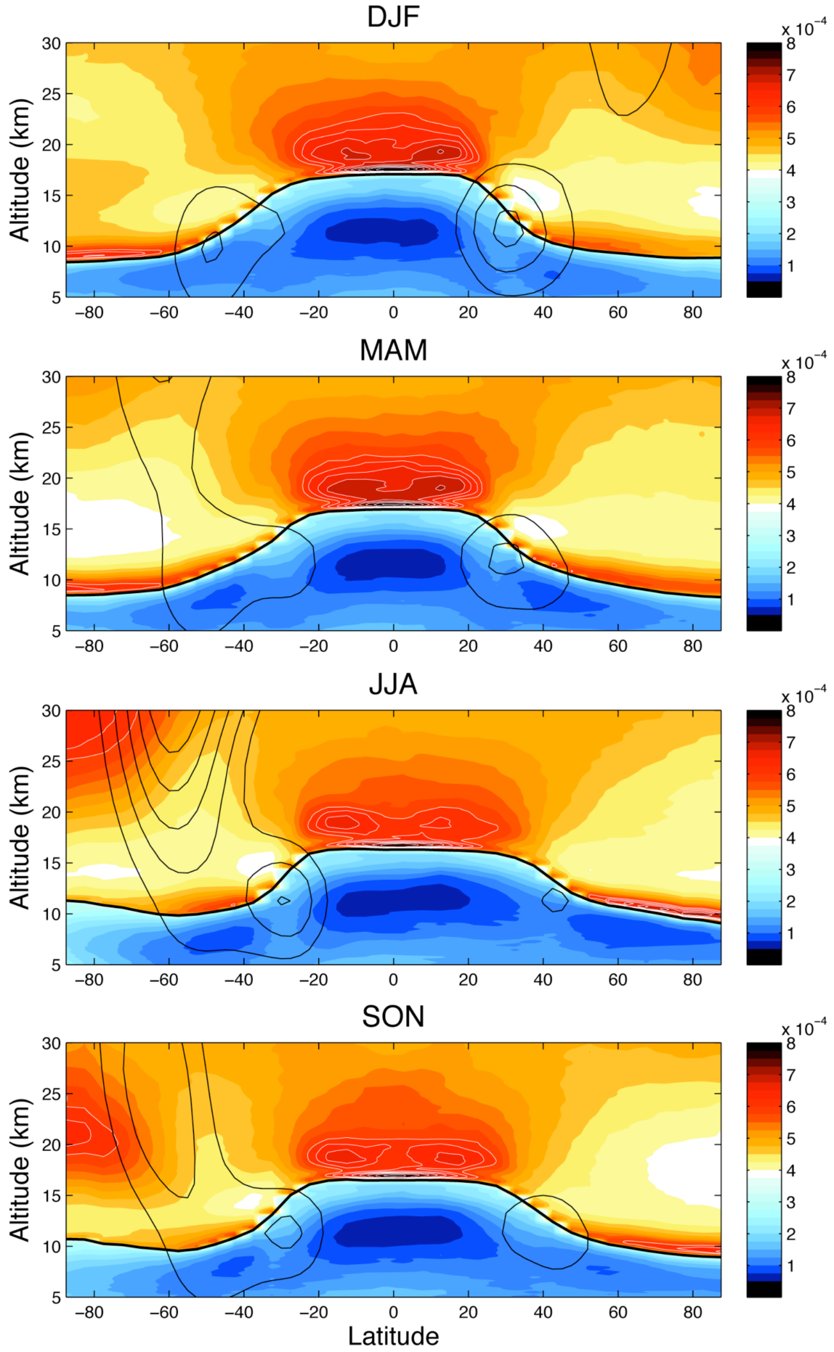

Figure 3.4: Zonal-mean N^2 (shading) averaged over the seasons indicated using data from March 2002 to August 2008. The shading interval is 2.5 x 10^{-5} s^{-2}. Thin black contours denote the corresponding seasonal-mean values of the zonal-mean zonal wind from the NCEP-NCAR reanalysis (lowest contour is 20 m s^{-1}; contour interval is 10 m s^{-1}). The thick solid black line in all panels denotes the seasonal-mean, zonal-mean tropopause height. The thin white contours highlight the shading intervals for values greater than or equal to 6.0 x 10^{-4} s^{-2}. Static stability in this figure and all subsequent figures is shown in tropopause-relative coordinates.

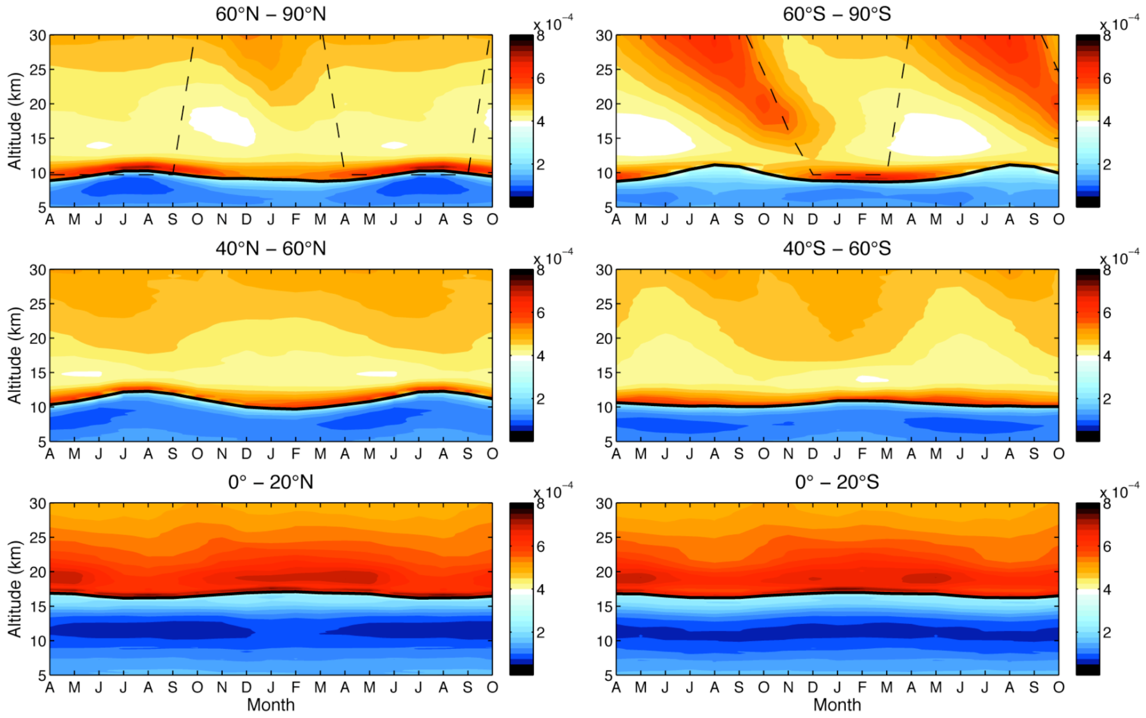

Figure 3.5: Month-height plots of the seasonal cycle in N^2 for the latitude bands indicated. The shading interval is 2.5 x 10^{-5} s^{-2}. The thick solid black line denotes the monthly-mean tropopause height in each plot. The dashed line in the top row denotes the altitude of the maximum westerly zonal wind over the latitude band 50° – 75°. Note that half of the seasonal cycle is repeated in each plot so that the seasonal cycle is not truncated at the edges of the figure.

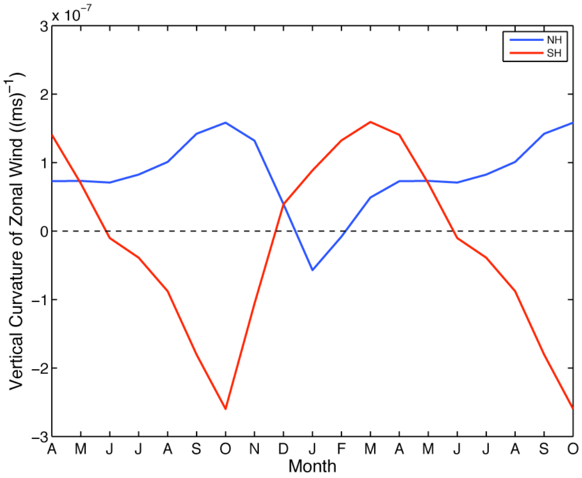

Figure 3.6: Seasonal cycle of the vertical curvature of the 25-km zonal wind averaged over (blue) 50°N – 75°N and (red) 50°S – 75°S. Negative vertical curvature values correspond to a poleward meridional gradient in static stability (see equation 3.2). Note that half of the seasonal cycle is repeated in each plot so that the seasonal cycle is not truncated at the edges of the figure.

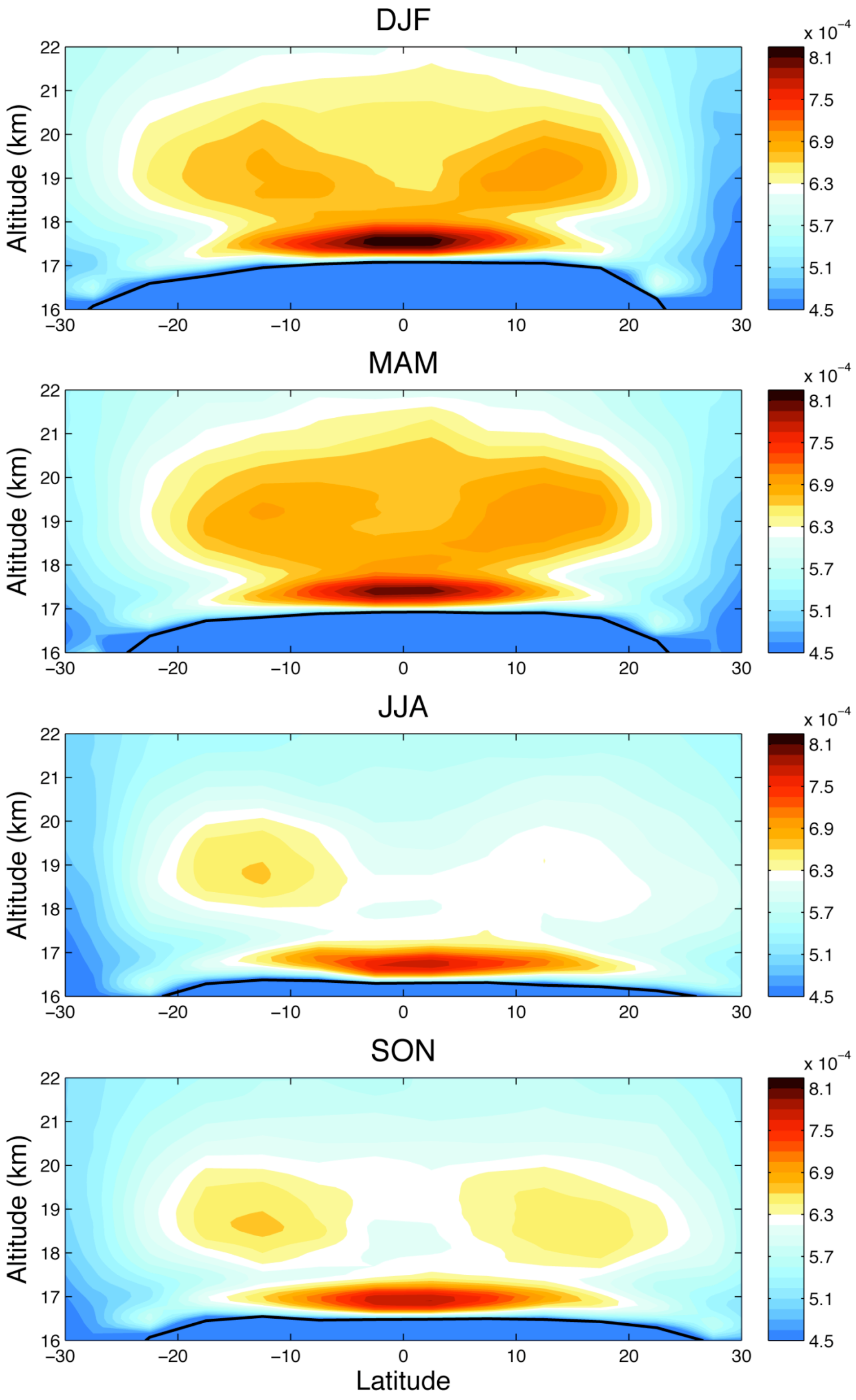

Figure 3.7: As in Figure 3.4, but for results focused on the tropical tropopause region. The shading interval is 1.5 x 10^{-5} s^{-2}, with values below 4.5 x 10^{-4} s^{-2} not contoured. The thick solid black line is the seasonal-mean, zonal-mean tropopause height. Note that the shading interval has been changed from Figure 3.4 to emphasize the vertical structure of the tropical features.

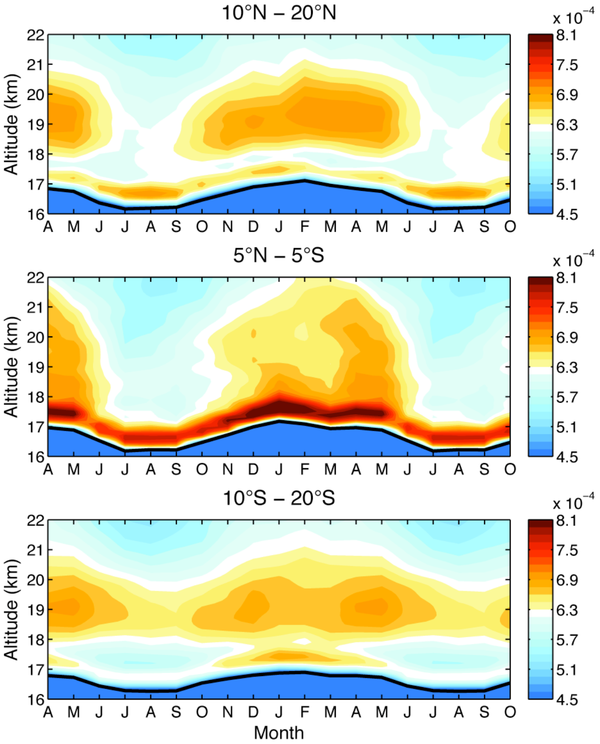

Figure 3.8: As in Figure 3.5, but for results averaged over select tropical latitude bands and focused on the tropical tropopause region. The shading interval is 1.5 x 10^{-5} s^{-2}, with values below 4.5 x 10^{-4} s^{-2} not contoured. The thick solid black line is the monthly-mean tropopause height in each plot. Note that the shading interval has been changed from Figure 3.5 to emphasize the vertical structure of the tropical features.

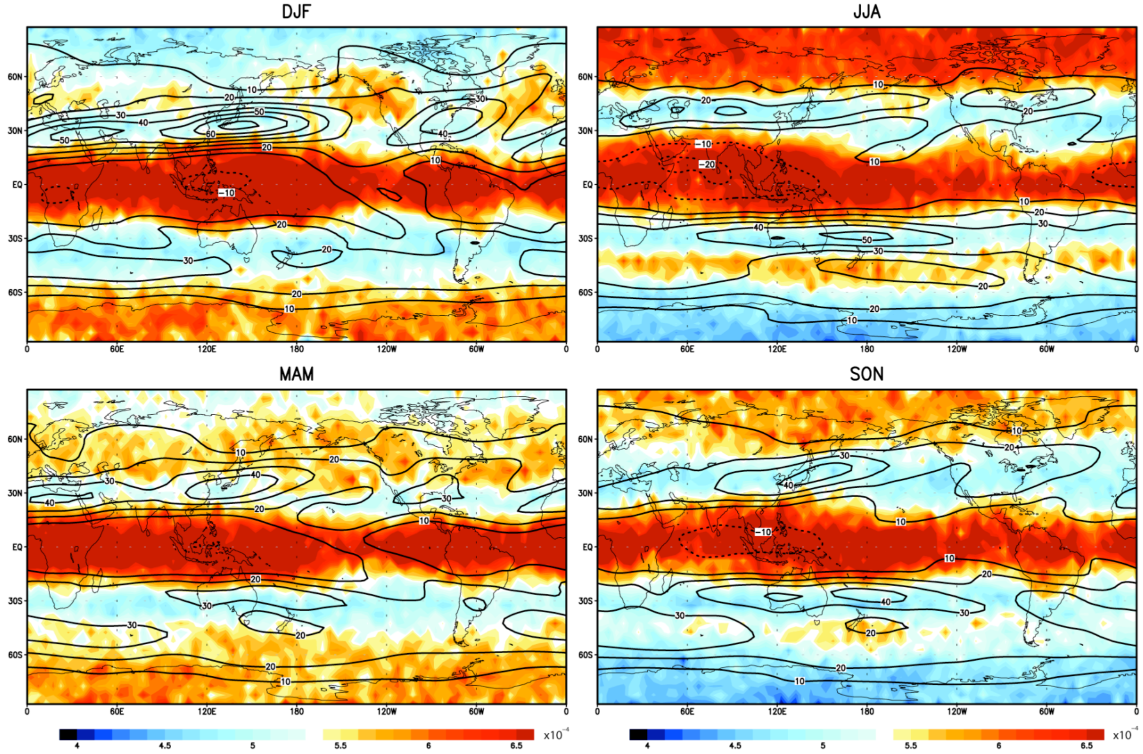

Figure 3.9: Static stability averaged over the 0–1-km layer above the tropopause (shading) for the seasons indicated. The black contours denote the 200-hPa zonal wind from the NCEP-NCAR reanalysis. The shading interval is 1.0 x 10^{-5} s^{-2}, with values above 6.5 x 10^{-4} s^{-2} not contoured. The contour interval for the 200-hPa zonal wind is 10 m s^{-1}. Positive contours are solid, negative contours are dashed, and the zero contour has been omitted.

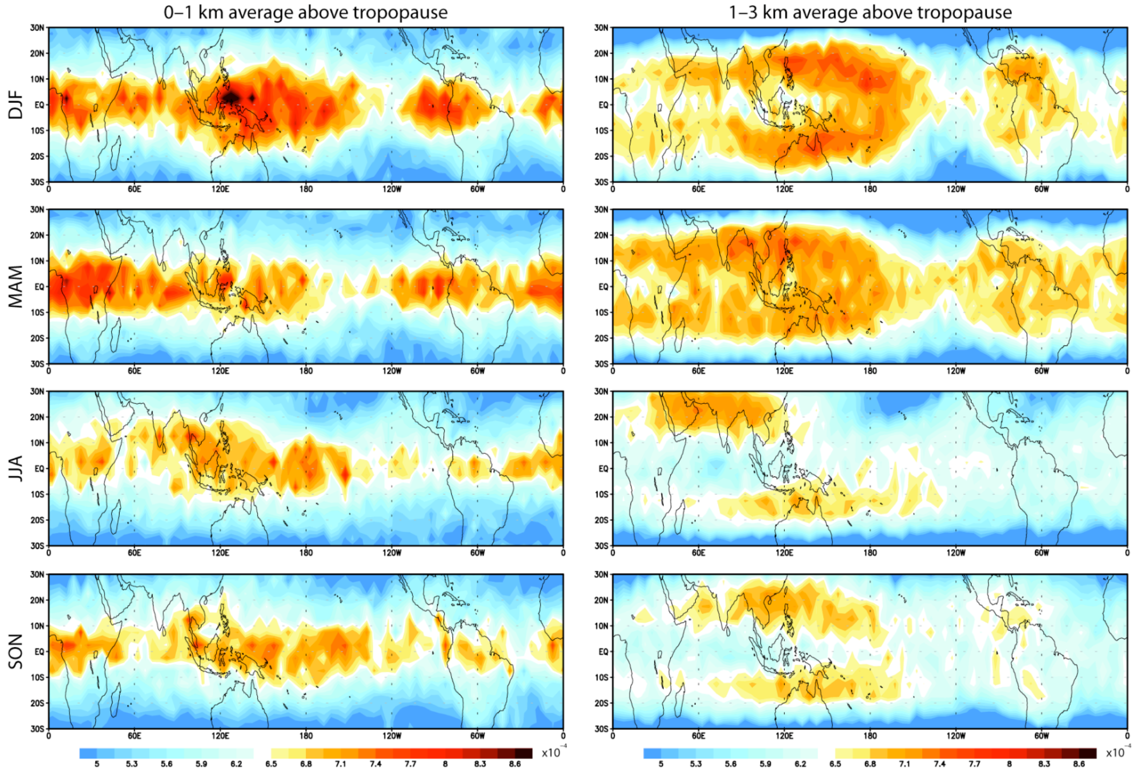

Figure 3.10: As in Figure 3.9, but focused on the tropics. The shading interval is 1.5 x 10^{-5} s^{-2}, with values below 5.0 x 10^{-4} s^{-2} not contoured. Note that the shading interval has been changed from Figure 3.9 to emphasize the horizontal structure of the tropical features.

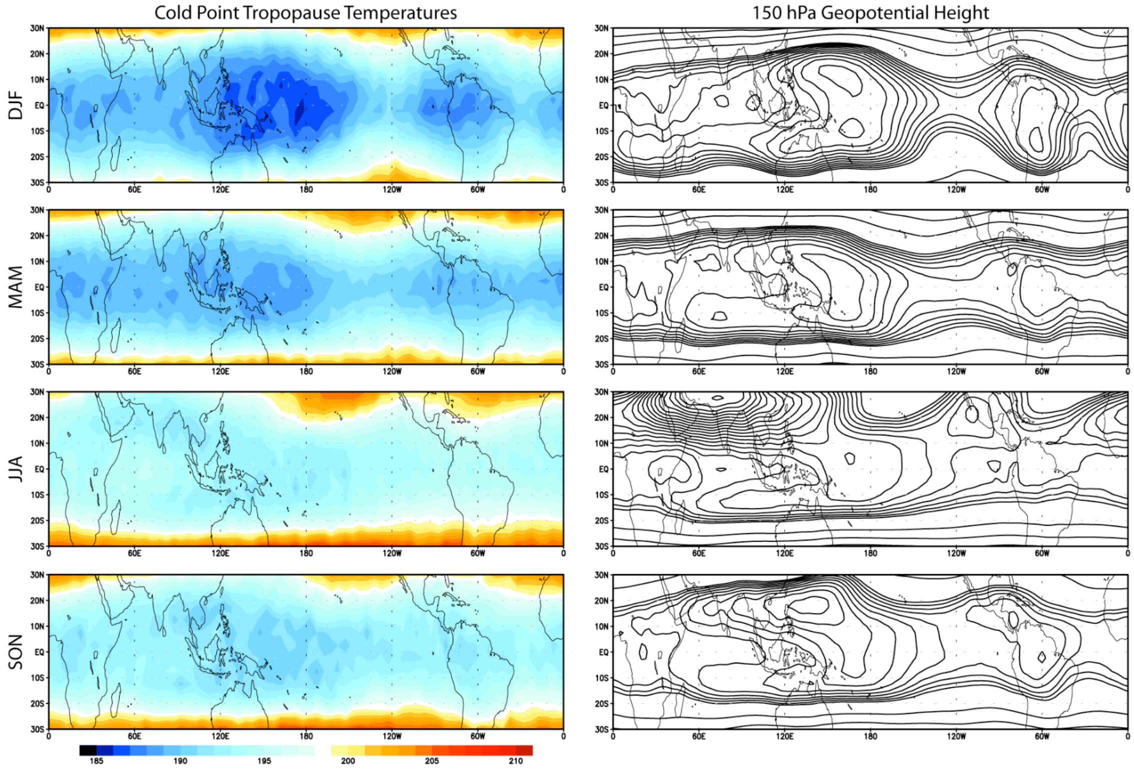

Figure 3.11: (Left column) CHAMP cold point tropopause temperatures and (right column) NCEP–NCAR reanalysis 150 hPa geopotential height averaged over the seasons indicated. The shading interval in the left column is 1 K, and the contour interval in the right column is 100 m for values less than 14200 m and 10 m for values greater than 14200 m (14100, 14200, 14210, 14220, …).

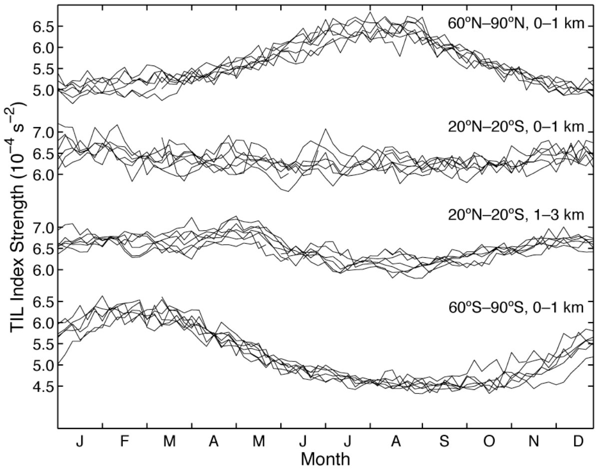

Figure 3.12: TIL index time series averaged over five-day periods and shown as a function of calendar day for the latitude bands and vertical ranges indicated (e.g., 0–1 km indicates the average of N^2 over the 0–1 km layer above the tropopause).

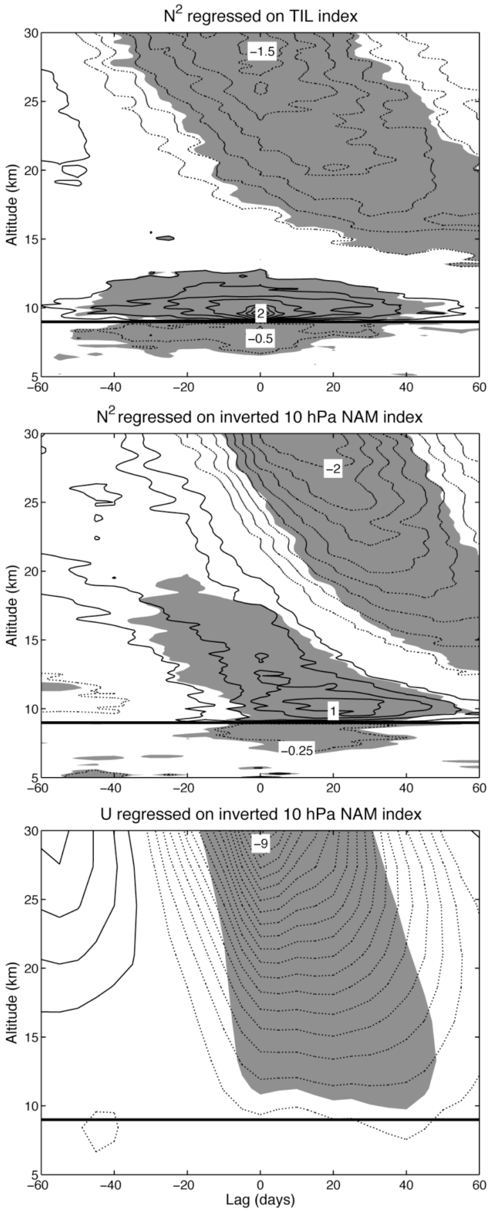

Figure 3.13: (Top) Five-day-mean N^2 anomalies (averaged over 60°N – 90°N) regressed upon wintertime values of the NH polar TIL index time series, and five-day-mean (middle) N^2 anomalies (averaged over 60°N – 90°N) and (bottom) NCEP-NCAR reanalysis zonal wind (U) anomalies (averaged over 50°N – 75°N) regressed upon inverted (i.e., multiplied by –1) values of the five-day-mean 10-hPa NAM index time series. The index time series lead (lag) the N^2 and U anomalies at positive (negative) lags. Positive contours are solid, negative contours are dotted, and the zero contour has been omitted. The contour interval in the top two panels is 2.5×10^{-6} s^{-2}, and the contour labels are in units of 10^{-5} s^{-2}. The contour interval in the bottom panel is 0.5 m s^{-1}. Units are per standard deviation in (top) the TIL index time series and (middle and bottom) the 10-hPa NAM index time series. The shading indicates regions that are 95% significant. The thick solid black line denotes the climatological November – April NH polar tropopause height.

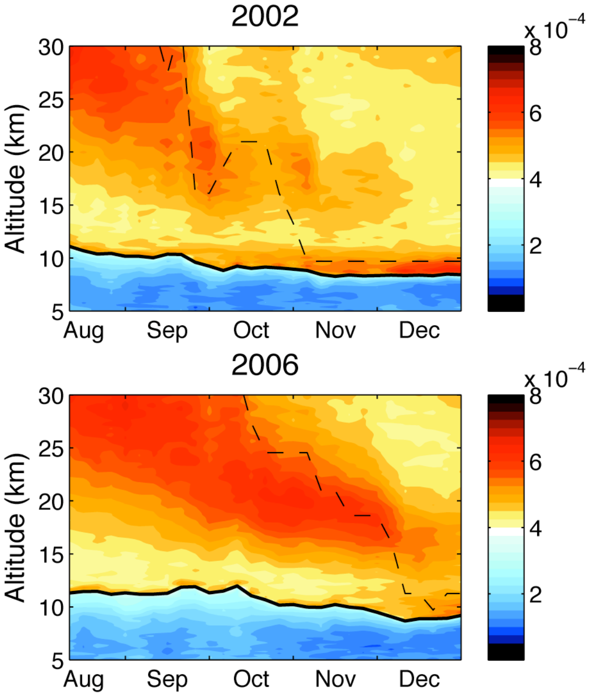

Figure 3.14: Five-day-mean values of N^2 (averaged over 60°S – 90°S) for the period August 9 – December 31. The top panel is for the year 2002, and the bottom panel is for the year 2006. The shading interval is 2.5 x 10^{-5} s^{-2}. The thick solid black line denotes the five-day-mean tropopause height in each plot. The dashed line denotes the altitude of the maximum five-day-mean westerly zonal wind over the latitude band 50°S – 75°S. Note that the values of N^2 in this figure are not anomalies and thus include the seasonal cycle.

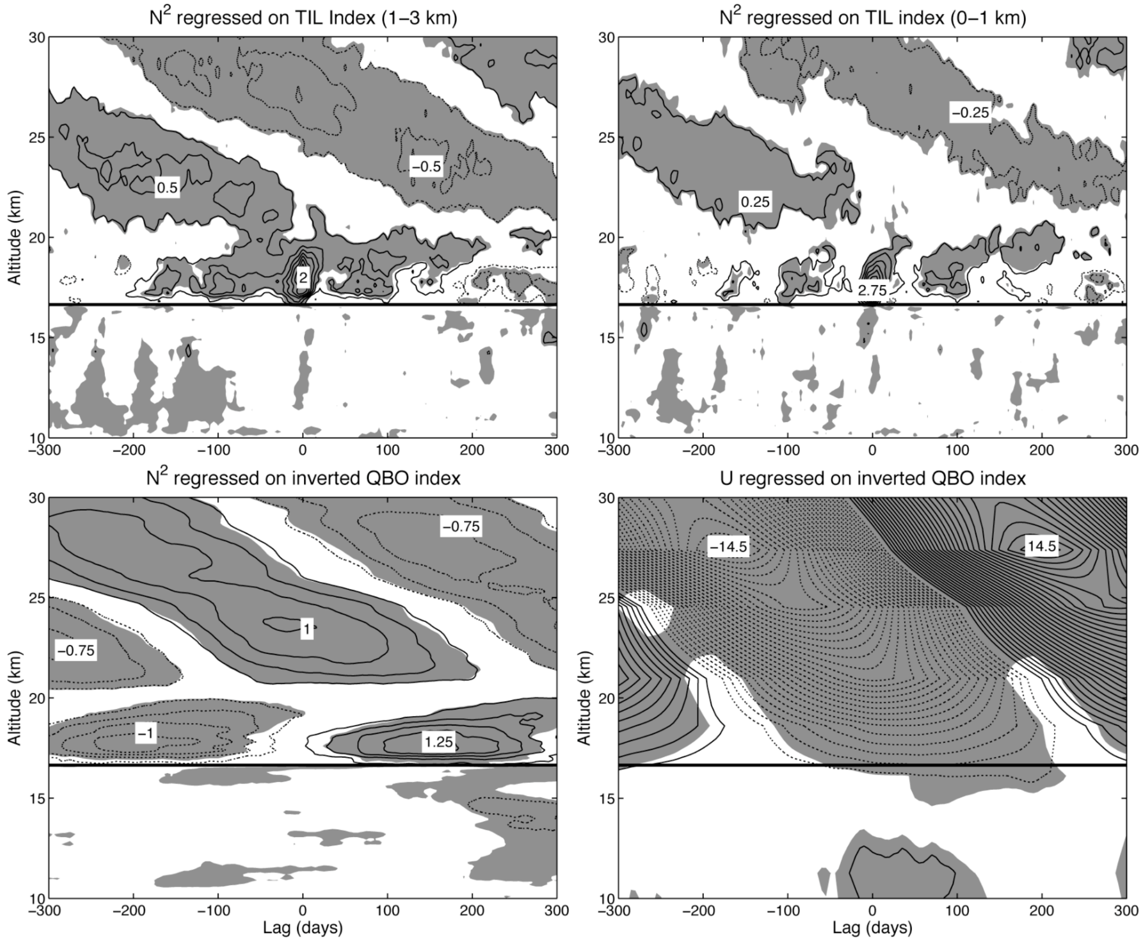

<u>Figure 3.15:</u> As in Figure 3.13, but for N^2 anomalies (averaged over 20°N – 20°S) regressed upon (top left) the 1–3 km tropical TIL index time series, (top right) the 0–1 km tropical TIL index time series, and (bottom left) inverted (i.e., multiplied by –1) values of the QBO index time series and for (bottom right) *U* anomalies at the Equator regressed upon inverted values of the QBO index time series. Units are per standard deviation in (top left) the 1–3 km tropical TIL index time series, (top right) the 0–1 km tropical TIL index time series, and (bottom row) the QBO index time series. The thick solid black line denotes the climatological tropical tropopause height.

CHAPTER 4: EQUATORIAL PLANETARY WAVES AND THEIR SIGNATURE IN ATMOSPHERIC VARIABILITY

The results in Chapter 3 reveal the importance of equatorial planetary waves in fine-scale structures near the tropical tropopause. Yet, as in most previous studies, the results in Chapter 3 focus on the role of equatorial planetary waves in the long-term mean and seasonal cycle of the tropical climate system. The remainder of this dissertation focuses on the role of equatorial planetary waves in driving variability about the seasonal cycle. This chapter develops an index for non-seasonal variations in the equatorial planetary waves, and the following chapter uses that index to assess the role of equatorial planetary waves in climate variability and trends. The results demonstrate that non-seasonal variations in the equatorial planetary waves are associated with a distinct pattern of equatorially symmetric climate variability that dominates the variance of the tropical circulation across a range of timescales.

This chapter begins with a brief review of background information: Section 4.1 reviews previous work on equatorial planetary waves; Section 4.2 reviews the climatology of the eddy kinetic energy field, which – by definition – measures the vigor of the zonally asymmetric components of the atmospheric circulation. Section 4.3 then examines the empirical orthogonal functions (EOFs) of wavelike variability in the tropical circulation and identifies a simple index of the amplitude of the equatorial planetary waves based on eddy kinetic energy. Section 4.4 analyzes the signature of the equatorial planetary waves in various dynamical fields. Conclusions are provided in Section 4.5. All analyses in this chapter are performed using NCEP–NCAR reanalysis data.

4.1 Background

Zonal asymmetries, or eddies, play a fundamental role in the atmospheric general circulation. In the extratropics, baroclinic eddies are generated near the surface in regions of large horizontal temperature gradients and propagate vertically in the troposphere and meridionally in the vicinity of the tropopause (e.g., Simmons and Hoskins 1978; Edmon et al. 1980). The heat and momentum fluxes associated with the eddies are crucial in maintaining key aspects of mid-latitude climate, including the surface westerlies and the horizontal distribution of temperature.

In the tropics, baroclinic instability is inhibited by weak rotation and small horizontal temperature gradients, and quasi-stationary equatorial planetary waves forced by the latent heat release from deep convection play a key role in the large-scale atmospheric circulation. Equatorial planetary waves are readily observed in the climatological-mean tropical circulation and are characterized by: 1) an equatorially trapped Rossby wave response to the west of convective heating over the western tropical Pacific Ocean and 2) a Kelvin wave response to the east of the heating (e.g., Dima et al. 2005; Dima and Wallace 2007). The observed equatorial planetary waves strongly resemble the idealized model response to a localized mid-tropospheric heat source centered on the Equator (e.g., Gill 1980; Highwood and Hoskins 1998; see also Appendix B). The equatorial planetary waves propagate vertically, achieving their maximum amplitude in the tropical upper troposphere (e.g., Dima and Wallace 2007) before becoming evanescent at stratospheric levels (Dunkerton 1995).

As is the case for baroclinic eddies in the extratropics, equatorial planetary waves play an important role in the momentum balance of the atmosphere. In the upper troposphere, the equatorial Rossby wave pattern is tilted meridionally, such that the Rossby waves propagate out of the deep tropics and flux westerly momentum into the equatorial upper troposphere (e.g., Dima et al. 2005). As a result, model experiments that include zonally asymmetric heating in the tropics – and thus generate equatorial planetary waves – often produce upper tropospheric westerly winds (superrotation) centered about the Equator (Kraucunas and Hartmann 2005). However, observations indicate easterlies in the tropical upper troposphere; the observed easterlies are driven not by the equatorial planetary waves (which provide a westerly torque in the tropical upper troposphere), but rather by the easterly torque associated with the seasonal cycle in the upper tropospheric cross-equatorial flow (Lee 1999; Dima et al. 2005; Kraucunas and Hartmann 2005).

Equatorial planetary waves may also be important in driving a component of the long-term mean upwelling at the tropical tropopause. Until recently, the long-term mean and seasonal cycle of temperatures in the tropical lower stratosphere have been explained almost exclusively in the context of upwelling driven by the zonal-mean balanced response to planetary wave breaking in the extratropical stratosphere (Yulaeva et al. 1994; Holton et al. 1995; Ueyama and Wallace 2010; see also Section 1.3.1). However, several recent studies have proposed that the upwelling is also influenced by the eddy momentum flux convergence associated with equatorial planetary waves (Boehm and Lee 2003; Kerr-Munslow and Norton 2006; Norton 2006; Randel et al. 2008; Ryu and Lee

2010). In this case, the seasonal cycle in tropical upwelling is due not to the seasonal cycle in Northern Hemisphere stratospheric wave breaking but to either 1) the seasonal cycle in the latitude of tropical convection (Norton 2006) or 2) the seasonal cycle in the height of tropical convection and its associated wave response (Randel et al. 2008). To date, the exact role of equatorial planetary waves in tropical upwelling remains unresolved.

4.2 Climatology of the eddy kinetic energy field

The left panel in Figure 4.1 shows climatological-mean, zonal-mean values of eddy kinetic energy. Eddy kinetic energy is characterized by distinct maxima in the extratropical stratosphere and upper troposphere and by locally large values in the tropical upper troposphere (e.g., Peixoto and Oort 1992). The extratropical stratospheric maxima largely arise from the active seasons of planetary wave activity in the stratosphere, whereas the extratropical upper tropospheric maxima are co-located with the mid-latitude eddy-driven jets in both hemispheres. The locally large values in the tropical upper troposphere primarily result from the equatorially symmetric component of equatorial planetary waves, particularly the equatorial Rossby wave component (e.g., Dima et al. 2005). The tropical eddy kinetic energy exhibits a semi-annual cycle with peaks during the monsoon seasons (Dima et al. 2005; Dima and Wallace 2007).

The right panel in Figure 4.1 shows the horizontal distribution of climatological-mean eddy kinetic energy at 150 hPa, the level of the largest tropical values in the left panel of Figure 4.1. In the extratropics, eddy kinetic energy peaks in regions of large baroclinic wave activity, including the North Atlantic Ocean, North Pacific Ocean, and

Southern Ocean storm track regions (e.g., Peixoto and Oort 1992). In the tropics, eddy kinetic energy peaks in regions where the climatological-mean equatorial planetary waves have largest amplitude, including India, the Maritime Continent, the eastern tropical Pacific Ocean, and the tropical Atlantic Ocean (e.g., Dima et al. 2005; Dima and Wallace 2007). The maxima in eddy kinetic energy over the eastern tropical Pacific Ocean and tropical Atlantic Ocean may also reflect the influence of extratropical eddies at tropical latitudes (e.g., Webster and Holton 1982).

4.3 Identifying the leading pattern of wavelike variability in the tropical atmosphere

This section isolates and examines the leading pattern of wavelike variability in the tropical atmosphere using the eddy kinetic energy field. The dominant pattern of variability in the tropical eddy kinetic energy field is identified by calculating the leading principal component (PC) time series of the daily-mean, zonal-mean eddy kinetic energy anomalies for the region 20ºN – 20ºS (see Section 2.2.4 for a review of EOF analysis). The leading PC time series explains 33% of the variance in the zonal-mean eddy kinetic energy field of the tropics and is well separated from subsequent PC time series via the criterion of North et al. (1982); the second PC time series explains only 13% of the variance in the zonal-mean eddy kinetic energy field. The ~33:13 ratio in explained variance points to the robustness of the pattern described by the leading PC time series. As demonstrated below, the leading PC time series reflects variability in the amplitude of equatorial planetary waves and is highly correlated with the leading PC time series of other dynamical fields in the tropics. For these reasons, the leading PC time series of zonal-mean eddy kinetic energy in the tropics is referred to as the equatorial planetary wave index (EPWI).

The top row of Figure 4.2 shows the regressions of daily-mean zonal-mean eddy kinetic energy anomalies (left) and daily-mean 150-hPa eddy kinetic energy anomalies (right) upon the standardized EPWI time series. Positive values of the EPWI time series are associated with large positive zonal-mean eddy kinetic energy anomalies in the tropical upper troposphere (Figure 4.2, top left). (Note that the sign of the EPWI time series is arbitrary and is chosen here such that positive values correspond to positive eddy kinetic energy anomalies in the tropical troposphere.) The tropical eddy kinetic energy anomalies extend from the lower troposphere into the lower stratosphere and arise largely from the Maritime Continent region and the eastern tropical Pacific Ocean (Figure 4.2, top right). The enhanced region of eddy kinetic energy in the tropical upper troposphere is accompanied by positive eddy kinetic energy anomalies in the subtropical upper troposphere of each hemisphere (Figure 4.2, top left). The subtropical anomalies are manifestations of enhanced eddy kinetic energy over the subtropical western Pacific Ocean in both hemispheres (Figure 4.2, top right). Interestingly, the sign of the anomalies is the same in all centers of action, which suggests eddy kinetic energy varies in-phase across a wide geographical region.

The top panel in Figure 4.3 shows the regressions of daily-mean 150-hPa Z^* anomalies onto the standardized EPWI time series. (Z^* denotes the eddy component of the geopotential height field; the zonal mean has been removed to accentuate the zonally asymmetric features in the figure.) The results are clearly reminiscent of the long-term mean structure of equatorial planetary waves (e.g., Dima et al. 2005; Dima and Wallace

2007) and the wave response to localized diabatic heating centered on the Equator (e.g., Gill 1980; Highwood and Hoskins 1998; Kraucunas and Hartmann 2005; Norton 2006): i.e., positive values of the EPWI time series are associated with paired 150-hPa anticyclones and cyclones that straddle the Equator over the Pacific Ocean. Hence, the wavelike variability described by the EPWI time series appears to be strongly linked to the amplitudes of the long-term mean equatorial planetary waves.

The relationship between the EPWI time series and the long-term mean equatorial planetary waves is further elucidated in the second row of Figures 4.2 and 4.3. The figures are generated as follows. First, the structure of the climatological-mean equatorial planetary waves is defined as the seasonally-varying climatological mean of the wave component of the 150-hPa zonal wind field (150 hPa u^*; Dima and Wallace 2007). Second, a time series of the climatological-mean pattern of equatorial planetary waves is generated by projecting daily 150-hPa u^* anomalies onto the seasonally-varying climatological-mean 150-hPa u^* field over the domain 20ºN – 20ºS. Third, eddy kinetic energy (Figure 4.2, second row) and 150 hPa Z^* (Figure 4.3, second panel) are regressed onto standardized values of the resulting projection time series. By construction, the projection time series captures variability in the amplitude of the equatorial planetary waves that dominate the climatology. The projection time series is correlated with the EPWI time series at a level of $r = 0.74$ (Table 4.1), and the corresponding regressions (Figures 4.2 and 4.3, second row) bear a strong resemblance to the patterns associated with the EPWI time series (Figures 4.2 and 4.3, top row). Thus, the leading pattern of wavelike variability in the tropical circulation (as captured by the EPWI time series) describes the pulsation of the amplitude of the climatological-mean pattern of equatorial planetary waves.

The structures associated with the EPWI time series also emerge in association with EOF analysis of other dynamical fields. Similar patterns are derived from regressions based on: 1) the leading PC time series of daily-mean eddy kinetic energy anomalies for the region 20ºN – 20ºS at 150 hPa (i.e., the eddy kinetic energy is not zonally averaged; Figures 4.2 and 4.3, third row), 2) the second PC time series of daily-mean zonal wind anomalies for the region 20ºN – 20ºS at 200 hPa (Figure 4.4, top), 3) the sum of the first two PC time series of daily-mean Z^* anomalies for the region 20ºN – 20ºS at 150 hPa (Figure 4.4, middle), and 4) the sum of the first two PC time series of daily-mean T^* anomalies for the region 20ºN – 20ºS at 100 hPa (Figure 4.4., bottom). (T^* denotes the eddy component of the temperature field.)

The variability described by the EPWI time series does not arise from one individual season (Table 4.2). Although the regressions shown in Figures 4.2 and 4.3 encompass all months, regressions using data from individual seasons produce very similar patterns (e.g., compare the 150 hPa Z^* regressions shown in the top row of Figure 4.5 with the regressions shown in the top panel of Figure 4.3). Notable differences between the seasons reflect the seasonally-varying structure of the equatorial planetary waves. To illustrate this, the middle row of Figure 4.5 shows composites of the 150-hPa geopotential height field for days when the EPWI time series is greater than +1 standard deviation; the bottom row of Figure 4.5 shows composites of the 150-hPa geopotential height field for days when the EPWI time series is less than –1 standard deviation. The results reveal that the differences between the 150 hPa Z^* regression patterns shown in

Figure 4.5 (top row) largely reflect the westward shift of the equatorial planetary waves in the Northern Hemisphere during June – August and the corresponding development of the Asian monsoon anticyclone. The remaining results in this chapter and the following chapter focus on data from all months, but it is important to realize that the structures associated with the EPWI time series are less equatorially symmetric in individual seasons because of seasonal differences in the climatological-mean equatorial planetary waves.

The results in this section thus reveal that:

1. The leading pattern of wavelike variability in the tropics is succinctly captured via EOF analysis of the zonal-mean tropical eddy kinetic energy field.
2. The resulting PC time series (referred to as the EPWI time series) is indicative of variability in the amplitude (i.e., pulsing) of the climatological-mean pattern of equatorial planetary waves. Positive values of the EPWI time series correspond to enhanced amplitudes of the equatorial planetary waves, and vice versa.
3. The EPWI time series is very robust: it explains 33% of the variance in the zonal-mean tropical eddy kinetic energy field, can be derived by projecting the wave component of the flow onto the seasonally-varying climatological-mean structure of the equatorial planetary waves, and emerges from individual seasons and from EOF analysis of a range of dynamical fields.

In the following section, the structures associated with the EPWI time series are explored in further detail.

4.4 Signature of equatorial planetary waves in atmospheric variability

This section examines the structures associated with variability in the amplitude of the climatological-mean pattern of equatorial planetary waves by regressing various zonal mean and zonally varying fields onto standardized values of the EPWI time series. Zonal-mean results are shown in Figure 4.6, and zonally varying results are shown in Figure 4.7. Note that the eddy kinetic energy and *Z** regressions shown in Figures 4.6 and 4.7 are reproduced from Figures 4.2 and 4.3 for the purpose of comparison.

As noted in the previous section, periods of enhanced amplitude in the equatorial planetary waves (i.e., the positive polarity of the EPWI time series) are associated with anomalously large eddy kinetic energy over the Maritime Continent, the eastern tropical Pacific Ocean, and the western Pacific Ocean at mid-latitudes (Figure 4.7, top). The regions of enhanced eddy kinetic energy extend from the mid-troposphere to the lower stratosphere (Figure 4.6, top left). The periods of enhanced wave amplitude are also associated with equatorward eddy momentum flux anomalies in the tropical upper troposphere of both hemispheres (Figure 4.6, top right). The equatorward eddy momentum flux anomalies evident in the zonal mean arise largely from a meridional couplet over the Maritime Continent (Figure 4.7, third panel) and are consistent with the meridional tilt of the 150-hPa *Z** anomalies in that region (Figure 4.7, second panel). The pattern of the tropical eddy momentum flux anomalies in Figure 4.6 (top right) is similar to that associated with the modeled equatorial planetary wave response to a localized mid-tropospheric diabatic heating anomaly centered on the Equator (Kraucunas and Hartmann 2005; Norton 2006).

The results in Figure 4.6 (top right) also suggest that the EPWI time series is associated with eddy momentum flux anomalies in the upper troposphere at extratropical latitudes. Hence, variations in the amplitude of the equatorial planetary waves are seemingly linked to variability in the extratropical fluxes of momentum. The causal nature of these linkages is unclear, but it is worth noting that a similar pattern of extratropical eddy momentum fluxes is found in the idealized modeling experiments of Kraucunas and Hartmann (2005; c.f. the transient eddy momentum fluxes in their Figure 7c).

The pattern of zonal-mean zonal wind anomalies associated with variability in the equatorial planetary waves (Figure 4.6, middle left) is consistent with forcing by the eddy momentum flux anomalies in Figure 4.6 (top right). Westerly wind anomalies are found in the tropical upper troposphere in the region of anomalous eddy momentum flux convergence, and easterly wind anomalies are found throughout the depth of the subtropical troposphere in both hemispheres. The barotropic component of the subtropical easterly wind anomalies is mandated by the anomalous divergence of the eddy momentum fluxes at ~20º latitude. The upper tropospheric zonal-mean zonal wind anomalies arise primarily from the eastern Pacific Ocean sector (Figure 4.7, bottom) and are physically consistent with flow around the anomalous upper tropospheric cyclones evident in the Z^* field (Figure 4.7, second panel).

Meridional momentum fluxes cannot entirely explain the zonal-mean zonal wind anomalies in Figure 4.6 (middle left). In fact, the tropical zonal-mean zonal wind anomalies extend into the mid-troposphere below the region of anomalous meridional eddy momentum flux convergence. Thus, consistent with the experiments of Kraucunas and Hartmann (2005) and Norton (2006), downward eddy momentum fluxes must act to spread the westerly zonal wind anomalies into the mid-troposphere (Figure 4.6, middle right). However, the results in Figure 4.6 (middle right) should be treated with caution because they are derived from NCEP–NCAR reanalysis vertical velocities, which extend only up to 100 hPa and are strongly model dependent.

To further illustrate the role of the meridional and vertical eddy momentum flux anomalies in Figure 4.6, Figure 4.8 displays the regressions on the EPWI time series of select terms from the Eulerian mean zonal momentum equation (4.1). The equation is written in log-pressure vertical coordinates, where the overbars denote a zonal mean and the primes denote deviations (eddies) from that zonal mean (e.g., Andrews et al. 1987).

$$\frac{\partial \overline{u}}{\partial t} = -\overline{v}\left(\frac{1}{a\cos\phi}\frac{\partial\left(\overline{u}\cos\phi\right)}{\partial\phi} - f\right) - \overline{w}\frac{\partial\overline{u}}{\partial z} - \frac{1}{a\cos^2\phi}\frac{\partial\left(\overline{u'v'}\cos^2\phi\right)}{\partial\phi} - \frac{1}{\rho_0}\frac{\partial\left(\rho_0\overline{u'w'}\right)}{\partial z} + F \qquad (4.1)$$

Figure 4.8 shows the regressions of the first, third, and fourth terms on the right hand side of (4.1). Frictional effects F are neglected, and the effects from the mean vertical flow (second term on right hand side in 4.1) are negligible and are not shown. The results in Figure 4.8 support the role of eddy momentum fluxes in driving westerly wind anomalies in the tropical mid- and upper troposphere and easterly wind anomalies in the subtropics. As discussed below, the advection of angular momentum by the mean meridional flow is small at tropical latitudes but balances the effects of the meridional momentum fluxes in the subtropics and extratropics (Figure 4.8, top).

The patterns of zonal-mean temperature and meridional mass streamfunction anomalies associated with variability in the equatorial planetary waves (Figure 4.6, bottom row) are also consistent with forcing by the eddy momentum flux anomalies (the linkages are summarized in the schematic in Figure 4.9). The anomalous divergence of the momentum fluxes at ~20º latitude is balanced by the Coriolis torque acting on anomalous poleward motion; the anomalous convergence of the momentum fluxes in the deep tropics is balanced by the Coriolis torque acting on anomalous equatorward motion (Figure 4.8, top; note that the balance does not hold right at the Equator, where the Coriolis parameter goes to zero). The positive temperature anomalies in the subtropical troposphere at ~30º latitude are consistent with adiabatic warming in the subsiding branches of the resulting meridional circulation cells, and the weak or slightly negative temperature anomalies at ~15º latitude are consistent with the rising branches of the circulation cells. The negative temperature anomalies in the lower tropical stratosphere and the positive temperature anomalies at the Equator below 150 hPa are consistent with the meridional convergence of the mass circulation near the tropical tropopause level.

To further illustrate the role of vertical motion in the temperature anomalies in Figure 4.6 (bottom left), Figure 4.10 displays the regressions on the EPWI time series of select terms from the Eulerian mean thermodynamic equation (4.2) (e.g., Andrews et al. 1987).

$$\frac{\partial\bar{\theta}}{\partial t} = -\frac{\bar{v}}{a}\frac{\partial\bar{\theta}}{\partial\phi} - \bar{w}\frac{\partial\bar{\theta}}{\partial z} - \frac{1}{a\cos\phi}\frac{\partial(\overline{v'\theta'}\cos\phi)}{\partial\phi} - \frac{1}{\rho_0}\frac{\partial}{\partial z}\left(\rho_0\overline{w'\theta'}\right) + Q \qquad (4.2)$$

Figure 4.10 shows the regressions of the second, third, and fourth terms on the right hand side of (4.2). Diabatic effects *Q* are neglected, and the effects from the mean meridional flow (first term on right hand side in 4.2) are negligible and are not shown. The results in Figure 4.10 support the role of adiabatic warming and cooling in driving the tropospheric temperature anomalies in Figure 4.6 (bottom left). Because the reanalysis vertical velocities extend only up to 100 hPa, the importance of vertical motion for the stratospheric temperature anomalies can only be surmised (see schematic in Figure 4.9). Interestingly, the middle panel of Figure 4.10 suggests that meridional heat fluxes may also play a role in forcing the lower stratospheric temperature anomalies. However, the results in Figure 4.10 should be viewed with caution because 1) the top and bottom panels are derived from reanalysis vertical velocities and 2) they neglect the contribution from diabatic processes. Diabatic processes, including latent heating in deep convective clouds and radiative cooling at cloud tops, could play a key role in forcing the temperature anomalies in Figure 4.6 (bottom left), particularly in the deep tropics.

The above results reveal that variations in the amplitude of the climatological-mean pattern of equatorial planetary waves are associated not only with upper tropospheric geopotential height and zonal wind anomalies (Figure 4.7, second and fourth panels), but also with a series of distinct equatorially symmetric features in the zonal-mean circulation. The structures bear a strong similarity to the patterns of eddy momentum flux, zonal wind, and temperature evident in the numerical simulations of Kraucunas and Hartmann (2005) and Norton (2006). Prominent zonal-mean features observed in association with enhanced amplitude in the equatorial planetary waves include:

1. Anomalous meridional eddy momentum flux convergence in the tropical upper troposphere and anomalous meridional eddy momentum flux divergence in the subtropical upper troposphere (Figure 4.6, top right)
2. Anomalous vertical eddy momentum flux convergence in the tropical mid-troposphere and anomalous vertical eddy momentum flux divergence in the tropical upper troposphere (Figure 4.6, middle right)
3. Westerly zonal wind anomalies in the tropical upper troposphere and easterly zonal wind anomalies throughout the depth of the subtropical troposphere (Figure 4.6, middle left)
4. Positive temperature anomalies in the subtropical troposphere juxtaposed against negative temperature anomalies near the tropopause in both the tropics and the subtropics (Figure 4.6, bottom left)
5. Anomalous meridional circulation cells in the troposphere of each hemisphere with rising motion at ~15º latitude and sinking motion near the Equator and at ~30º latitude (Figure 4.6, bottom right)

4.5 Conclusions

Previous studies have established that equatorial planetary waves dominate the zonally asymmetric component of the climatological-mean tropical tropospheric circulation. The waves are forced by the latent heat release associated with deep convection and are characterized by an equatorially trapped Rossby wave response to the west of the convection and a Kelvin wave response to the east of the convection (e.g., Gill 1980; Highwood and Hoskins 1998; Dima et al. 2005; Dima and Wallace 2007).

The equatorial planetary waves play an important role in the zonal-mean momentum balance of the tropics (Lee 1999; Dima et al. 2005; Kraucunas and Hartmann 2005) and are potentially important for tropical troposphere/stratosphere exchange (e.g., Boehm and Lee 2003; Norton 2006; Randel et al. 2008).

The results of this chapter demonstrate that equatorial planetary waves play an equally prominent role in driving variability in the tropical circulation about its climatological mean. The leading pattern of wavelike variability in the tropical atmosphere corresponds to pulsation in the amplitude of the climatological-mean pattern of equatorial planetary waves. Hence, equatorial planetary waves not only dominate the wavelike component of the mean tropical circulation, but they also play an important role in its variability. The leading pattern of tropical wavelike variability is identified here on the basis of the leading PC time series of the zonal-mean tropical eddy kinetic energy field (referred to herein as the equatorial planetary wave index, or EPWI, time series). Very similar structures emerge from EOF analysis of a range of key tropical dynamical fields.

Variations in the amplitude of the equatorial planetary waves (as characterized by the EPWI time series) are associated with a range of tropical circulation anomalies that are reminiscent of the simulated response to zonally asymmetric tropical heating (e.g., Gill 1980; Highwood and Hoskins 1998; Kraucunas and Hartmann 2005; Norton 2006). The positive polarity of the EPWI time series (i.e., enhanced amplitudes of the equatorial planetary waves) is associated with: 1) equatorially symmetric eddy momentum flux anomalies that converge about the Equator in the upper troposphere, 2) westerly upper tropospheric wind anomalies centered about the Equator, 3) negative temperature anomalies at the tropical tropopause, 4) deep easterly wind anomalies centered at ~25º latitude in both hemispheres, and 5) positive temperature anomalies throughout the depth of the Northern and Southern Hemisphere subtropical troposphere (Figures 4.6 and 4.7). The zonal-mean temperature and wind anomalies associated with variations in the equatorial planetary waves are consistent with the zonal-mean balanced response to the equatorially symmetric eddy momentum flux anomalies in the tropical upper troposphere (Figures 4.6 and 4.9).

In the next chapter, the above results are discussed in the context of the El Niño-Southern Oscillation (ENSO) and the Madden-Julian Oscillation (MJO) and are used to interpret tropical climate variability and trends. Additionally, the results are linked to the fine-scale static stability structures discussed in Chapter 3.

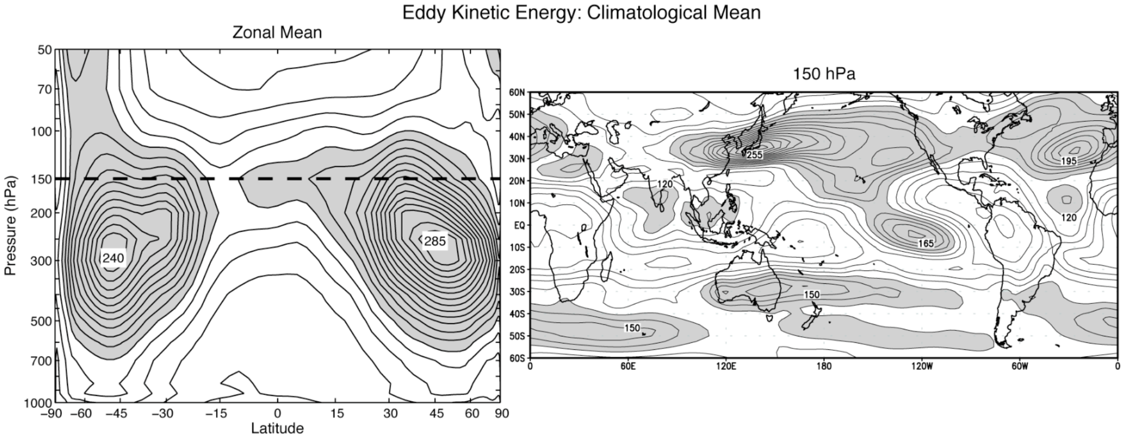

Figure 4.1: Climatological-mean (left panel) zonal-mean eddy kinetic energy and (right panel) 150-hPa eddy kinetic energy. The contour interval is 15 $m^2 s^{-2}$ with the shading added to highlight values greater than (left) 75 $m^2 s^{-2}$ and (right) 120 $m^2 s^{-2}$. The thick dashed horizontal line in the left panel denotes the level shown in the right panel. The abscissa in the left panel of this figure and all subsequent figure panels with zonal-mean cross sections is plotted with a sine of latitude scale to accentuate the tropical features. All figures in this chapter are based on NCEP–NCAR reanalysis data covering the period 1979 – 2009.

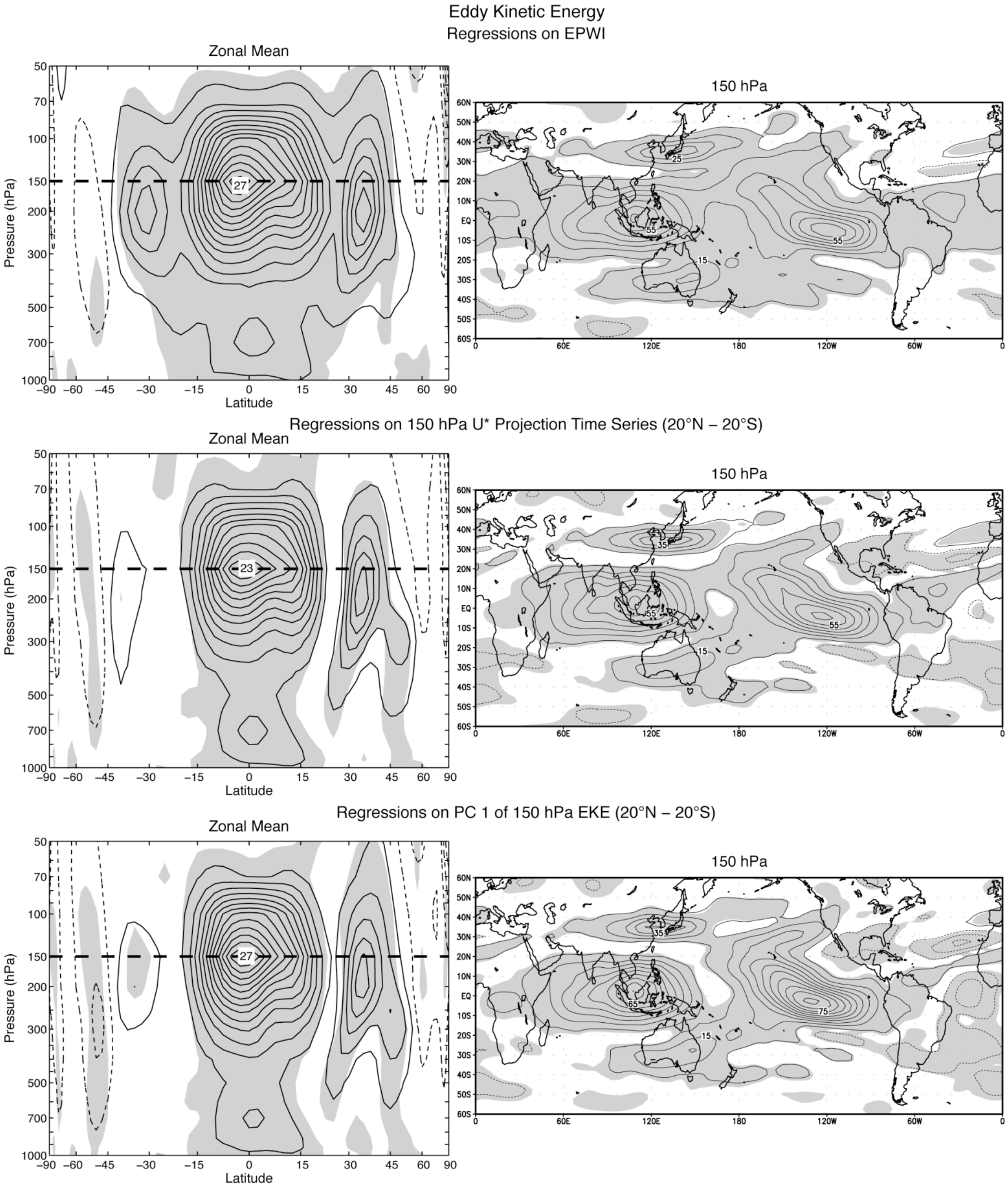

Figure 4.2: Daily-mean eddy kinetic energy anomalies regressed upon (top row) the leading principal component (PC) time series of the daily-mean, zonal-mean eddy kinetic energy anomalies for the region 20ºN – 20ºS (i.e., the EPWI time series), (middle row) the time series of the projection of daily-mean 150-hPa $u*$ anomalies onto the seasonally-varying climatological-mean of 150-hPa $u*$ over the domain 20ºN – 20ºS, and (bottom row) the leading PC time series of the daily-mean 150-hPa eddy kinetic energy anomalies for the region 20ºN – 20ºS. The left column shows regressions of zonal-mean eddy kinetic energy anomalies, and the right column shows regressions of 150-hPa eddy kinetic energy anomalies. Positive contours are solid, and negative contours are dashed. The contour interval is (left) 2 $m^2 s^{-2}$ (–3, –1, 1, 3, …) and (right) 10 $m^2 s^{-2}$ (–15, –5, 5, 15, …). Units are per standard deviation in each time series. The shading indicates regions that are 95% significant. The thick dashed horizontal line in each left panel denotes the level shown in the corresponding right panel.

150 hPa Geopotential Height
Regressions on EPWI

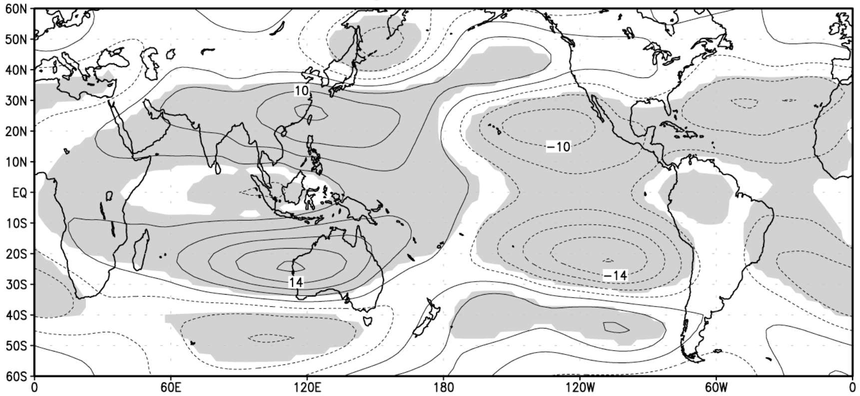

Regressions on 150 hPa U* Projection Time Series (20°N – 20°S)

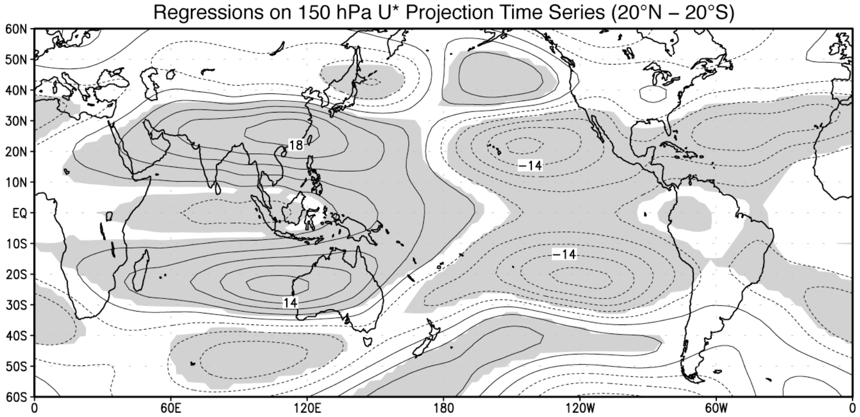

Regressions on PC 1 of 150 hPa EKE (20°N – 20°S)

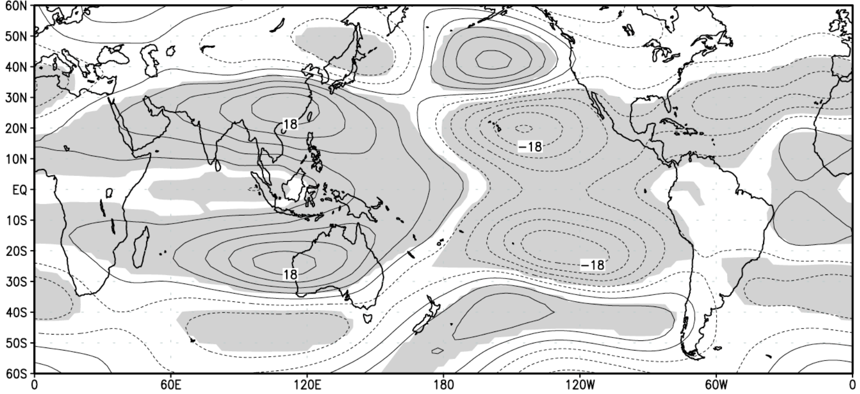

Figure 4.3: As in the right column of Figure 4.2, but for regressions of daily-mean 150-hPa *Z** anomalies. (*Z** denotes the eddy component of the geopotential height field; i.e., the zonal mean has been removed from the geopotential height field.) The contour interval is 4 m (–6, –2, 2, 6, …).

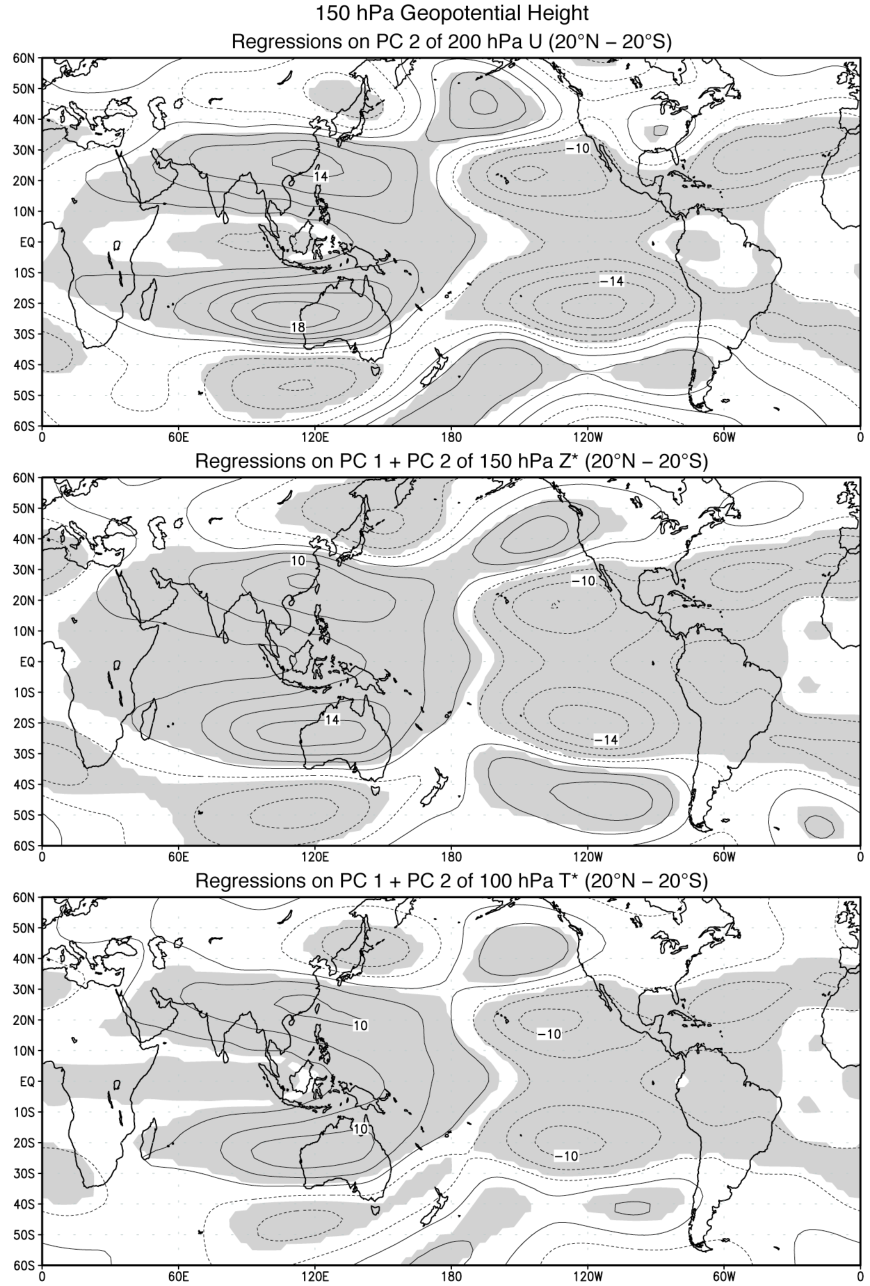

Figure 4.4: As in Figure 4.3, but for regressions on (top) PC 2 of the daily-mean 200-hPa zonal wind anomalies for the region 20ºN – 20ºS, (middle) the sum of the first two PC time series of the daily-mean 150-hPa *Z** anomalies for the region 20ºN – 20ºS, and (bottom) the sum of the first two PC time series of the daily-mean 100-hPa *T** anomalies for the region 20ºN – 20ºS. (*T** denotes the eddy component of the temperature field; i.e., the zonal mean has been removed from the temperature field.)

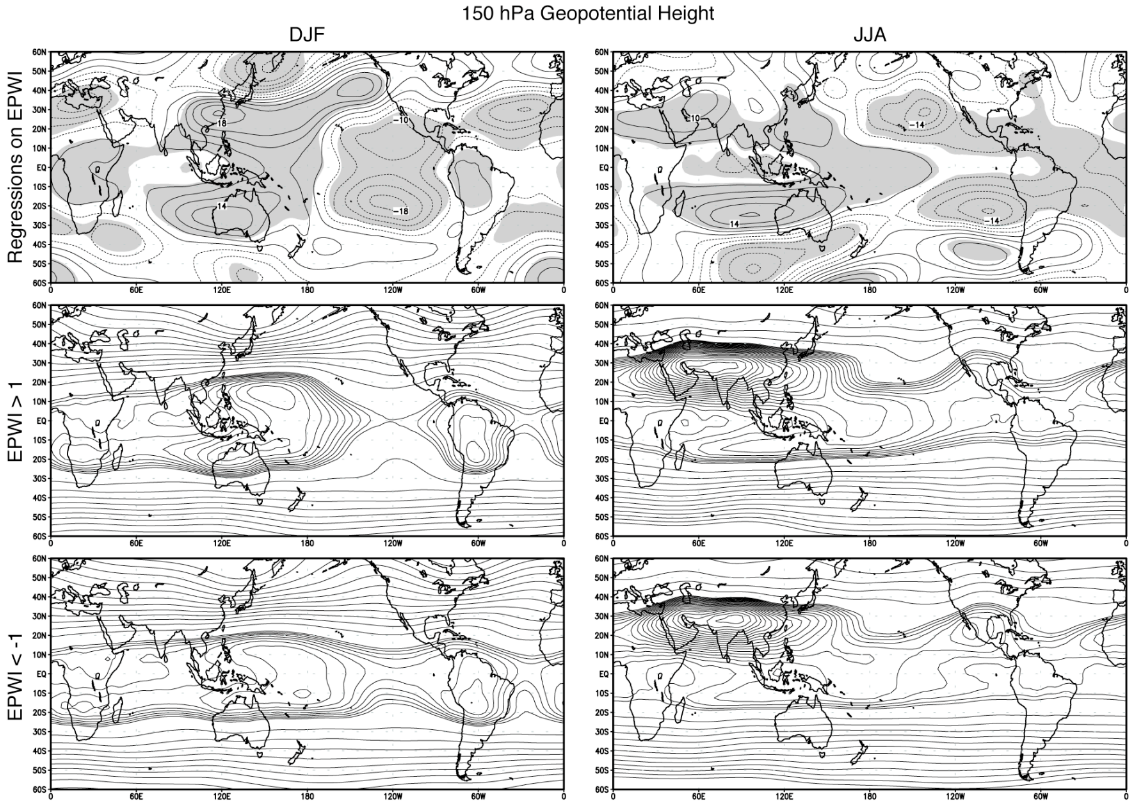

Figure 4.5: (Top row) As in the top panel of Figure 4.3, but for regressions confined to the (left) December-January-February (DJF) and (right) June-July-August (JJA) seasons. (Bottom two rows) Composites of the total (i.e., the zonal mean is not removed) 150-hPa geopotential height field for (middle row) days on which the EPWI time series is greater than +1 standard deviation and (bottom row) days on which the EPWI time series is less than -1 standard deviation. The contour interval in the bottom two rows is 100 m for values less than 14200 m and 10 m for values greater than 14200 m (14100, 14200, 14210, 14220, …).

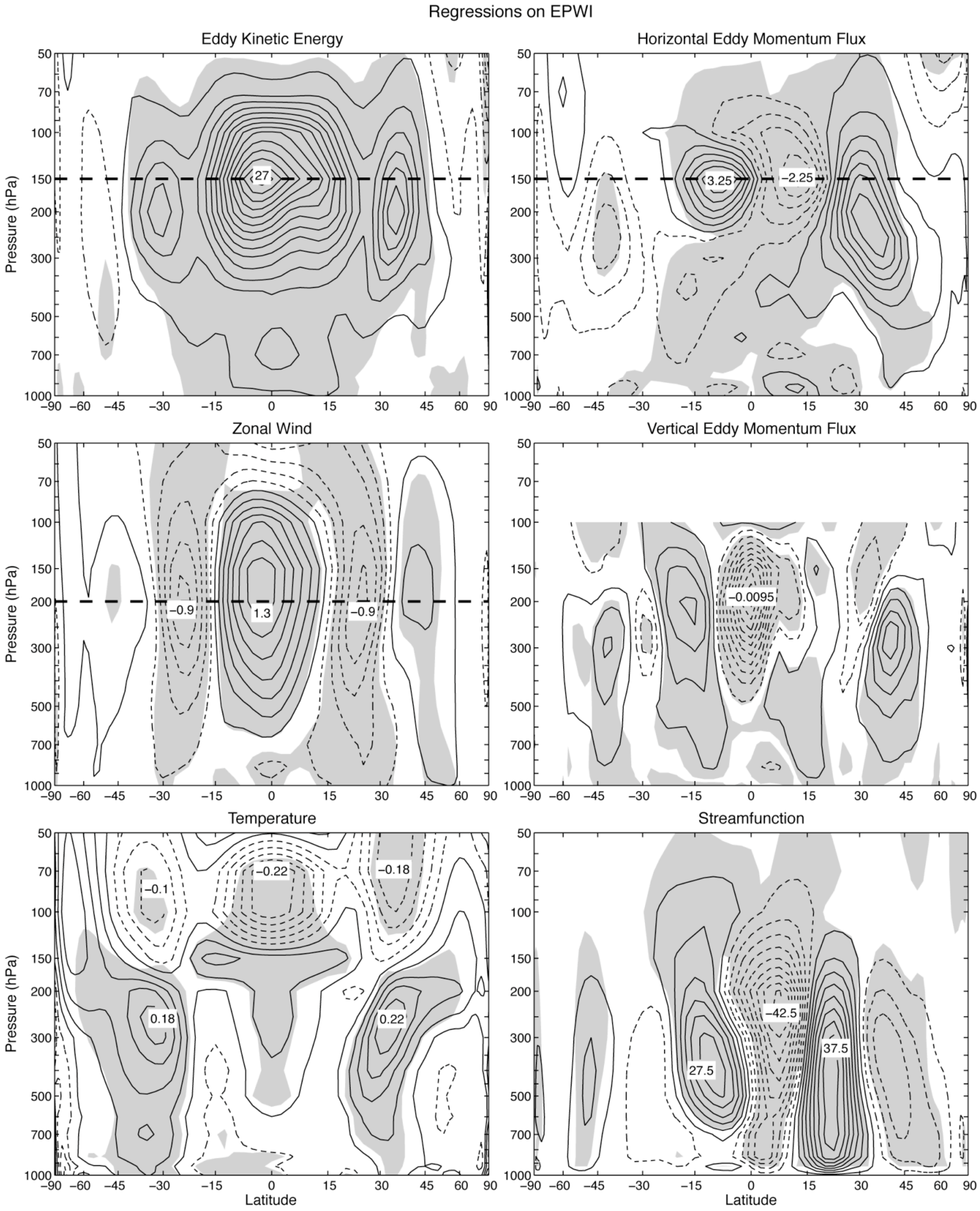

Figure 4.6: Regressions of daily-mean, zonal-mean anomalies on the EPWI time series: (top left) eddy kinetic energy, (top right) meridional eddy momentum flux, (middle left) zonal wind, (middle right) vertical eddy momentum flux, (bottom left) temperature, and (bottom right) mean meridional mass streamfunction (positive values: clockwise circulation). Positive contours are solid, and negative contours are dashed. The contour interval is (top left) 2 $m^2 s^{-2}$ (–3, –1, 1, 3, …), (top right) 0.5 $m^2 s^{-2}$ (–0.75, –0.25, 0.25, 0.75, …), (middle left) 0.2 $m s^{-1}$ (–0.3, –0.1, 0.1, 0.3, …), (middle right) 0.001 $m^2 s^{-2}$ (–0.0015, –0.0005, 0.0005, 0.0015, …), (bottom left) 0.04 K (–0.06, –0.02, 0.02, 0.06, …), and (bottom right) 5 x 10^8 kg s^{-1} (–7.5, –2.5, 2.5, 7.5, …). Units are per standard deviation in the EPWI time series. The shading indicates regions that are 95% significant. The thick dashed horizontal line in the first three panels denotes the level shown in the corresponding panels in Figure 4.7. The contour labels in the bottom right panel are in units of 10^8 kg s^{-1}.

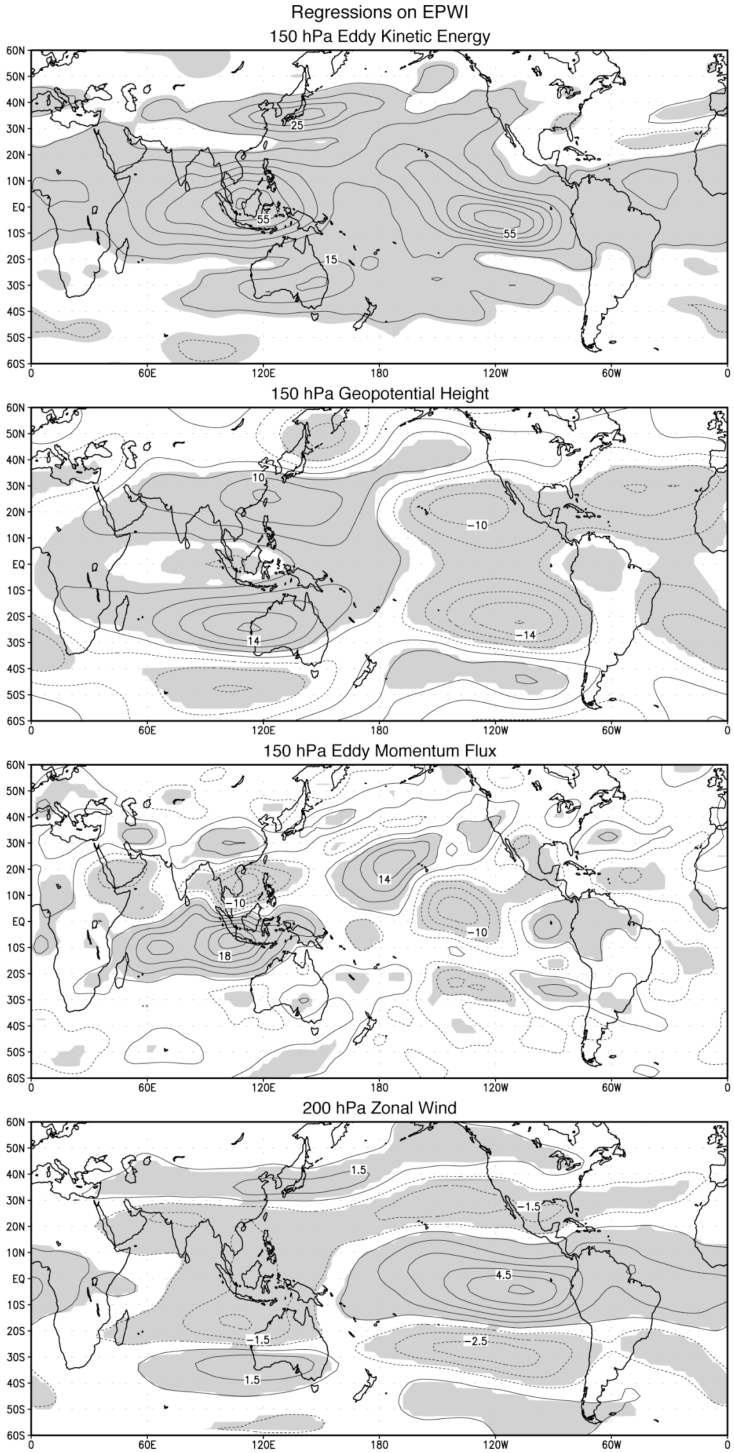
Regressions on EPWI

150 hPa Eddy Kinetic Energy

150 hPa Geopotential Height

150 hPa Eddy Momentum Flux

200 hPa Zonal Wind

Figure 4.7: Regressions of daily-mean anomalies on the EPWI time series: (top panel) 150-hPa eddy kinetic energy, (second panel) 150-hPa Z^*, (third panel) 150-hPa eddy momentum flux, and (bottom panel) 200-hPa zonal wind. Positive contours are solid, and negative contours are dashed. The contour interval is (top panel) 10 $m^2 s^{-2}$ (–15, –5, 5, 15, …), (second panel) 4 m (–6, –2, 2, 6, …), (third panel) 4 $m^2 s^{-2}$ (–6, –2, 2, 6, …), and (bottom panel) 1 $m s^{-1}$ (–1.5, –0.5, 0.5, 1.5, …). Units are per standard deviation in the EPWI time series. The shading indicates regions that are 95% significant.

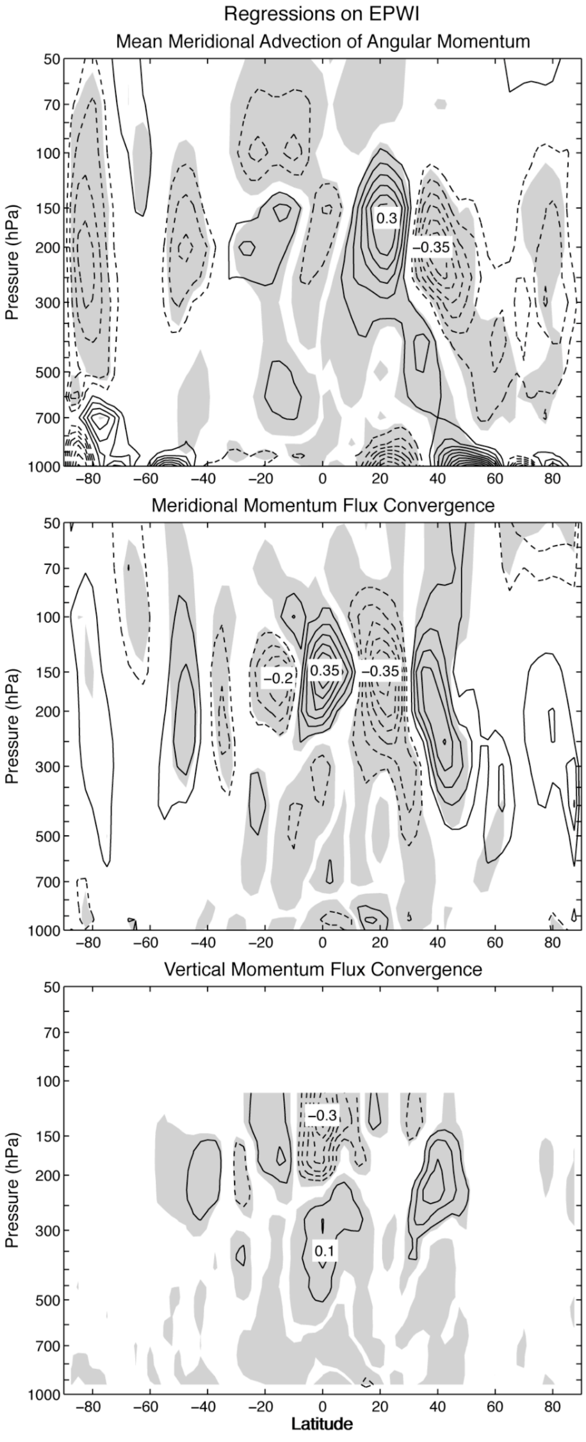

Figure 4.8: Regressions of daily-mean anomalies of terms in the Eulerian mean zonal momentum equation (4.1) on the EPWI time series: (top) advection of angular momentum by the mean meridional flow, (middle) meridional momentum flux convergence, and (bottom) vertical momentum flux convergence. Positive contours are solid, negative contours are dashed, and the zero contour is omitted. The contour interval is 0.05 m s^{-1} day^{-1}. Units are per standard deviation in the EPWI time series. The shading indicates regions that are 95% significant.

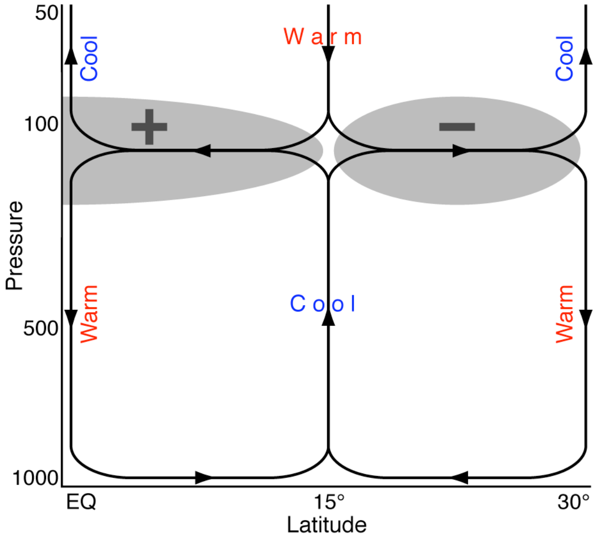

Figure 4.9: Schematic of the transient equatorially symmetric zonal-mean processes associated with variability in equatorial planetary waves. The gray circles signify regions of meridional eddy momentum flux convergence (marked with a plus sign) and meridional eddy momentum flux divergence (marked with a minus sign). The red and blue colors signify adiabatic warming and cooling, respectively. The vertical axis shows pressure levels in units of hPa. For simplicity, the effects of vertical eddy momentum fluxes have been neglected in this schematic.

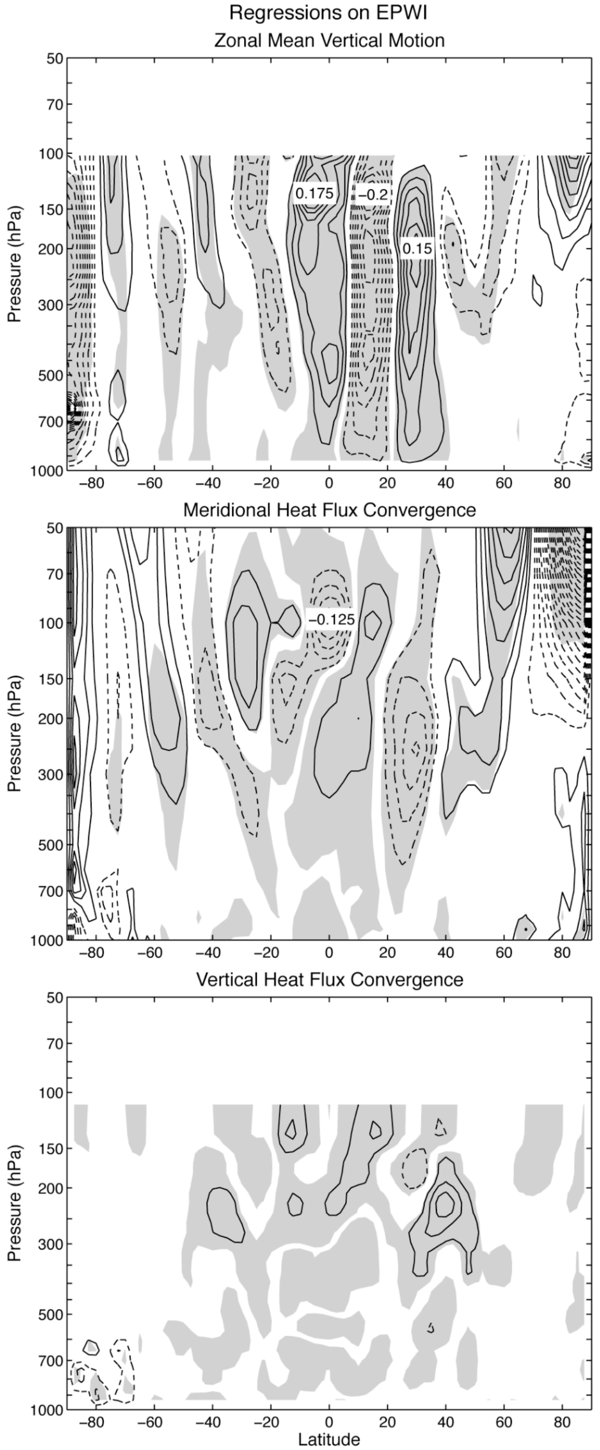

Figure 4.10: As in Figure 4.8, but for the regressions of daily-mean anomalies of terms in the Eulerian mean thermodynamic equation (4.2) on the EPWI time series: (top) mean vertical flow, (middle) meridional heat flux convergence, and (bottom) vertical heat flux convergence. The contour interval is 0.025 K day^{-1}.

Table 4.1: Correlations with the leading principal component (PC) time series of the daily-mean, zonal-mean eddy kinetic energy (EKE) anomalies for the region 20ºN – 20ºS (i.e., the EPWI time series). The correlations are calculated using daily values for the first ten indices and monthly values for the ENSO index time series. All PC and projection time series listed in the table are derived using data from the region 20ºN – 20ºS. The star indicates that the zonal mean has been removed from a field. All correlations listed in the table are 95% significant.

Index	Correlation with EPWI
EPWI derived from 1989–2009 ERA-Interim reanalysis data (Simmons et al. 2007)	0.96
PC 1 of 150 hPa EKE	0.82
PC 2 of 200 hPa U	0.75
Projection onto seasonally varying pattern of 150 hPa U*	0.74
PC 1 of 30–90-day filtered zonal mean EKE	0.70
Sum of MJO Indices	0.66
PC 1 + PC 2 of 150 hPa Z*	0.63
PC 1 + PC 2 of 100 hPa T*	0.61
PC 1 of 90+ day filtered zonal mean EKE	0.55
PC 1 of 0–30-day filtered zonal mean EKE	0.45
Inverted ENSO Index	0.45

Table 4.2: Percent variance in EPWI time series explained by season.

Season	Percent Variance Explained
December-January-February	34.7
March-April-May	22.5
June-July-August	24.8
September-October-November	18.0

CHAPTER 5: ON THE ROLE OF EQUATORIAL PLANETARY WAVES IN CLIMATE VARIABILITY AND TRENDS

The results in the previous two chapters 1) document climatological-mean static stability structures near the tropical tropopause that resemble equatorial planetary waves and 2) establish the robustness of an index time series that measures non-seasonal variations in the equatorial planetary waves (i.e., the EPWI time series). In this chapter, the EPWI time series is used to interpret climate variability and trends, both in the tropical troposphere and in the tropical tropopause region. Section 5.1 examines the signatures of variability in the equatorial planetary waves in the outgoing longwave radiation (OLR) and sea surface temperature fields. Section 5.2 then discusses the relevant timescales associated with the EPWI time series and explores the linkages between variability in the equatorial planetary waves, the El Niño-Southern Oscillation (ENSO), and the Madden-Julian Oscillation (MJO). Section 5.3 describes the relationships between the equatorial planetary waves and long-term changes in troposphere/stratosphere exchange and the width of the tropical belt. Section 5.4 then examines signatures of variability in the equatorial planetary waves in the fine-scale static stability structures near the tropical tropopause. Concluding remarks are provided in Section 5.5.

5.1 Signature of the EPWI in OLR and sea surface temperatures

Variability in the amplitude of the equatorial planetary waves is presumably associated with variability in convective heating. To confirm this, the top panel of Figure 5.1 shows the regressions of daily-mean OLR anomalies onto the standardized EPWI time series. Periods of anomalously large equatorial planetary wave amplitude (i.e., the positive polarity of the EPWI time series) are associated with enhanced convection (negative OLR anomalies) over the Maritime Continent and western tropical Pacific Ocean and suppressed convection (positive OLR anomalies) over the Indian Ocean and the eastern tropical Pacific Ocean. As revealed in the next section, the dipole in OLR anomalies between the western and eastern tropical Pacific Ocean is reminiscent of that associated with ENSO, and the dipole in OLR anomalies between the tropical Indian Ocean and the Maritime Continent is reminiscent of the MJO.

The bottom panel of Figure 5.1 shows the corresponding regressions for monthly-mean sea surface temperature anomalies. Periods of enhanced equatorial planetary wave amplitude are associated with warm sea surface temperature anomalies over the mid-latitude Pacific Ocean in each hemisphere and cold sea surface temperature anomalies over the eastern equatorial Pacific Ocean. The tropical sea surface temperature anomalies bear strong resemblance to those associated with ENSO (e.g., Rasmusson and Carpenter 1982).

5.2 Timescales and linkages to ENSO and MJO

The relationship between variability in the amplitude of the equatorial planetary waves, ENSO, and the MJO is examined in greater detail in this section. The section first discusses the relevant timescales that contribute to the structures associated with the EPWI time series. The section then presents a detailed comparison between the structures associated with the EPWI time series and those associated with ENSO and the MJO.

5.2.1 Timescales

The timescales contributing to the structures associated with the EPWI time series are explored in Figures 5.2–5.4. The top rows in the three figures are identical: all show the regressions of zonal-mean eddy kinetic energy and zonal wind (top left) and zonally varying 150-hPa eddy kinetic energy and OLR (top right) onto the standardized EPWI time series (the results are reproduced from Chapter 4 to aid in the comparison between panels). The second rows of Figures 5.2–5.4 show the same fields as the top rows, but in this case, the basis for the regressions is the standardized leading PC time series of time-filtered, zonal-mean eddy kinetic energy anomalies between 20ºN and 20ºS (recall that the EPWI time series is the leading PC time series of *unfiltered* zonal-mean eddy kinetic energy anomalies between 20ºN and 20ºS). The results in the second row of Figure 5.2 are based on 90-day low-pass filtered data, the results in the second row of Figure 5.3 are based on 30–90-day band-pass filtered data, and the results in the second row of Figure 5.4 are based on 30-day high-pass filtered data.

The patterns associated with the leading PC time series of the 90-day low-pass filtered eddy kinetic energy field (Figure 5.2, second row) and the 30–90-day band-pass filtered eddy kinetic energy field (Figure 5.3, second row) bear strong resemblance to the patterns associated with the EPWI time series (Figures 5.2 and 5.3, top row). Thus, the structures associated with the EPWI time series arise as the leading patterns of wavelike variability on both intraseasonal and interannual timescales. The primary differences between the structures associated with the EPWI time series and the regressions based on the PCs of time-filtered eddy kinetic energy are found in the subtropics, where the zonal-mean zonal wind anomalies are noticeably larger on timescales longer than 90 days (i.e., compare the middle left panels in Figures 5.2 and 5.3). Other notable differences include: 1) a westward shift in the 150-hPa eddy kinetic energy anomalies over the eastern Pacific Ocean on timescales longer than 90 days and 2) the absence of OLR anomalies over the cold tongue region of the eastern tropical Pacific Ocean on intraseasonal timescales.

The patterns associated with the leading PC time series of the 30-day high-pass filtered eddy kinetic energy field (Figure 5.4, second row) bear little resemblance to the patterns associated with the EPWI time series (Figure 5.4, top row). The regression patterns in Figure 5.4 (second row) are characterized by eddy kinetic energy anomalies in the subtropical upper troposphere that arise predominantly from the longitudes of the Pacific Ocean. The eddy kinetic energy anomalies are associated with zonal jet shifts in the subtropics and have little coherent relationship with tropical convection.

Because the patterns in Figure 5.4 (second row) possess only weak tropical signatures, the results suggest that the equatorial planetary wave structures associated with the EPWI time series emerge primarily from timescales greater than 30 days (see also correlations in Table 4.1). To confirm this, the power spectrum of the EPWI time series is shown in Figure 5.5. The power spectrum indicates that the EPWI time series exhibits statistically significant spectral power at periods of 1–2 months, with the largest spectral peak between 50–60 days. As discussed below, the spectral peak at intraseasonal timescales is consistent with the relationship between the EPWI time series and the MJO (e.g., Madden and Julian 1994). However, the EPWI time series also exhibits statistically significant spectral power at periods of ~10–30 days. The nature of the sub-monthly variance is less coherent. Regressions on a 30-day high-pass filtered version of the EPWI time series depict similar structures to those shown in Figure 5.4 (second row).

5.2.2 Relationships with ENSO and MJO

The bottom rows of Figures 5.2 and 5.3 show the same fields as the top two rows, but in this case, the basis for the regressions is inverted values of the ENSO index time series (Figure 5.2, bottom row) and an index of the MJO (Figure 5.3, bottom row). The ENSO index time series is inverted (i.e., multiplied by –1) so that the regression coefficients correspond to cold sea surface temperature anomalies in the eastern tropical Pacific Ocean. The index of the MJO is motivated by Figure 5.6. Figure 5.6 shows scatter plots of daily values of the EPWI time series plotted as a function of the orthogonal “RMM” MJO indices (the details of the indices are given in Wheeler and Hendon 2004). The top panel indicates days when the EPWI time series is greater than +1 standard deviation; the bottom panel indicates days when the EPWI time series is less than –1 standard deviation. Figure 5.6 illustrates that 1) enhanced amplitude in the equatorial planetary waves occurs with greatest frequency during MJO phases 5 and 6 (i.e., when the MJO is associated with peak and decaying convection just to the west of the International Date Line) and 2) suppressed amplitude in the equatorial planetary waves occurs with greatest frequency during MJO phases 1 and 2 (i.e., when convection is suppressed over the Maritime Continent and the western tropical Pacific Ocean). Thus, the strongest relationship between the MJO and the EPWI time series occurs along the diagonal axis through MJO phases 1, 2, 5, and 6. (The MJO also has its greatest influence on atmospheric angular momentum during similar phases; see previous work by Madden 1987 and Weickmann et al. 1997.) The regressions in the bottom row of Figure 5.3 are based on the linear sum of the paired RMM indices and hence correspond to regressions along the diagonal in Figure 5.6.

Comparing the three rows in Figures 5.2 and 5.3, it is clear that variability in the amplitude of the equatorial planetary waves not only emerges as the leading pattern of wavelike variability on intraseasonal and interannual timescales (middle rows), but also projects strongly onto ENSO (Figure 5.2, bottom row) and the MJO during its phases 5 – 6 (Figure 5.3, bottom row). A similar relationship between the equatorial planetary waves and ENSO was shown in Dima and Wallace (2007), who examined the wavelike component of the tropical circulation in composites based on the phase of ENSO; and a similar wavelike structure is evident in composites of the MJO during its phases 5 – 6 (cf. Figures 8 and 9 of Wheeler and Hendon 2004; see also Figure 4 of Hendon and Salby 1994). Consistent with the results in the middle rows of Figures 5.2 and 5.3, the most pronounced differences between the structures in the bottom rows of Figures 5.2 and 5.3 are found in the subtropics, where ENSO has a much larger projection onto the zonal-mean zonal wind field than the MJO (i.e., compare the bottom left panels in Figures 5.2 and 5.3). Other notable differences include: 1) weaker zonal-mean eddy kinetic energy anomalies associated with ENSO in the deep tropics, 2) a slight westward shift in the 150-hPa eddy kinetic energy anomalies associated with ENSO over the Pacific Ocean, 3) oppositely-signed 150-hPa eddy kinetic energy anomalies associated with ENSO over the Atlantic Ocean, and 4) the absence of OLR anomalies associated with the MJO over the cold tongue region of the eastern tropical Pacific Ocean.

The high degree of resemblance between the structures associated with the MJO and those associated with variability in the equatorial planetary waves suggests that the MJO can be viewed as consisting of two components: 1) a stationary component that is linearly congruent with variability in the amplitude of the equatorial planetary waves and 2) a propagating component that is linearly unrelated to variability in the amplitude of the equatorial planetary waves. The decomposition of the MJO into these two components is shown in Figure 5.7.

The left column of Figure 5.7 shows the regressions of OLR and 150-hPa Z^* anomalies onto linear combinations of the Wheeler and Hendon (2004) RMM indices. The results are organized such that the top panel corresponds to the phase of the MJO that is characterized by anomalous convection to the south of India, and subsequent panels indicate the eastward progression of the anomalous convection across the Maritime Continent (e.g., see also Figure 5.6). As documented extensively in the literature, the convective anomalies associated with the MJO are accompanied by upper tropospheric geopotential height anomalies that resemble the equatorial wave response to a localized tropical heating anomaly (e.g., Hendon and Salby 1994).

The middle column of Figure 5.7 shows the contribution of the equatorial planetary waves to the structure of the MJO as a function of MJO phase; the right column shows the component of the MJO that is linearly uncorrelated with variability in the equatorial planetary waves (as defined by the EPWI time series). As noted earlier, variability in the amplitude of the climatological-mean pattern of equatorial planetary waves does not contribute substantially to the structure of the MJO when the anomalous convection is located over the eastern Indian Ocean (Figure 5.6; second row of Figure 5.7). But the projection is notable otherwise, particularly in the upper tropospheric Z^* field (top row and bottom two rows of Figure 5.7). For example, when the anomalous convection is centered over the Maritime Continent (bottom two rows of Figure 5.7), the equatorial planetary waves account for a substantial fraction of the structure of the MJO in both the OLR and upper tropospheric Z^* fields (e.g., compare the left and middle columns in Figure 5.7).

5.3 Relevance for tropical climate trends

As discussed in the previous section, equatorial planetary waves exhibit substantial variability on intraseasonal and interannual timescales. As evidenced in a plot of the EPWI time series (Figure 5.8, left), equatorial planetary waves also exhibit variability on decadal timescales. The trend in the EPWI time series over the period 1979 – 2009 is not statistically significant at the 95% level, and trends derived from reanalysis data sets should always be treated with caution. But it is nevertheless clear from Figure 5.8 that in the NCEP–NCAR reanalysis data: 1) the amplitudes of the equatorial planetary waves (as measured by the EPWI time series) are larger over the last ~10 years than during the 1980s and 1990s (Figure 5.8, left) and 2) the eddy kinetic energy in the deep tropics (equatorward of 10º latitude) has increased over the past three decades within a narrow region near the cold point tropopause level (Figure 5.8, right). (Similar behavior is also observed in ERA-Interim reanalysis data.) Interestingly, the timing of the increase in the EPWI time series (and in the eddy kinetic energy near the tropical tropopause) is reminiscent of that associated with recent changes in stratospheric water vapor (e.g., Randel et al. 2006; Solomon et al. 2010) and the width of the tropical belt (cf. Figure 1 of Johanson and Fu 2009). The remainder of this section examines to what extent the weak but apparent trend in the amplitude of the equatorial planetary waves has contributed to the observed trends in these fields.

5.3.1 Stratospheric water vapor

As discussed in Section 1.3.2, transport across the tropical tropopause largely controls the concentration of water vapor in the lower stratosphere (e.g., Brewer 1949; Mote et al. 1996; Fueglistaler et al. 2009). Because of the cold temperatures encountered near the tropical tropopause, stratospheric water vapor concentrations are quite small (~5 ppmv), and current instrumentation is unable to resolve the small absolute values of stratospheric water vapor with any certainty (e.g., Fueglistaler et al. 2009). Thus, an accurate assessment of decadal-scale changes in stratospheric water vapor remains challenging. Nonetheless, stratospheric water vapor was thought to be increasing prior to 2001 (e.g., Rosenlof et al. 2001), when it exhibited a dramatic step-like decrease in values during the early 2000s (e.g., Randel et al. 2006; Rosenlof and Reid 2008; Solomon et al. 2010). The recent decrease in stratospheric water vapor was largest in the lowermost tropical and subtropical stratosphere (Solomon et al. 2010) and is consistent with a recent decrease in tropical tropopause temperatures (e.g., Randel et al. 2006; Rosenlof and Reid 2008; Solomon et al. 2010), a recent decrease in ozone values in the lowermost tropical stratosphere (Randel et al. 2006), and thus presumably a recent increase in tropical upwelling in the lowermost stratosphere (Randel et al. 2006; Rosenlof and Reid 2008). Interestingly, a concurrent increase in western tropical Pacific sea surface temperatures is also observed (Rosenlof and Reid 2008; Solomon et al. 2010).

Previous studies have proposed a link between the step-like increase in western tropical Pacific sea surface temperatures over the last decade and the similar step-like decrease in tropical tropopause temperatures and stratospheric water vapor concentrations in the early 2000s (e.g., Rosenlof and Reid 2008; Solomon et al. 2010). The increase in values in the EPWI time series since 2000 (Figure 5.8, left) is consistent with this hypothesis, as warmer sea surface temperatures could feasibly enhance the amplitudes of equatorial planetary waves and thus enhance upwelling across the tropical tropopause (e.g., Deckert and Dameris 2008; Calvo and Garcia 2009). However, the observational evidence for a linkage between equatorial planetary waves and upwelling in the lower tropical stratosphere remains inconclusive (Ueyama and Wallace 2010).

The results in Figure 5.1 (bottom) support a link between variability in equatorial planetary waves and sea surface temperatures in the western tropical Pacific Ocean. But there does not appear to be a definitive link between variability in equatorial planetary waves and stratospheric water vapor. For example, Figure 5.9 shows the regressions of daily-mean Aura MLS water vapor anomalies (averaged over 20ºN – 20ºS) upon the standardized EPWI time series for the period 2005 – 2009. Periods of enhanced amplitude in the equatorial planetary waves are associated with reduced water vapor mixing ratios in the tropical upper troposphere, particularly during the period following peak amplitude in the EPWI time series. The upper tropospheric water vapor anomalies appear to pulse on a timescale of 40 – 50 days and are reminiscent of the water vapor anomalies associated with the MJO (e.g., Mote et al. 1998; Mote et al. 2000). However, the region of significant water vapor anomalies does not extend above the tropopause level (Figure 5.9). Nevertheless, the results in Figure 5.9 do not preclude equatorial planetary waves from playing a role in the recent stratospheric water vapor changes. Because stratospheric water vapor anomalies represent the integrated signal of tropical tropopause temperature anomalies (e.g., Randel et al. 2004), the tropical tropopause temperature anomalies associated with variability in the equatorial planetary waves (Figure 4.6, bottom left) may only be relevant for stratospheric water vapor concentrations for lower frequency variability than that shown in Figure 5.9.

5.3.2 Width of the tropics

Recent evidence has suggested that the width of the tropics has expanded over the last several decades (e.g., Fu et al. 2006; Hudson et al. 2006; Seidel and Randel 2007; Hu and Fu 2007; Seidel et al. 2008). The widening of the tropics is characterized by a poleward expansion of the Hadley circulation (e.g., Hu and Fu 2007) and thus a poleward shift in the latitude of the upper tropospheric subtropical zonal jet (e.g., Fu et al. 2006) and the subtropical dry zones (e.g., Hu and Fu 2007). Interestingly, many of these same features are present in the regressions on the EPWI time series shown in Chapter 4 (Figure 4.6). The deep easterly zonal wind anomalies in the subtropics (Figure 4.6, middle left) are characteristic of a poleward shift in the subtropical zonal jets, and the positive temperature anomalies in the subtropical troposphere (Figure 4.6, bottom left) are reminiscent of a poleward shift in the subsiding branches of the Hadley circulation.

Has variability in the equatorial planetary waves contributed to fluctuations and trends in the width of the tropical belt (e.g., Fu et al. 2006; Seidel et al. 2008)? Figure 5.10 shows the regression onto the EPWI time series of two measures of the width of the tropics: the transition between zonal-mean easterlies and westerlies at the surface (top) and the 250 W m^{-2} OLR threshold used to denote the subtropical dry zones (bottom; e.g., Hu and Fu 2007). (Note that the results in Figure 5.10 are regressions on the full EPWI time series: i.e., they are not trends.) At first glance, variability in the equatorial planetary waves appears to have only a weak signature in both measures of the width of the tropics (Figure 5.10). But on closer inspection, a +1 standard deviation change in the EPWI time series is associated with a widening of the tropical belt by ~0.5º latitude based on the surface wind measure (Figure 5.10, top) and ~0.25º latitude based on the OLR measure (Figure 5.10, bottom). The sign of the results is consistent with the relationships between ENSO and the width of the tropical belt (e.g., Seager et al. 2003; Lu et al. 2008) and between the MJO and the width of the Hadley circulation within select longitude bands (e.g., Hendon and Liebmann 1990a, b).

Figure 5.10 reveals that equatorial planetary waves are linked to changes in the width of the tropics on intraseasonal and interannual timescales. In general, the results are consistent with the temperature and streamfunction anomalies associated with the EPWI time series shown in Figure 4.6. However, to the extent that the trend in the EPWI time series is reliable, the contribution of the equatorial planetary waves to decadal variability in the width of the tropics is very small. For example: the trend in the EPWI time series is 0.09 standard deviations per decade, and thus the trend in the EPWI time series can account for only ~0.09 std/decade x 0.5º latitude/std, or ~0.05º latitude per decade change in the width of the tropics. In contrast, the observed trends are on the order of ~0.8º – 2º latitude per decade (e.g., Seidel et al. 2008). Nonetheless, if reanalysis data underestimate the amplitude of the trend in the EPWI time series, it is possible that equatorial planetary waves play a more prominent role in trends in the width of the tropics than indicated here.

5.4 Signature of the EPWI in the tropical TIL

The results in Chapter 3 demonstrate that the climatological-mean structure of the tropopause inversion layer (TIL) in the tropics strongly resembles the long-term mean pattern of equatorial planetary waves. This section examines whether a similar relationship exists between variability in the amplitude of the equatorial planetary waves (as measured by the EPWI time series) and variability in the amplitude of the structures in the tropical TIL. As in Chapter 3, the results are displayed in tropopause-relative coordinates. However, the results in this section are derived using COSMIC GPS radio occultation temperature profiles, which have improved spatial density over the CHAMP profiles used in Chapter 3 (see Section 2.1.1).

Figure 5.11 shows the regressions of five-day-mean, zonal-mean COSMIC static stability anomalies upon the standardized EPWI time series for the period 2007 – 2010. Periods of enhanced amplitude in the equatorial planetary waves are associated with positive static stability anomalies in a narrow layer immediately above the tropical tropopause and negative off-equatorial static stability anomalies ~2 km above the tropopause. Thus, variability in the equatorial planetary waves projects onto both features of the tropical TIL: 1) the shallow static stability maximum centered ~0–1 km above the tropopause and 2) the paired static stability maxima centered between 10° and 20° latitude in both hemispheres and located ~1–3 km above the tropopause (e.g., Figure 3.2). Nonetheless, it is somewhat surprising that variability in the equatorial planetary waves is associated with oppositely signed static stability anomalies in the two layers of the tropical TIL.

To better understand the results shown in Figure 5.11, Figure 5.12 shows the regression onto the EPWI time series of five-day-mean COSMIC static stability anomalies averaged over two layers: 0–1 km above the tropopause and 1–3 km above the tropopause (i.e., the results in Figure 5.12 are displayed in a similar format to those in Figure 3.10). The results reveal that the positive static stability anomalies ~0–1 km above the tropopause in Figure 5.11 arise primarily from the western Pacific Ocean sector (Figure 5.12, top), whereas the negative static stability anomalies ~1–3 km above the tropopause in Figure 5.11 arise primarily from the eastern Pacific Ocean sector (Figure 5.12, bottom). Consistent with the climatology (Figures 3.10 and 3.11, left columns), the positive static stability anomalies in the 0–1 km layer are co-located with negative cold point tropopause temperature anomalies (Figure 5.13). But in contrast to the climatology (Figures 3.10 and 3.11, right columns), the zonal-mean static stability anomalies in the 1–3 km layer are not driven by modulations in amplitude of the upper tropospheric anticyclones over the western Pacific Ocean. Instead, the negative zonal-mean static stability anomalies in the 1–3 km layer are associated with anomalous upper tropospheric cyclones over the eastern Pacific Ocean (Figure 4.3, top). Thus, the longitudinal extent of the upper tropospheric anticyclones over the western Pacific Ocean appears to be a crucial factor in determining the variability of the zonal-mean static stability structures ~1–3 km above the tropical tropopause.

5.5 Conclusions

Periods of anomalously large equatorial planetary wave amplitude (i.e., the positive polarity of the EPWI time series) are marked by enhanced convection over the Maritime Continent and western tropical Pacific Ocean, suppressed convection over the Indian Ocean and eastern tropical Pacific Ocean, and sea surface temperature anomalies that are reminiscent of the cold phase of the ENSO cycle (Figure 5.1). The variability in the equatorial planetary waves emerges largely from interannual and intraseasonal timescales (Figures 5.2 and 5.3), and the EPWI time series exhibits a spectral peak at periods of 50–60 days (Figure 5.5). Thus, the equatorial planetary waves project strongly onto not only ENSO, but also onto the MJO during periods when the anomalous convection is centered near the Maritime Continent (Figures 5.3 and 5.6). As a result, it is argued that the MJO can be viewed as the linear superposition of two distinct phenomena: 1) a stationary component that is linearly congruent with variability in the amplitude of the equatorial planetary waves and 2) a propagating component that is linearly unrelated to variability in the amplitude of the equatorial planetary waves. Past studies have shown that the MJO cannot be interpreted solely as a Kelvin wave (e.g., Hsu 1996; Zhang 2005). They have also shown that the MJO cannot be thought of as a standing oscillation in convection that excites a propagating circulation anomaly (Zhang and Hendon 1997). But the results shown here suggest that the equatorial planetary waves excited by the MJO may act to alias the propagating signature of the MJO. The implications of the results for theories of the MJO remain to be determined.

Variability in the equatorial planetary waves is also important for interpreting other aspects of tropical climate variability. For example, the signature of the equatorial planetary waves in tropical tropopause temperatures (Figure 4.6, bottom left) suggests that they play a role in driving variability in troposphere/stratosphere exchange (see also Norton 2006), and the signature of the waves in the subtropical wind and temperature fields reveals that they play a role in driving variability in the width of the tropics (Figure 5.10). The preliminary analyses shown here suggest that the equatorial planetary waves are not strongly linked to trends in either stratospheric water vapor or two measures of the width of the tropics. But trends in reanalysis data are notoriously unreliable in the tropics, and thus more detailed future work will be necessary to determine the relevance of equatorial planetary waves for these and other forms of tropical decadal climate variability.

Finally, variability in the equatorial planetary waves is linked to variability in the fine-scale static stability structures of the tropical TIL. Periods of enhanced amplitude in the equatorial planetary waves are associated with 1) a shallow equatorially-centered region of positive static stability anomalies in the ~0–1 km layer above the tropical tropopause and 2) paired off-equatorial regions of negative static stability anomalies in the ~1–3 km layer above the tropical tropopause (Figure 5.11). The positive static stability anomalies in the lower layer of the tropical TIL are co-located with negative cold point tropopause temperature anomalies (Figure 5.12, top; Figure 5.13), and the negative static stability anomalies in the upper layer of the tropical TIL arise largely from the anomalous upper tropospheric cyclones over the eastern Pacific Ocean (Figure 4.3, top; Figure 5.12, top). Thus, equatorial planetary waves appear to play an important role in driving variability in the amplitude of both the ~0–1 km and ~1–3 km features of the tropical TIL. However, the results shown here do not preclude the role of other processes. Because variability in the equatorial planetary waves is associated with variability in tropical convection (Figure 5.1, top), radiative cooling from convective or cirrus clouds in the tropical tropopause layer could also play an appreciable role in forcing the static stability anomalies in Figures 5.11 and 5.12, particularly in the ~0–1 km layer.

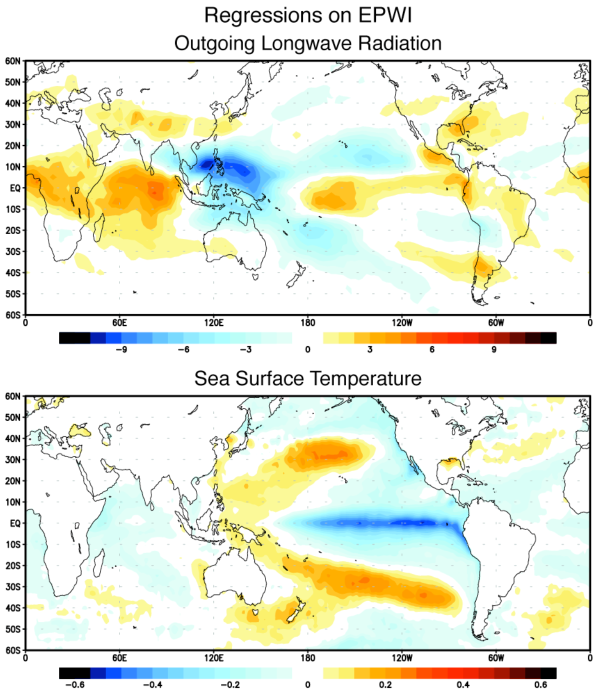

Regressions on EPWI

Outgoing Longwave Radiation

Sea Surface Temperature

Figure 5.1: Regressions on the leading principal component (PC) time series of the daily-mean, zonal-mean eddy kinetic energy anomalies for the region 20ºN – 20ºS (i.e., the EPWI time series): (top) daily-mean outgoing longwave radiation (OLR) anomalies (from NOAA Interpolated OLR data set) and (bottom) monthly-mean sea surface temperature anomalies (from NOAA Optimal Interpolation Version 2 sea surface temperature data set). The contour interval is (top) 0.75 W m^{-2} and (bottom) 0.04 ºC. Units are per standard deviation in the EPWI time series. Unless otherwise noted, all figures in this chapter are based on NCEP–NCAR reanalysis data and are derived from data covering the period 1979–2009; the bottom panel and all subsequent panels that use sea surface temperature data are based upon the period 1982–2009.

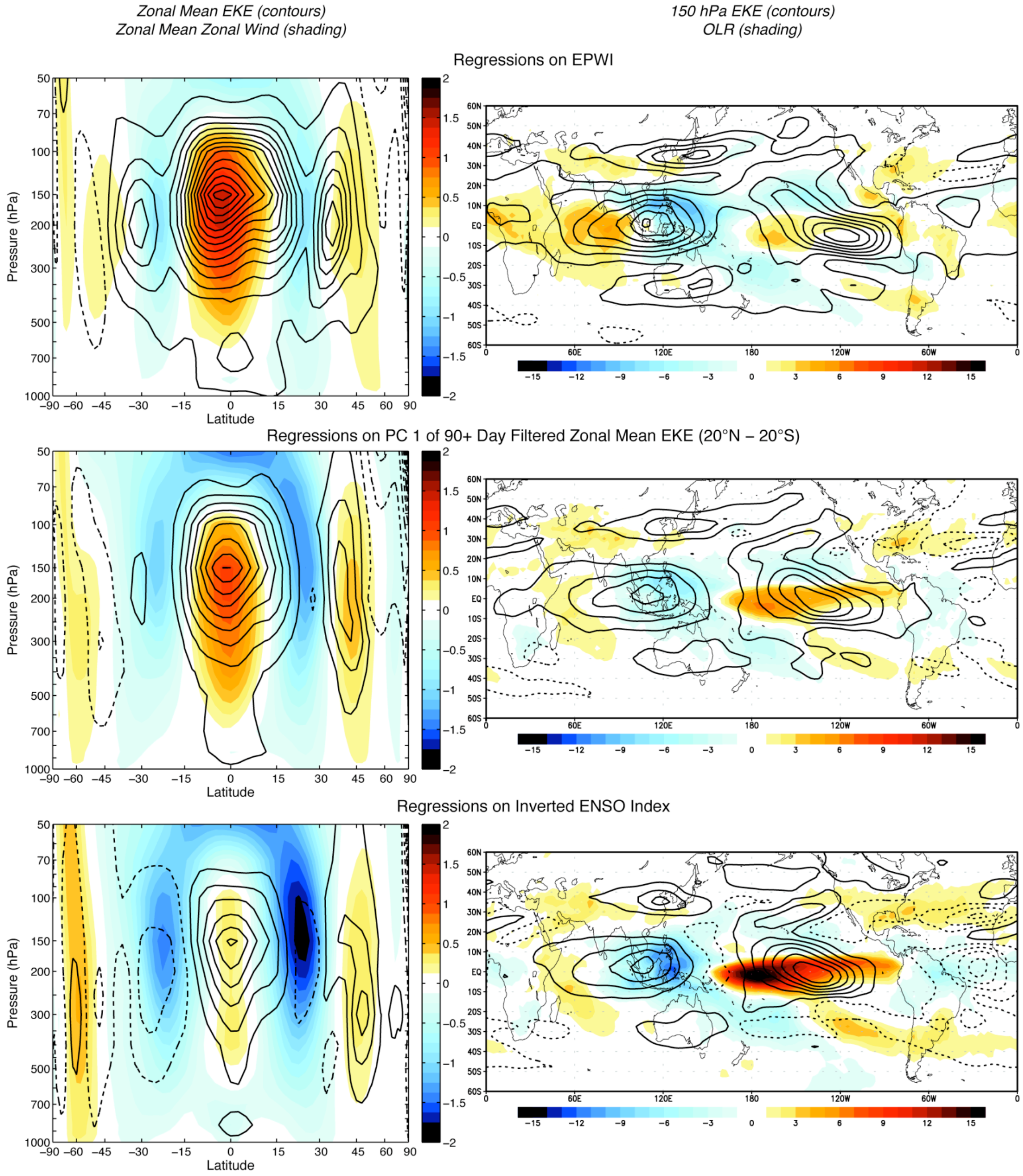

Figure 5.2: Regressions on (top row) the EPWI time series, (middle row) the leading PC time series of the 90-day low-pass filtered daily-mean, zonal-mean eddy kinetic energy anomalies for the region 20ºN – 20ºS, and (bottom row) the inverted (i.e., multiplied by -1) ENSO index time series. The black contours represent (left) zonal-mean eddy kinetic energy anomalies and (right) 150-hPa eddy kinetic energy anomalies. Positive contours are solid, and negative contours are dashed. The contours are plotted at the same intervals as in Figures 4.6 and 4.7. The colored shading represents (left) zonal-mean zonal wind anomalies and (right) outgoing longwave radiation anomalies (from NOAA Interpolated OLR data set). The shading interval is (left) 0.125 m s^{-1} and (right) 1 W m^{-2}. Units are per standard deviation in each time series. The regressions on the ENSO index are performed using monthly-mean anomalies.

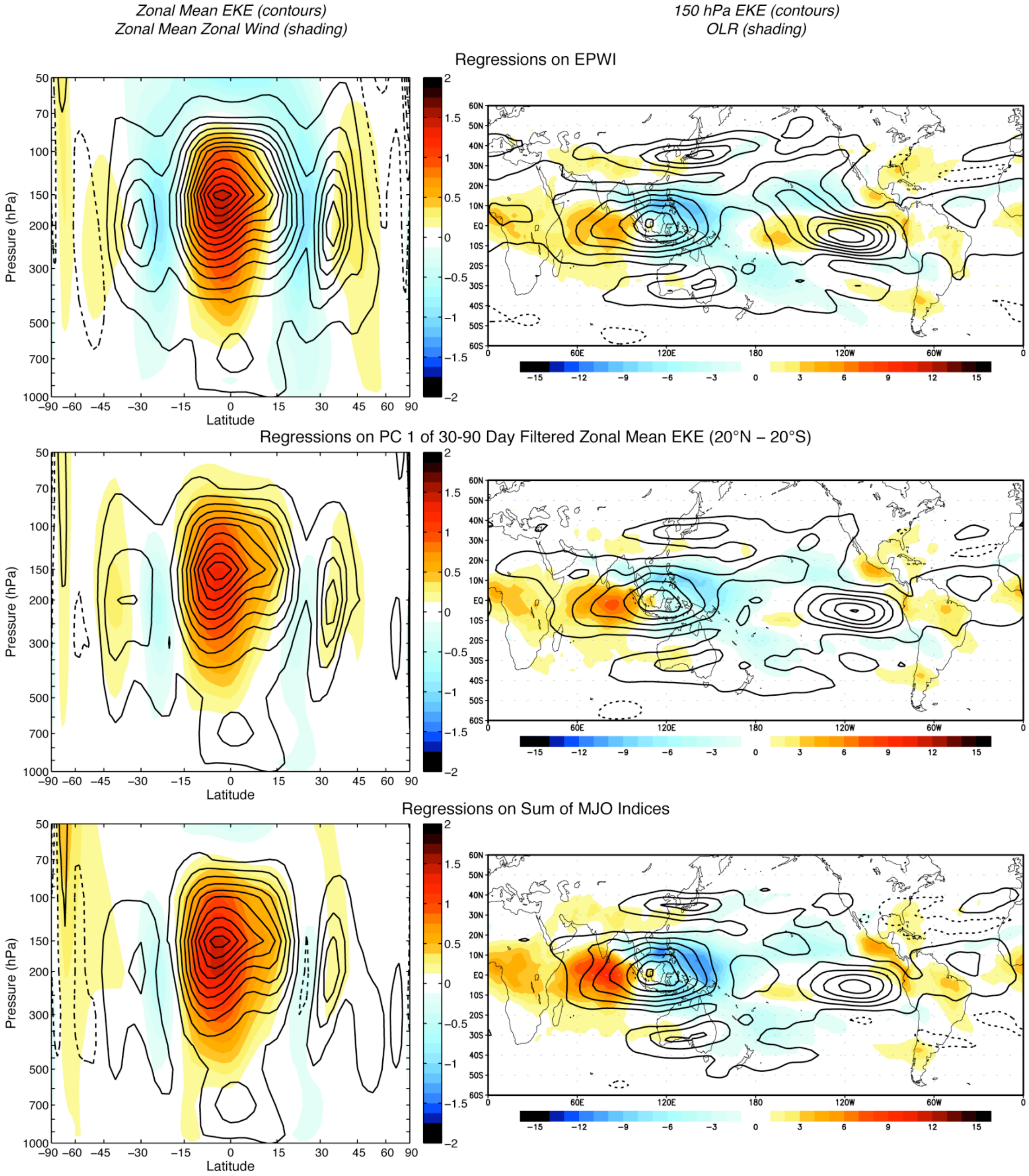

Figure 5.3: As in Figure 5.2, but for regressions on (middle row) the leading PC time series of the 30–90-day band-pass filtered daily-mean, zonal-mean eddy kinetic energy anomalies for the region 20ºN – 20ºS and (bottom row) the sum of the paired MJO index time series. Units are per standard deviation in each time series.

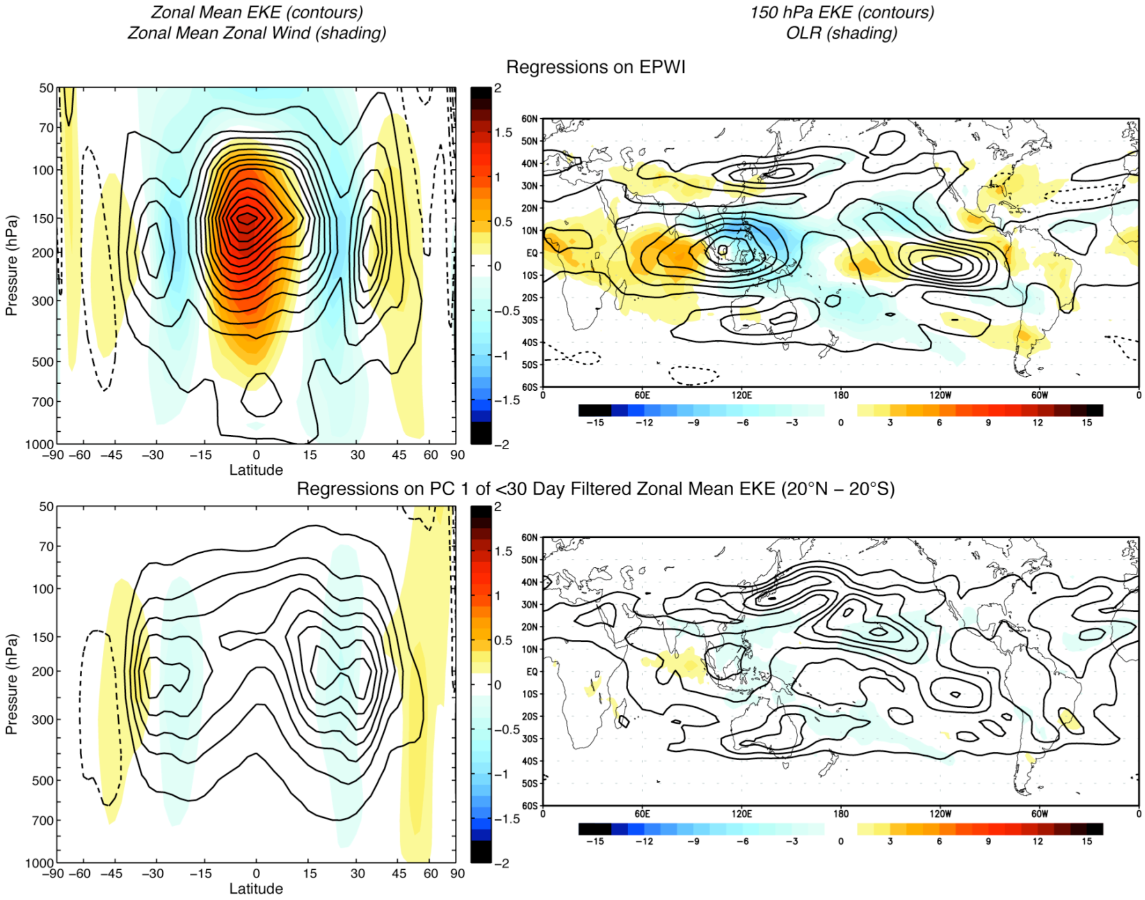

Figure 5.4: As in Figure 5.2, but for regressions on (middle row) the leading PC time series of the 30-day high-pass filtered daily-mean, zonal-mean eddy kinetic energy anomalies for the region 20ºN – 20ºS. Units are per standard deviation in each time series.

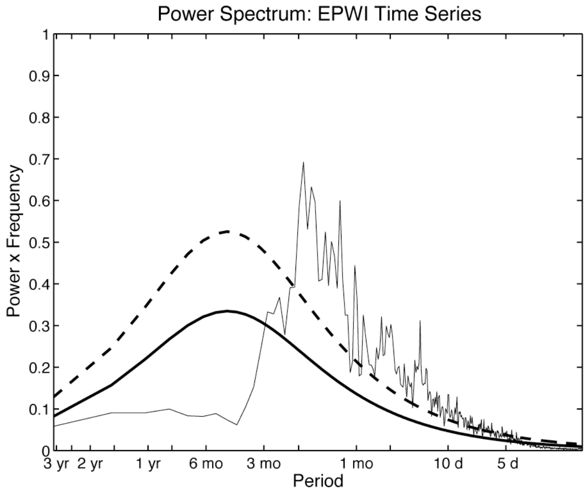

Figure 5.5: (Thin solid line) Power spectrum for the EPWI time series calculated by averaging the spectra from 19 overlapping subsets that were each weighted by a Hanning window. (Thick solid line) Theoretical red noise spectrum. (Thick dashed line) 95% statistical significance bound measured by the *F*-statistic associated with 20 degrees of freedom for the spectral estimates and infinite degrees of freedom for the red noise fit. The area under the power spectrum and red noise spectrum has been normalized to one.

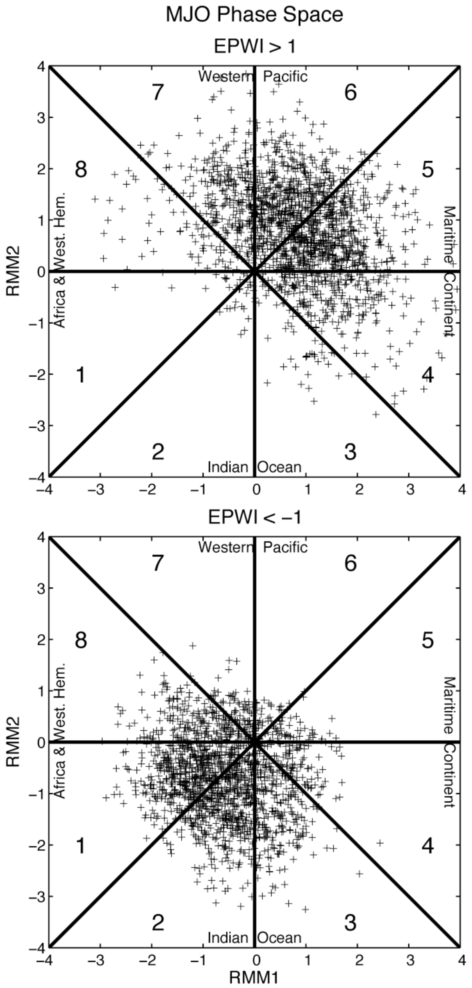

Figure 5.6: Scatter plot of the phase space spanned by the paired MJO index time series (RMM1 and RMM2) for (top) the days on which the EPWI time series is greater than +1 standard deviation and (bottom) the days on which the EPWI time series is less than -1 standard deviation. The labels indicate the numerical phases of the MJO as defined in Wheeler and Hendon (2004) and the approximate location of the enhanced convection in each of those phases.

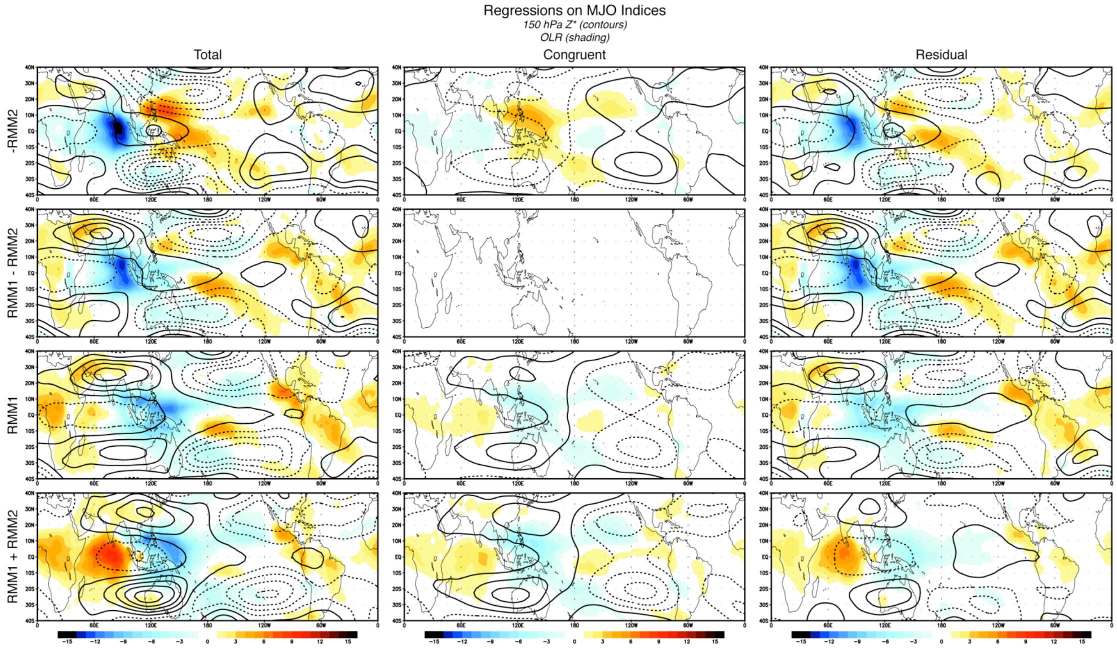

Figure 5.7: Regressions on linear combinations of the paired MJO indices (RMM1 and RMM2). The regressions are on (top row) – RMM2, (second row) RMM1 – RMM2, (third row) RMM1, and (bottom row) RMM1 + RMM2. The regressions in the middle column represent the component of the total regressions (left column) that is linearly congruent with the EPWI time series, and the regressions in the right column represent the component of the total regressions that is linearly unrelated to the EPWI time series. The black contours represent 150-hPa Z^* anomalies. Positive contours are solid, negative contours are dashed, and the contour interval is 4 m (–6, –2, 2, 6, …). The colored shading represents outgoing longwave radiation anomalies (from NOAA Interpolated OLR data set). The shading interval is 1 W m^{-2}. Units are per standard deviation in the MJO indices.

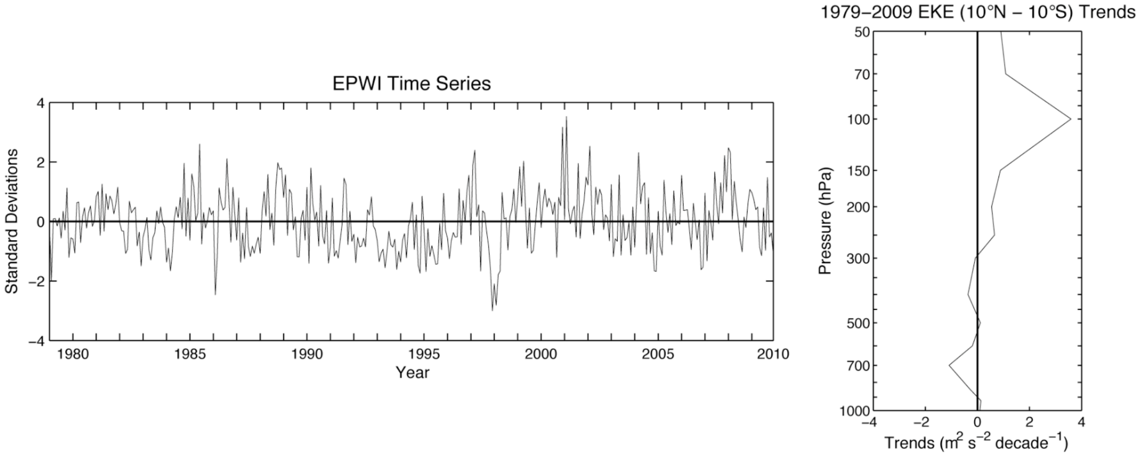

<u>Figure 5.8:</u> (Left panel) EPWI time series derived from monthly-mean data. (Right panel) 1979–2009 trends in time series of monthly-mean, zonal-mean eddy kinetic energy anomalies (averaged over 10ºN–10ºS) at each vertical level.

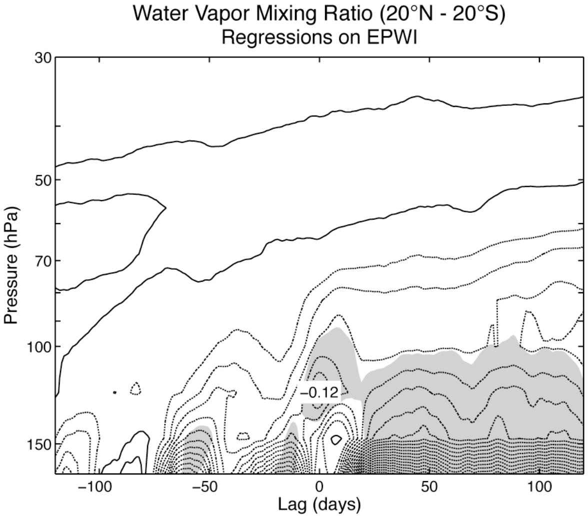

Figure 5.9: Daily-mean Aura MLS water vapor mixing ratio anomalies (averaged over 20ºN – 20ºS) regressed upon the EPWI time series. The EPWI leads (lags) the water vapor anomalies at positive (negative) lags. Positive contours are solid, negative contours are dashed, and the zero contour has been omitted. The contour interval is 0.02 ppmv. Units are per standard deviation in the EPWI time series. The shading indicates regions that are 95% significant. This figure is based upon data covering the period 2005 – 2009.

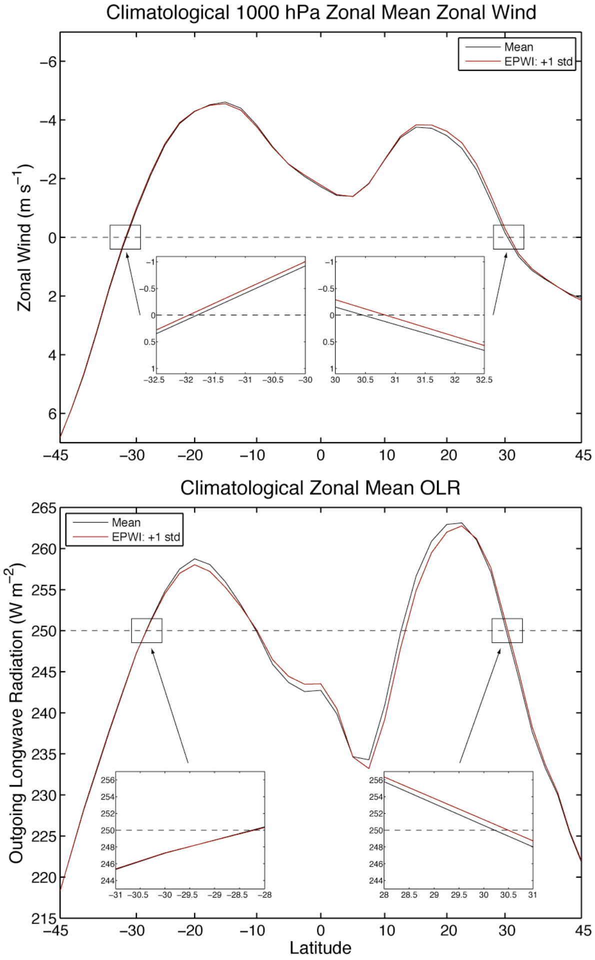

Climatological 1000 hPa Zonal Mean Zonal Wind

Climatological Zonal Mean OLR

Figure 5.10: Climatological zonal-mean (top) 1000-hPa zonal wind and (bottom) outgoing longwave radiation (from NOAA Interpolated OLR data set). The climatological-mean values (solid black line) are accompanied by the regressions of daily-mean, zonal-mean (top) 1000-hPa zonal wind anomalies and (bottom) outgoing longwave radiation anomalies on the EPWI time series. The regression coefficients have been added to the climatological-mean values at each latitude (red line). The dashed line indicates the (top) 0 m s^{-1} and (bottom) 250 W m^{-2} thresholds. Note that the ordinate is reversed in the top panel to emphasize easterly winds.

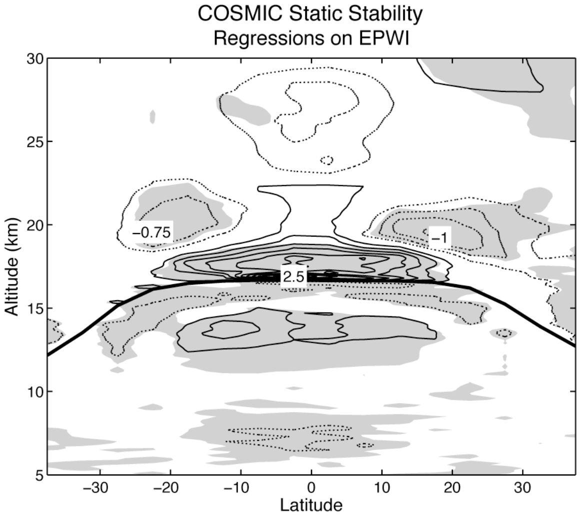

Figure 5.11: Five-day-mean, zonal-mean COSMIC static stability anomalies in tropopause-relative coordinates regressed upon the EPWI time series. Positive contours are solid, negative contours are dotted, and the zero contour has been omitted. The contour interval is 2.5 x 10^{-6} s^{-2}, and the contour labels are in units of 10^{-5} s^{-2}. Units are per standard deviation in the EPWI time series. The shading indicates regions that are 95% significant. The thick solid black line is the annual-mean, zonal-mean thermal tropopause height. The abscissa in this figure is not plotted using a sine of latitude scale so that the results are more easily compared to those in Chapter 3. This figure and all subsequent figures that use COSMIC data are based upon the period 2007 – 2010.

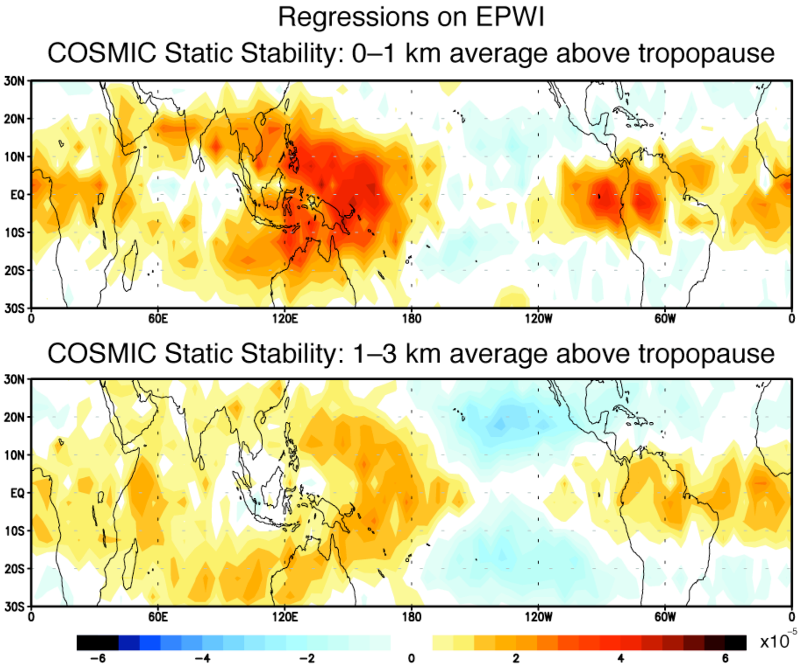

Figure 5.12: Five-day-mean COSMIC static stability anomalies regressed upon the EPWI time series. The top panel is for static stability averaged over the 0–1-km layer above the tropopause, and the bottom panel is for static stability averaged over the 1–3-km layer above the tropopause. The shading interval is 4.0 x 10^{-6} s^{-2}. Units are per standard deviation in the EPWI time series.

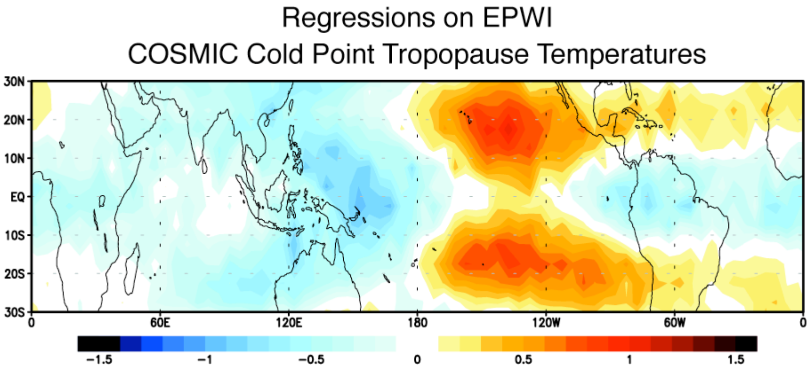

Figure 5.13: Five-day-mean COSMIC cold point tropopause temperature anomalies regressed upon the EPWI time series. The shading interval is 0.1 K. Units are per standard deviation in the EPWI time series.

CHAPTER 6: CONCLUSIONS

6.1 Summary and Discussion

The tropopause is an important interface in the climate system, separating the unique dynamical, chemical, and radiative regimes of the troposphere and stratosphere. In recent years, it has become apparent that the tropopause can also be viewed as a layer consisting of both stratospheric and tropospheric properties. In the extratropics, the layer is categorized as a mixing zone (the extratropical tropopause transition layer or ExTL) or as a sharp temperature inversion in the lowermost stratosphere (the tropopause inversion layer or TIL). In the tropics, the layer is categorized as a transition zone between the top of convection and the cold point tropopause (the tropical tropopause layer or TTL).

In this dissertation, the global tropopause is re-examined using high vertical resolution GPS radio occultation temperature profiles. The GPS data are used to conduct a comprehensive global survey of the vertical temperature stratification, or static stability, near the global tropopause. Consistent with previous studies (e.g., Birner 2006; Randel et al. 2007a; Randel and Wu 2010), the analyses reveal a fine-scale temperature inversion in the extratropical lowermost stratosphere (i.e., the TIL), which is strongest in polar regions during summer (Figures 3.1 and 3.4). However, the results of this dissertation also demonstrate that the polar TIL is strongly modulated by wave-driven variability in the stratospheric polar vortex. Periods after sudden stratospheric warmings are marked by a substantial enhancement in the strength of the polar TIL (Figures 3.13 and 3.14). The strong TIL may act to 1) inhibit the propagation of gravity and Rossby wave activity into the stratosphere (see discussion in Birner 2006) and/or 2) affect the propagation of baroclinic eddies in the extratropical upper troposphere (Simpson et al. 2009). Thus, the TIL may play a role in the coupling of the extratropical tropospheric and stratospheric flow observed after sudden stratospheric warmings (e.g., Baldwin and Dunkerton 2001).

In the tropics, the static stability field exhibits unique horizontally and vertically varying structures in the narrow layer above the tropopause. The structures, which are referred to as the tropical TIL, have not been appreciated in previous studies. The tropical TIL is characterized by two key features: 1) a very shallow static stability maximum centered at the Equator and located ~0–1 km above the tropopause and 2) paired static stability maxima in the lower stratosphere centered between 10° and 20° latitude in both hemispheres and located ~1–3 km above the tropopause (Figure 3.2). The features of the tropical TIL may play a key role in the propagation of tropical waves and the exchange of air across the tropical tropopause.

Both features of the tropical TIL have physically meaningful horizontal structures (Figure 3.10). The lower feature bears resemblance to the pattern of cold point temperatures in the tropics (e.g., Highwood and Hoskins 1998; Figure 3.11, left) and to the spatial distribution of cirrus clouds in the TTL (cf. Figure 4 of Virts and Wallace 2010), and both the upper and lower features are consistent with the quasi-stationary equatorial Rossby and Kelvin wave responses to the diabatic heating associated with the climatological distribution of deep convection (e.g., Gill 1980; Highwood and Hoskins 1998; see also Appendix B). The upper feature is also strongly modulated by the stratospheric dynamics of the quasi-biennial oscillation (QBO; Figure 3.15). Thus, the results suggest that tropospheric dynamics associated with equatorial planetary waves, stratospheric dynamics associated with the QBO, and localized radiative processes associated with deep convection and cirrus clouds may each play some role in forcing the static stability structures in the tropical TIL.

To better understand the role of equatorial planetary waves in the tropical TIL, the second half of the dissertation focuses on the role of equatorial planetary waves in atmospheric variability. The analyses examine NCEP-NCAR reanalysis data to develop an index for the temporal variability of the equatorial planetary waves. Previous studies have primarily isolated the signatures of the equatorial planetary waves in the long-term mean and seasonal cycle of the general circulation (e.g., Dima et al. 2005; Dima and Wallace 2007). In contrast, this dissertation shows that the equatorial planetary waves not only dominate structures in the climatological-mean tropical circulation, but they also play an important role in its interannual and intraseasonal variability.

The structure of the climatological-mean pattern of equatorial planetary waves emerges as the leading pattern of wavelike variability in the tropical circulation (Figures 4.2 and 4.3). The variability is characterized by the leading principal component time series of zonal-mean eddy kinetic energy in the tropics (i.e., the EPWI time series). Similar structures can also be derived from 1) the projection of the wave component of the flow onto the seasonally-varying climatological mean structure of the equatorial planetary waves (Figures 4.2 and 4.3, middle row) and 2) empirical orthogonal function analysis of a range of key tropical dynamical fields (Figure 4.4).

Variability in the equatorial planetary waves (as measured by the EPWI time series) is associated with a distinct pattern of equatorially symmetric features. In the zonal mean, periods of enhanced amplitude in the equatorial planetary waves (i.e., the positive polarity of the EPWI time series) are characterized by: 1) meridional eddy momentum flux anomalies that converge in the tropical upper troposphere, 2) westerly wind anomalies in the tropical upper troposphere, 3) negative temperature anomalies at the tropical tropopause, 4) deep easterly wind anomalies in the subtropics, and 5) positive temperature anomalies in the subtropical troposphere (Figure 4.6). The structures bear resemblance to those associated with the simulated equatorial planetary wave response to zonally asymmetric tropical heating (e.g., Kraucunas and Hartmann 2005; Norton 2006) and are consistent with anomalous meridional circulation cells being forced by the eddy momentum flux anomalies (Figure 4.9).

The EPWI time series can be used to isolate the structures in the tropical TIL associated with variability in the equatorial planetary waves. Periods of enhanced amplitude in the equatorial planetary waves are associated with positive static stability anomalies in the layer ~0–1 km above the tropical tropopause and negative off-equatorial static stability anomalies in the layer ~1–3 km above the tropical tropopause (Figure 5.11). The positive static stability anomalies in the ~0–1 km layer are co-located with negative cold point tropopause temperature anomalies (Figure 5.13), and the negative zonal-mean static stability anomalies in the ~1–3 km layer arise largely from anomalous upper tropospheric cyclones over the eastern Pacific Ocean (Figure 5.12, bottom). The results support the role of equatorial planetary waves in governing the static stability features of the tropical TIL. But other processes, such as stratospheric dynamics or localized radiative cooling, cannot be excluded and may play equally important roles.

The EPWI time series can also be used to interpret a range of other phenomena in the tropical climate system. Regressions of outgoing longwave radiation and sea surface temperature anomalies on the EPWI time series (Figure 5.1) reveal patterns reminiscent of both the El Niño-Southern Oscillation (ENSO) and the Madden-Julian Oscillation (MJO), and analyses performed using low-pass filtered and band-pass filtered data yield very similar structures to those associated with ENSO and the MJO (Figures 5.2 and 5.3). Thus, the structures associated with the EPWI time series arise from both interannual and intraseasonal timescales and are strongly related to both ENSO and the MJO.

The relationship between variability in the equatorial planetary waves and the MJO is particularly intriguing. It is suggested that the MJO can be decomposed into a pulsating and a propagating component and that the pulsating component (i.e., the pulsation of the equatorial planetary waves) aliases the true nature of the MJO's propagation (Figure 5.7). Past studies have shown that the MJO is neither a pure Kelvin wave nor a standing oscillation in convection (e.g., Hsu 1996; Zhang and Hendon 1997). However, the results shown here suggest that the role of equatorial planetary waves in the MJO signal warrants further exploration.

Variability in the equatorial planetary waves may also be relevant in interpreting decadal variability in the tropics. The EPWI time series exhibited an increase in values in ~2000 (Figure 5.8), which coincided with a decrease in stratospheric water vapor (e.g., Randel et al. 2006) and an increase in the width of the tropical belt (cf. Figure 1 of Johanson and Fu 2009). Consequently, because the EPWI time series is associated with temperature anomalies near the tropical tropopause (Figure 4.6), variability in the equatorial planetary waves may have impacted stratospheric water vapor concentrations and their recent trends. However, no definitive link between equatorial planetary waves and stratospheric water vapor was found in the five years of data used in this study (Figure 5.9). Future analyses should re-examine the relationship between equatorial planetary waves and stratospheric water vapor in longer data records.

Variability in the equatorial planetary waves is linked to variability in the width of the tropics (Figure 5.10), as the positive polarity of the EPWI time series is associated with anomalous easterly winds, subsidence, and adiabatic warming in the subtropics (Figures 4.6 and 4.10). However, the EPWI time series exhibits only a weak trend over the last ~30 years (Figure 5.8) and does not appear to be linked to the recent trend in the width of the tropics. Nevertheless, because the EPWI time series is derived from reanalysis data, future work should re-examine the relationship between the equatorial planetary waves and the width of the tropics using additional data sets.

Overall, the results of this dissertation can be summarized in two overarching conclusions:

1. *Fine-scale static stability structures near the global tropopause (i.e., the TIL) are attributable to a diverse range of radiative and dynamical processes.* Previous studies have argued for the role of radiative processes associated with ozone and water vapor (e.g., Randel et al. 2007a; Kunz et al. 2009) and dynamical processes associated with tropospheric anticyclones (e.g., Wirth 2003; Wirth and Szabo 2007). Here, the results suggest the role of equatorial planetary waves, the QBO, and wave-driven variability in the stratospheric polar vortex. The results also hint at the

importance of the radiative processes associated with the clouds and chemical constituents in the TTL.

2. *The pulsation of the quasi-stationary equatorial planetary waves in the tropics is a fundamental feature of the tropical climate system.* It emerges in conjunction with a wide range of tropical climate phenomena and thus provides a framework for linking a host of otherwise seemingly unrelated climate features (the tropical TIL, ENSO, MJO, stratospheric water vapor, the width of the tropics, etc.).

6.2 Future Work

The results of this dissertation raise a number of questions to consider in future work. In this section, three potential avenues for future research are discussed.

6.2.1 The role of the TIL in stratosphere–troposphere coupling

The results of this dissertation demonstrate a linkage between wave-driven variability in the stratospheric polar vortex and the strength of the TIL in polar regions (Figures 3.13 and 3.14). Interestingly, periods following fluctuations in the strength of the polar vortex are associated not only with fluctuations in the strength of the polar TIL but also with fluctuations in the extratropical tropospheric flow (e.g., Baldwin and Dunkerton 2001). Whether the linkages between the TIL and the extratropical tropospheric flow are causal or merely coincidental remains unclear.

Theoretical studies that have examined the effects of fine-scale features in the atmospheric static stability field have been inconclusive. For example, Lindzen (1994) demonstrated that fine-scale vertical gradients in a quasi-geostrophic reference state could have a profound effect on stationary Rossby waves, but his results were later found to be attributable to a numerical error (Lindzen and Roe 1997). However, Simpson et al. (2009) have recently showed the importance of the vertical distribution of static stability near the tropopause in determining upper tropospheric eddy momentum flux anomalies and the eddy-driven tropospheric circulation response to stratospheric heating perturbations in an idealized general circulation model.

Future work on this topic should focus on two fronts. First, more in-depth observational analyses should be conducted to examine whether fluctuations in the stratospheric polar vortex that manifest themselves at tropospheric levels are characterized by unusually strong projections onto the TIL region. Second, idealized modeling experiments should be conducted to artificially impose the presence of a TIL, similar to that which occurs after a sudden stratospheric warming. It would interesting to see whether the artificial insertion of a TIL into a numerical model could produce changes in the tropospheric circulation similar to those observed after sudden stratospheric warmings.

6.2.2 Multi-platform analysis of the tropical TIL

The results of this dissertation have extensively documented the structure of the tropical TIL using GPS radio occultation temperature profiles and examined its linkages to various dynamical forcings, particularly equatorial planetary waves. Yet, the role of radiative processes in the tropical TIL has remained largely unexplored. As in the extratropics (e.g., Randel et al. 2007a; Kunz et al. 2009), the radiative effects of ozone and water vapor may play a key role in forcing static stability anomalies in the tropical TIL. Additionally, the similarity between the spatial distribution of the lower feature of the tropical TIL (Figure 3.10, left column) and the spatial distribution of TTL cirrus (cf. Figure 4 of Virts and Wallace 2010) suggests that cloud radiative effects may also play a key role in the tropical TIL.

Thus, future work on this topic should focus on examining the tropical TIL using a multi-platform approach: Aura MLS water vapor and ozone measurements, COSMIC GPS radio occultation temperature profiles, and Cloud–Aerosol Lidar and Infrared Pathfinder Satellite Observations (CALIPSO) cirrus cloud measurements (Winker et al. 2007). The analyses should focus on transient variability in each of the fields and the linkages between the various fields and the tropical TIL. While such analyses cannot strictly separate radiative and dynamical processes, they can provide more insight into the possible role of radiative processes in the tropical TIL.

Additionally, the above analyses can be used to examine transient variability in the upwelling of constituents across the tropical tropopause. As in Randel et al. (2008), tropical upwelling can be derived from the momentum balance in reanalysis fields and then decomposed into the components associated with various contributions to the wave driving (Eliassen-Palm flux divergence). Using this method, the role of equatorial planetary waves in tropical troposphere/stratosphere exchange may be more conclusive than the results shown in Figure 5.9.

6.2.3 Idealized sea surface temperature experiments

The results of this dissertation link variability in equatorial planetary waves with variability in the width of the tropics (Figure 5.10). However, because the relationship does not appear to hold on decadal timescales, model experiments should be performed to clarify the exact role of equatorial planetary waves in the width of the tropics. A straightforward way to do this would be to construct a series of idealized aquaplanet general circulation model experiments (e.g., Frierson et al. 2007), with the tropical sea surface temperature distribution serving as the independent variable. Presumably, enhancing the sea surface temperatures in a certain region would strengthen localized deep convection in that region, affect the amplitudes of the equatorial planetary waves, and thus impact the width of the tropics. Previous studies have indeed suggested that zonally asymmetric sea surface temperature changes, particularly over the western tropical Pacific Ocean, could have an impact on the width of the tropics (Fu et al. 2006; Lau et al. 2008).

In the proposed work, the model experiments should examine cases forced with zonally symmetric tropical sea surface temperatures and compare them to cases forced with tropical sea surface temperatures characteristic of the climatology, El Niño conditions, La Niña conditions, and future climate scenarios. Given the possible importance of sea surface temperature anomalies over the western tropical Pacific Ocean, the experiments could be repeated with the tropical sea surface temperature anomalies implemented separately over the western tropical Pacific Ocean and then over all other longitudes. If the sea surface temperatures over the western tropical Pacific Ocean have a much greater impact on the width of the tropics than those at other longitudes, the model experiments would support the role of equatorial planetary waves in modulating the width of the tropics (Figure 5.10).

REFERENCES

Andrews, D. G., J. R. Holton, and C. B. Leovy, 1987: *Middle Atmospheric Dynamics*. Academic Press, 489 pp.

Anthes, R. A., and Coauthors, 2008: The COSMIC/FORMOSAT-3 mission: Early results. *Bull. Amer. Meteor. Soc.*, **89**, 313–333.

Baldwin, M. P., and T. J. Dunkerton, 2001: Stratospheric harbingers of anomalous weather regimes. *Science*, **294**, 581–584.

Baldwin, M. P., and Coauthors, 2001: The quasi-biennial oscillation. *Rev. Geophys.*, **39**, 179–229.

Bell, S. W., and M. A. Geller, 2008: Tropopause inversion layer: Seasonal and latitudinal variations and representation in standard radiosonde data and global models. *J. Geophys. Res.*, **113**, doi:10.1029/2007JD009022.

Bethan, S., G. Vaughan, and S. J. Reid, 1996: A comparison of ozone and thermal tropopause heights and the impact of tropopause definition on quantifying the ozone content of the troposphere. *Quart. J. Roy. Meteor. Soc.,* **122**, 929–944.

Birner, T., 2006: Fine-scale structure of the extratropical tropopause region. *J. Geophys. Res.*, **111**, doi:10.1029/2005JD006301.

Birner, T., 2010: Residual circulation and tropopause structure. *J. Atmos. Sci.*, **67**, 2582 –2600.

Birner, T., A. Dörnbrack, and U. Schumann, 2002: How sharp is the tropopause at midlatitudes? *Geophys. Res. Lett.*, **29**, doi:10.1029/2002GL015142.

Birner, T., D. Sankey, and T. G. Shepherd, 2006: The tropopause inversion layer in models and analyses. *Geophys. Res. Lett.*, **33**, doi:10.1029/2006GL026549.

Boehm, M. T., and S. Lee, 2003: The implications of tropical Rossby waves for tropical tropopause cirrus formation and for the equatorial upwelling of the Brewer-Dobson Circulation. *J. Atmos. Sci.*, **60**, 247–261.

Bretherton, C. S., M. Widmann, V. P. Dymnikov, J. M. Wallace, and I. Bladé, 1999: The effective number of spatial degrees of freedom of a time-varying field. *J. Climate*, **12**, 1990–2009.

Brewer, A. W., 1949: Evidence for a world circulation provided by the measurements of helium and water vapour distribution in the stratosphere. *Quart. J. Roy. Meteor. Soc.*, **75**, 351–363.

Calvo, N., and R. R. Garcia, 2009: Wave forcing of the tropical upwelling in the lower stratosphere under increasing concentrations of greenhouse gases. *J. Atmos. Sci.*, **66**, 3184–3196.

Charney, J.G., and P.G. Drazin, 1961: Propagation of planetary-scale disturbances from the lower into the upper atmosphere. *J. Geophys. Res.,* **66**, 83-109.

Corti, T., and Coauthors, 2008: Unprecedented evidence for deep convection hydrating the tropical stratosphere. *Geophys. Res. Lett.*, **35**, L10810, doi:10.1029/2008GL033641.

Danielsen, E. F., 1982: A dehydration mechanism for the stratosphere. *Geophys. Res. Lett.*, **9**, 605–608.

Deckert, R., and M. Dameris, 2008: Higher tropical SSTs strengthen the tropical upwelling via deep convection. *Geophys. Res. Lett.*, **35**, L10813, doi:10.1029/2008GL033719.

Dhomse, S., M. Weber, and J. Burrows, 2008: The relationship between tropospheric wave forcing and tropical lower stratospheric water vapor. *Atmos. Chem. Phys.*, **8**, 471–480.

Dima, I. M., and J. M. Wallace, 2007: Structure of the annual-mean equatorial planetary waves in the ERA-40 reanalyses. *J. Atmos. Sci.*, **64**, 2862–2880.

Dima, I. M., J. M. Wallace, and I. Kraucunas, 2005: Tropical zonal momentum balance in the NCEP reanalyses. *J. Atmos. Sci.*, **62**, 2499–2513.

Dobson, G. M. B., 1956: Origin and distribution of polyatomic molecules in the atmosphere. *Proc. Roy. Soc. London*, **236A**, 187–193.

Dunkerton, T. J., 1995: Evidence of meridional motion in the summer lower stratosphere adjacent to monsoon regions. *J. Geophys. Res.*, **100**, 16 675–16 688.

Edmon, H. J., B. J. Hoskins, and M. E. McIntyre, 1980: Eliassen-Palm cross sections for troposphere. *J. Atmos. Sci.*, **37**, 2600–2616.

Egger, J., 1995: Tropopause height in baroclinic channel flow. *J. Atmos. Sci.*, **52**, 2232–2241.

Folkins, I., P. Bernath, C. Boone, G. Lesins, N. Livesey, A. M. Thompson, K. Walker, and J. C. Witte, 2006: Seasonal cycles of O_3, CO, and convective outflow at the tropical tropopause. *Geophys. Res. Lett.*, **33**, L16802, doi:10.1029/2006GL026602.

Forster, P. M. de F., and K. P. Shine, 1997: Radiative forcing and temperature trends from stratospheric ozone changes. *J. Geophys. Res.*, **102**, 10 841–10 855.

Forster, P. M. de F., and K. P. Shine, 1999: Stratospheric water vapour changes as a possible contributor to observed stratospheric cooling. *Geophys. Res. Lett.*, **26**, 3309–3312.

Frierson, D. M. W., 2008: Midlatitude static stability in simple and comprehensive general circulation models. *J. Atmos. Sci.*, **65**, 1049–1062.

Frierson, D. M. W., I. M. Held, and P. Zurita-Gotor, 2006: A gray-radiation aquaplanet moist GCM. Part I: Static stability and eddy scale. *J. Atmos. Sci.*, **63**, 2548–2566.

Frierson, D. M. W., J. Lu, and G. Chen, 2007: Width of the Hadley cell in simple and comprehensive general circulation models. *Geophys. Res. Lett.*, **34**, L18804, doi:10.1029/2007GL031115.

Fu, Q., C. M. Johanson, J. M. Wallace, and T. Reichler, 2006: Enhanced mid-latitude tropospheric warming in satellite measurements. *Science*, **312**, 1179.

Fueglistaler, S., and P. H. Haynes, 2005: Control of interannual and longer-term variability of stratospheric water vapor. *J. Geophys. Res.*, **110**, D24108, doi:10.1029/2005JD006019.

Fueglistaler, S., M. Bonazzola, P. H. Haynes, and T. Peter, 2005: Stratospheric water vapor predicted from the Lagrangian temperature history of air entering the stratosphere in the tropics. *J. Geophys. Res.*, **110**, D08107, doi:10.1029/2004JD005516.

Fueglistaler, S., A. E. Dessler, T. J. Dunkerton, I. Folkins, Q. Fu, and P. W. Mote, 2009: Tropical tropopause layer. *Rev. Geophys.*, **47**, RG1004, doi:10.1029/2008RG000267.

Fujiwara, M., and Coauthors, 2010: Seasonal to decadal variations of water vapor in the tropical lower stratosphere observed with balloon-borne cryogenic frost point hygrometers. *J. Geophys. Res.*, **115**, D18304, doi:10.1029/2010JD014179.

Geller, M. A., X. Zhou, and M. Zhang, 2002: Simulations of the interannual variability of stratospheric water vapor. *J. Atmos. Sci.*, **59**, 1076–1085.

Gettelman, A., and P. M. Forster, 2002: A climatology of the tropical tropopause layer. *J. Meteor. Soc. Japan*, **80**, 911–924.

Gettelman, A., and T. Birner, 2007: Insights into tropical tropopause layer processes using global models. *J. Geophys. Res.*, **112**, D23104, doi:10.1029/2007JD008945.

Gill, A. E., 1980: Some simple solutions for heat-induced tropical circulation. *Quart. J. Roy. Meteor. Soc.*, **106**, 447–462.

Grise, K. M., D. W. J. Thompson, and P. M. Forster, 2009: On the role of radiative processes in stratosphere-troposphere coupling. *J. Climate*, **22**, 4154–4161.

Hajj, G. A., and Coauthors, 2004: CHAMP and SAC-C atmospheric occultation results and intercomparisons. *J. Geophys. Res.*, **109**, doi:10.1029/2003JD003909.

Hartmann, D. L., 1976: The structure of the stratosphere in the Southern Hemisphere during late winter 1973 as observed by satellite. *J. Atmos. Sci.*, **33**, 1141–1154.

Hartmann, D. L., J. R. Holton, and Q. Fu, 2001: The heat balance of the tropical tropopause, cirrus, and stratospheric dehydration. *Geophys. Res. Lett.*, **28**, 1969–1972.

Haynes, P., 2005: Stratospheric dynamics. *Annu. Rev. Fluid Mech.*, **37**, 263-293.

Haynes, P.H., C.J. Marks, M.E. McIntyre, T.G. Shepherd, and K.P. Shine, 1991: On the "downward control" of extratropical diabatic circulations by eddy-induced mean zonal forces. *J. Atmos. Sci.*, **48**, 651-678.

Haynes, P., J. Scinocca, and M. Greenslade, 2001: Formation and maintenance of the extratropical tropopause by baroclinic eddies. *Geophys. Res. Lett.*, **28**, 4179–4182.

Hegglin, M. I., C. D. Boone, G. L. Manney, and K. A. Walker, 2009: A global view of the extratropical tropopause transition layer from Atmospheric Chemistry Experiment Fourier Transform Spectrometer O_3, H_2O, and CO. *J. Geophys. Res.*, **114**, D00B11, doi:10.1029/2008JD009984.

Held, I. M., 1982: On the height of the tropopause and the static stability of the troposphere. *J. Atmos. Sci.*, **39**, 412–417.

Hendon, H. H., and B. Liebmann, 1990a: The intraseasonal (30-50 day) oscillation of the Australian summer monsoon. *J. Atmos. Sci.*, **47**, 2909–2923.

Hendon, H. H., and B. Liebmann, 1990b: A composite study of onset of the Australian summer monsoon. *J. Atmos. Sci.*, **47**, 2227–2240.

Hendon, H. H., and M. L. Salby, 1994: The life cycle of the Madden-Julian Oscillation. *J. Atmos. Sci.*, **51**, 2225 – 2237.

Highwood, E. J., and B. J. Hoskins, 1998: The tropical tropopause. *Quart. J. Roy. Meteor. Soc.*, **124**, 1579–1604.

Hoerling, M. P., A. Kumar, and T. Xu, 2001: Robustness of the nonlinear climate response to ENSO's extreme phases. *J. Climate*, **14**, 1277–1293.

Hoinka, K. P., 1997: The tropopause: discovery, definition, and demarcation. *Meteor. Z.*, **6**, 281–303.

Holloway, C. E., and J. D. Neelin, 2007: The convective cold top and quasi equilibrium. *J. Atmos. Sci.*, **64**, 1467–1487.

Holton, J. R., 2004: *An Introduction to Dynamic Meteorology, 4th ed.* Elsevier Academic Press, 535 pp.

Holton, J. R., and A. Gettelman, 2001: Horizontal transport and the dehydration of the stratosphere. *Geophys. Res. Lett.*, **28**, 2799–2802.

Holton, J. R., P. H. Haynes, M. E. McIntyre, A. R. Douglass, R. B. Rood, and L. Pfister, 1995: Stratosphere-troposphere exchange. *Rev. Geophys.*, **33**, 403–439.

Hsu, H.-H., 1996: Global view of the intraseasonal oscillation during northern winter. *J. Climate*, **9**, 2386–2406.

Hu, Y., and Q. Fu, 2007: Observed poleward expansion of the Hadley circulation since 1979. *Atmos. Chem. Phys.*, **7**, 5229–5236.

Hudson, R. D., M. F. Andrade, M. B. Follette, and A. D. Frolov, 2006: The total ozone field separated into meteorological regimes – Part II: Northern Hemisphere mid-latitude total ozone trends. *Atmos. Chem. Phys.*, **6**, 5183–5191.

Jacob, D.J., 1999: *Introduction to Atmospheric Chemistry*. Princeton University Press, 266 pp.

Jensen, E. J., O. B. Toon, H. B. Selkirk, J. D. Spinhirne, and M. R. Schoeberl, 1996: On the formation and persistence of subvisible cirrus clouds near the tropical tropopause. *J. Geophys. Res.,* **101**, 21 361–21 375.

Johanson, C. M., and Q. Fu, 2009: Hadley cell widening: Model simulations versus observations. *J. Climate*, **22**, 2713–2725.

Juckes, M. N., 2000: The static stability of the midlatitude troposphere: The relevance of moisture. *J. Atmos. Sci.*, **57**, 3050–3057.

Kalnay, E., and Coauthors, 1996: The NCEP/NCAR 40-Year Reanalysis Project. *Bull. Amer. Meteor. Soc.,* **77,** 437–471.

Kerr-Munslow, A. M., and W. A. Norton, 2006: Tropical wave driving of the annual cycle in tropical tropopause temperatures. Part I: ECMWF analyses. *J. Atmos. Sci.*, **63**, 1410–1419.

Kiehl, J. T., and S. Solomon, 1986: On the radiative balance of the stratosphere. *J. Atmos. Sci.*, **43**, 1525–1534.

Kirk-Davidoff, D. B., and R. S. Lindzen, 2000: An energy balance model based on potential vorticity homogenization. *J. Climate*, **13**, 431–448.

Kistler, R., and Coauthors, 2001: The NCEP-NCAR 50-Year Reanalysis: Monthly means CD-ROM and documentation. *Bull. Amer. Meteor. Soc.,* **82**, 247–267.

Kraucunas, I., and D. L. Hartmann, 2005: Equatorial superrotation and the factors controlling the zonal-mean zonal winds in the tropical upper troposphere. *J. Atmos. Sci.*, **62**, 371–389.

Kuang, Z., and C. S. Bretherton, 2004: Convective influence on the heat balance of the tropical tropopause layer: A cloud-resolving model study. *J. Atmos. Sci.*, **61**, 2919–2927.

Kunz, A., P. Konopka, R. Müller, L. L. Pan, C. Schiller, and F. Rohrer, 2009: High static stability in the mixing layer above the extratropical tropopause. *J. Geophys. Res.*, **114**, D16305, doi:10.1029/2009JD011840.

Kunz, A., P. Konopka, R. Müller, and L. L. Pan, 2011: Dynamical tropopause based on isentropic potential vorticity gradients. *J. Geophys. Res.*, **116**, D01110, doi:10.1029/2010JD014343.

Kursinski, E. R., and Coauthors, 1996: Initial results of radio occultation observations of earth's atmosphere using the Global Positioning System. *Science*, **271**, 1107–1110.

Lambert, A., and Coauthors, 2007: Validation of the Aura Microwave Limb Sounder middle atmosphere water vapor and nitrous oxide measurements. *J. Geophys. Res.*, **112**, D24S36, doi:10.1029/2007JD008724.

Lau, N.-C., A. Leetmaa, and M. J. Nath, 2008: Interactions between the responses of North American climate to El Niño-La Niña and to the secular warming trend in the Indian-Western Pacific Oceans. *J. Climate*, **21**, 476–494.

Lee, S., 1999: Why are the climatological zonal winds easterly in the equatorial upper troposphere? *J. Atmos. Sci.*, **56**, 1353–1363.

Le Texier, H., S. Solomon, and R. R. Garcia, 1988: The role of molecular hydrogen and methane oxidation in the water vapour budget of the stratosphere. *Q. J. R. Meteorol. Soc.*, **114**, 281–295.

Liebmann, B., and C. A. Smith, 1996: Description of a complete (interpolated) outgoing longwave radiation dataset. *Bull. Amer. Meteor. Soc.*, **77**, 1275–1277.

Lindzen, R. S., 1994: The effect of concentrated PV gradients on stationary waves. *J. Atmos. Sci.*, **51**, 3455–3466.

Lindzen, R. S., and G. Roe, 1997: The effect of concentrated PV gradients on stationary waves: Correction. *J. Atmos. Sci.*, **54**, 1815 – 1818.

Lu, J., G. Chen, and D. M. W. Frierson, 2008: Response of the zonal mean atmospheric circulation to El Niño versus global warming. *J. Climate*, **21**, 5835–5851.

Madden, R. A., 1987: Relationships between changes in the length of day and the 40- to 50-day oscillation in the tropics. *J. Geophys. Res.*, **92**, 8391–8399.

Madden, R. A., and P. R. Julian, 1994: Observations of the 40-50-day tropical oscillation-a review. *Mon. Wea. Rev.*, **122**, 814–837.

Manabe, S., and R. F. Strickler, 1964: Thermal equilibrium of the atmosphere with a convective adjustment. *J. Atmos. Sci.*, **21**, 361–385.

Massie, S., A. Gettelman, W. Randel, and D. Baumgardner, 2002: Distribution of tropical cirrus in relation to convection. *J. Geophys. Res.*, **107**, 4591, doi:10.1029/2001JD001293.

Matsuno, T., 1966: Quasi-geostrophic motions in the equatorial area. *J. Meteorol. Soc. Japan*, **44**, 25–43.

McIntyre, M.E., 1982: How well do we understand the dynamics of stratospheric warmings?. *J. Meteorol. Soc. Japan*, **60**, 37-65.

Mote, P. W., and Coauthors, 1996: An atmospheric tape recorder: The imprint of tropical tropopause temperatures on stratospheric water vapor. *J. Geophys. Res.*, **101**, 3989–4006.

Mote, P. W., T. J. Dunkerton, and H. C. Pumphrey, 1998: Sub-seasonal variations in lower stratospheric water vapor. *Geophys. Res. Lett.*, **25**, 2445–2448.

Mote, P. W., H. L. Clark, T. J. Dunkerton, R. S. Harwood, and H. C. Pumphrey, 2000: Intraseasonal variations of water vapor in the tropical upper troposphere and tropopause region. *J. Geophys. Res.*, **105**, 17 457 – 17 470.

Newell, R. E., and S. Gould-Stewart, 1981: A stratospheric fountain? *J. Atmos. Sci.*, **38**, 2789–2796.

North, G. R., T. L. Bell, R. F. Cahalan, and F. J. Moeng, 1982: Sampling errors in the estimation of empirical orthogonal functions. *Mon. Wea. Rev.,* **110,** 699–706.

Norton, W. A., 2006: Tropical wave driving of the annual cycle in tropical tropopause temperatures. Part II: Model results. *J. Atmos. Sci.*, **63**, 1420–1431.

Pan, L. L., and Coauthors, 2010: The Stratosphere-Troposphere Analyses of Region Transport 2008 experiment. *Bull. Amer. Meteor. Soc.*, **91**, 327–342.

Peixoto, J. P., and A. H. Oort, 1992: *Physics of Climate.* American Institute of Physics, 520 pp.

Plumb, R. A., 1996: A "tropical pipe" model of stratospheric transport. *J. Geophys. Res.*, **101**, 3957–3972.

Plumb, R. A., and J. Eluszkiewicz, 1999: The Brewer-Dobson circulation: Dynamics of the tropical upwelling. *J. Atmos. Sci.*, **56**, 868–890.

Randel, W. J., and F. Wu, 2005: Kelvin wave variability near the equatorial tropopause observed in GPS radio occultation measurements. *J. Geophys. Res.*, **110**, D03102, doi:10.1029/2004JD005006.

Randel, W. J., and F. Wu, 2010: The polar summer tropopause inversion layer. *J. Atmos. Sci.*, **67**, 2572–2581.

Randel, W. J., F. Wu, and D. J. Gaffen, 2000: Interannual variability of the tropical tropopause derived from radiosonde data and NCEP reanalysis. *J. Geophys. Res.*, **105**, D12, 15509–15523.

Randel, W. J., R. R. Garcia, and F. Wu, 2002: Time-dependent upwelling in the tropical lower stratosphere estimated from the zonal-mean momentum budget. *J. Atmos. Sci.*, **59**, 2141–2152.

Randel, W. J., F. Wu, and W. R. Rios, 2003: Thermal variability of the tropical tropopause region derived from GPS/MET observations. *J. Geophys. Res.*, **108**, 4024, doi:10.1029/2002JD002595.

Randel, W. J., F. Wu, S. J. Oltmans, K. Rosenlof, and G. E. Nedoluha, 2004: Interannual changes of stratospheric water vapor and correlations with tropical tropopause temperatures. *J. Atmos. Sci.*, **61**, 2133–2148.

Randel, W. J., F. Wu, H. Vömel, G. E. Nedoluha, and P. Forster, 2006: Decreases in stratospheric water vapor after 2001: Links to changes in the tropical tropopause and the Brewer-Dobson circulation. *J. Geophys. Res.*, **111**, D12312, doi:10.1029/2005JD006744.

Randel, W. J., F. Wu, and P. Forster, 2007a: The extratropical tropopause inversion layer: Global observations with GPS data, and a radiative forcing mechanism. *J. Atmos. Sci.*, **64**, 4489–4496.

Randel, W. J., M. Park, F. Wu, and N. Livesey, 2007b: A large annual cycle in ozone above the tropical tropopause linked to the Brewer-Dobson circulation. *J. Atmos. Sci.*, **64**, 4479–4488.

Randel, W. J., R. Garcia, and F. Wu, 2008: Dynamical balances and tropical stratospheric upwelling. *J. Atmos. Sci.*, **65**, 3584–3595.

Randel, W. J., R. R. Garcia, N. Calvo, and D. Marsh, 2009: ENSO influence on zonal mean temperature and ozone in the tropical lower stratosphere. *Geophys. Res. Lett.*, **36**, L15822, doi:10.1029/2009GL039343.

Rasmusson, E. M., and T. H. Carpenter, 1982: Variations in tropical sea surface temperature and surface wind fields associated with the Southern Oscillation/El Niño. *Mon. Wea. Rev.*, **110**, 354–384.

Ratnam, M. V., T. Tsuda, T. Kozu, and S. Mori, 2006: Long-term behavior of the Kelvin waves revealed by CHAMP/GPS RO measurements and their effects on the tropopause structure. *Ann. Geophys.,* **24,** 1355–1366.

Read, W. G., and Coauthors, 2007: Aura Microwave Limb Sounder upper tropospheric and lower stratospheric H_2O and relative humidity with respect to ice validation. *J. Geophys. Res.*, **112**, D24S35, doi:10.1029/2007JD008752.

Reed, R. J., and C. L. Vlcek, 1969: The annual temperature variation in the lower tropical stratosphere. *J. Atmos. Sci.*, **26**, 163–167.

Reid, G. C., and K. S. Gage, 1981: On the annual variation in height of the tropical tropopause. *J. Atmos. Sci.*, **38**, 1928–1938.

Reynolds, R.W., N. A. Rayner, T. M. Smith, D. C. Stokes, and W. Wang, 2002: An improved in situ and satellite SST analysis for climate. *J. Climate*, **15**, 1609–1625.

Rosenlof, K. H., 1995: Seasonal cycle of the residual mean meridional circulation in the stratosphere. *J. Geophys. Res.*, **100**, 5173–5191.

Rosenlof, K. H., and G. C. Reid, 2008: Trends in the temperature and water vapor content of the tropical lower stratosphere: Sea surface connection. *J. Geophys. Res.*, **113**, D06107, doi:10.1029/2007JD009109.

Rosenlof, K. H., and Coauthors, 2001: Stratospheric water vapor increases over the past half-century. *Geophys. Res. Lett.*, **28**, 1195–1198.

Ryu, J.-H., and S. Lee, 2010: Effect of tropical waves on the tropical tropopause transition layer upwelling. *J. Atmos. Sci.*, **67**, 3130–3148.

Ryu, J.-H., S. Lee, and S.-W. Son, 2008: Vertically propagating Kelvin waves and tropical tropopause variability. *J. Atmos. Sci.*, **65**, 1817–1837.

Santer, B. D., and Coauthors, 2003: Behavior of tropopause height and atmospheric temperature in models, reanalyses, and observations: Decadal changes. *J. Geophys. Res.*, **108**, 4002, doi:10.1029/2002JD002258.

Schmidt, T., J.-P. Cammas, H. G. J. Smit, S. Heise, J. Wickert, and A. Haser, 2010: Observational characteristics of the tropopause inversion layer derived from CHAMP/GRACE radio occultations and MOZAIC aircraft data. *J. Geophys. Res.*, **115**, D24304, doi:10.1029/2010JD014284.

Schneider, T., 2004: The tropopause and the thermal stratification in the extratropics of a dry atmosphere. *J. Atmos. Sci.*, **61**, 1317–1340.

Schneider, T., 2007: The thermal stratification of the extratropical troposphere. *The Global Circulation of the Atmosphere*, T. Schneider and A. H. Sobel, Eds., Princeton University Press, 47–77.

Seager, R., N. Harnik, Y. Kushnir, W. Robinson, and J. Miller, 2003: Mechanisms of hemispherically symmetric climate variability. *J. Climate*, **16**, 2960–2978.

Seidel, D. J., and W. J. Randel, 2007: Recent widening of the tropical belt: Evidence from tropopause observations. *J. Geophys. Res.*, **112**, D20113, doi:10.1029/2007JD008861.

Seidel, D. J., Q. Fu, W. J. Randel, and T. J. Reichler, 2008: Widening of the tropical belt in a changing climate. *Nat. Geosci.*, **1**, 21–24.

Shepherd, T., R. A. Plumb, and S. C. Wofsy, 2005: PREFACE, **62**, 565–566.

Sherwood, S. C., and A. E. Dessler, 2000: On the control of stratospheric humidity. *Geophys. Res. Lett.*, **27**, 2513–2516.

Simmons, A. J., and B. J. Hoskins, 1978: The life cycles of some nonlinear baroclinic waves. *J. Atmos. Sci.*, **35**, 414–432.

Simmons, A., S. Uppala, D. Dee, and S. Kobayashi, 2007: ERA-Interim: New ECMWF reanalysis products from 1989 onwards. *ECMWF Newsletter,* **110,** Winter 2006/07, 25-35 pp.

Simpson, I. R., M. Blackburn, and J. D. Haigh, 2009: The role of eddies in driving the tropospheric response to stratospheric heating perturbations. *J. Atmos. Sci.*, **66**, 1347–1365.

Smith, C. A., J. D. Haigh, and R. Toumi, 2001: Radiative forcing due to trends in stratospheric water vapour. *Geophys. Res. Lett.*, **28**, 179–182.

Solomon, S., R. R. Garcia, F. S. Rowland, and D. J. Wuebbles, 1986: On the depletion of Antarctic ozone. *Nature*, **321**, 755–758.

Solomon, S., K. H. Rosenlof, R. W. Portmann, J. S. Daniel, S. M. Davis, T. J. Sanford, and G.-K. Plattner, 2010: Contributions of stratospheric water vapor to decadal changes in the rate of global warming. *Science*, **327**, 1219–1223.

Son, S.-W., and S. Lee, 2007: Intraseasonal variability of the zonal-mean tropical tropopause height. *J. Atmos. Sci.*, **64**, 2695–2706.

Son, S.-W., and L. M. Polvani, 2007: Dynamical formation of an extra-tropical tropopause inversion layer in a relatively simple general circulation model. *Geophys. Res. Lett.*, **34**, L17806, doi:10.1029/2007GL030564.

Son, S.-W., S. Lee, and S. B. Feldstein, 2007: Intraseasonal variability of the zonal-mean extratropical tropopause height. *J. Atmos. Sci.*, **64**, 608–620.

Son, S.-W., N. F. Tandon, and L. P. Polvani, 2011: The fine-scale structure of the global tropopause derived from COSMIC GPS radio occultation measurements. *J. Geophys. Res.*, submitted.

Stone, P. H., 1972: A simplified radiative-dynamical model for the static stability of rotating atmospheres. *J. Atmos. Sci.*, **29**, 405–418.

Thuburn, J., and G. C. Craig, 2000: Stratospheric influence on tropopause height: The radiative constraint. *J. Atmos. Sci.*, **57**, 17–28.

Thuburn, J., and G. C. Craig, 2002: On the temperature structure of the tropical substratosphere. *J. Geophys. Res.*, **107**, 4017, doi:10.1029/2001JD000448.

Tomikawa, Y., Y. Nishimura, and T. Yamanouchi, 2009: Characteristics of tropopause and tropopause inversion layer in the polar region. *SOLA*, **5**, 141–144.

Ueyama, R., and J. M. Wallace, 2010: To what extent does high-latitude wave forcing drive tropical upwelling in the Brewer-Dobson circulation? *J. Atmos. Sci.*, **67**, 1232 – 1246.

Virts, K. S., and J. M. Wallace, 2010: Annual, interannual, and intraseasonal variability of tropical tropopause transition layer cirrus. *J. Atmos. Sci.*, **67**, 3097–3112.

Webster, P. J., and J. R. Holton, 1982: Cross-equatorial response to mid-latitude forcing in a zonally varying basic state. *J. Atmos. Sci.*, **39**, 722–733.

Weickmann, K. M., G. N. Kiladis, and P. D. Sardeshmukh, 1997: The dynamics of intraseasonal atmospheric angular momentum oscillations. *J. Atmos. Sci.*, **54**, 1445–1461.

Wheeler, M. C., and H. H. Hendon, 2004: An all-season real-time multivariate MJO index: Development of an index for monitoring and prediction. *Mon. Wea. Rev.*, **132**, 1917–1932.

Wickert, J., and Coauthors, 2001: Atmosphere sounding by GPS radio occultation: First results from CHAMP. *Geophys. Res. Lett.*, **28**, 3263–3266.

Winker, D. M., W. H. Hunt, and M. J. McGill, 2007: Initial performance assessment of CALIOP. *Geophys. Res. Lett.*, **34,** L19803. doi:10.1029/2007GL030135.

Wirth, V., 2003: Static stability in the extratropical tropopause region. *J. Atmos. Sci.*, **60**, 1395 – 1409.

Wirth, V., and T. Szabo, 2007: Sharpness of the extratropical tropopause in baroclinic life cycle experiments. *Geophys. Res. Lett.*, **34**, doi:10.1029/2006GL028369.

WMO, 1957: Meteorology – A three dimensional science. *WMO Bull.*, **6**, 134– 138.

WMO, 1986: Atmospheric ozone 1985. World Meteorological Organization Global Ozone Research and Monitoring Project Rep. 16, Vol. I, WMO, Geneva, Switzerland, 240 pp.

Xu, K.-M., and K. A. Emanuel, 1989: Is the tropical atmosphere conditionally unstable? *Mon. Wea. Rev.,* **117,** 1471–1479.

Yulaeva, E., J. R. Holton, and J. M. Wallace, 1994: On the cause of the annual cycle in tropical lower-stratospheric temperatures. *J. Atmos. Sci.*, **51**, 169–174.

Zängl, G., and K. P. Hoinka, 2001: The tropopause in the polar regions. *J. Climate,* **14**, 3117–3139.

Zängl, G., and V. Wirth, 2002: Synoptic-scale variability of the polar and subpolar tropopause: Data analysis and idealized PV inversions. *Quart. J. Roy. Meteor. Soc.*, **128**, 2301–2315.

Zhang, C., 2005: Madden-Julian Oscillation. *Rev. Geophys.*, **43**, RG2003, doi:10.1029/2004RG000158.

Zhang, C., and H. H. Hendon, 1997: Propagating and standing components of the intraseasonal oscillation in tropical convection. *J. Atmos. Sci.*, **54**, 741–752.

Zhou, X. L., M. A. Geller, and M. H. Zhang, 2001: Tropical cold point tropopause characteristics derived from ECMWF reanalysis and soundings. *J. Climate*, **14**, 1823–1838.

APPENDIX A: STRATOSPHERIC DYNAMICS

The observed equator-to-pole temperature gradient in the stratosphere is much less than that predicted by radiative equilibrium (e.g., Andrews et al. 1987). This appendix reviews the relevant dynamics that cause the stratosphere to deviate from radiative equilibrium.

The deviation of the stratosphere from radiative equilibrium is primarily the result of the vertical propagation of Rossby waves (waves that conserve potential vorticity) into the stratosphere from the troposphere. However, only select Rossby waves are capable of reaching stratospheric levels under very specific conditions. Using quasi-geostrophic Beta-plane theory with a constant base state zonal wind u_0 and temperature, Charney and Drazin (1961) derived the following refractive index n^2 for the vertical propagation of Rossby waves:

$$n^2 = -\frac{1}{4H^2} - \frac{N^2}{f_0^{\,2}}\left\{(k^2 + l^2) - \frac{\beta}{u_0 - c}\right\} \qquad \text{(A.1)}$$

In (A.1), β is a constant mid-latitude value of Earth's planetary vorticity gradient, H is the atmospheric scale height, N^2 is the static stability (see equation 2.1), f_0 is a constant mid-latitude value of Earth's planetary vorticity, k is the zonal wavenumber of the Rossby wave, l is the meridional wavenumber of the Rossby wave, and c is the phase speed of the Rossby wave.

The vertical propagation of Rossby waves is only possible for $n^2 > 0$, so (A.1) is easier to interpret by solving for the phase speed relative stratospheric zonal wind $u_0 - c$ required to satisfy $n^2 > 0$:

$$0 < u_0 - c < \frac{\beta}{(k^2 + l^2) + f_0^{\,2}/(4H^2N^2)} \equiv U_c \qquad \text{(A.2)}$$

The results in (A.2) reveal that the phase speed relative stratospheric zonal wind must be westerly ($u_0 - c > 0$) but less than a certain critical value ($u_0 - c < U_c$) for a Rossby wave to propagate vertically into the stratosphere. Because U_c is inversely related to wavenumber, large wavenumber (small wavelength) Rossby waves, such as those associated with synoptic-scale baroclinic eddies, rarely satisfy (A.2). Thus, only planetary-scale Rossby waves typically reach stratospheric levels. Such planetary waves are usually quasi-stationary ($c \approx 0$) and are generated by topography and large-scale land-sea temperature contrast.

The Charney and Drazin (1961) condition is only met during select seasons. During the summer months, continuous sunlight at the pole supports substantial absorption of shortwave radiation by ozone and warms the summer pole more than the Equator. Consequently, easterly shear develops with height in the stratosphere (as expected from thermal wind balance), and the stratospheric easterlies preclude the vertical propagation of planetary waves into the stratosphere. Likewise, during the winter months, the absence of sunlight at the pole supports the presence of stratospheric westerlies (i.e., the stratospheric polar vortex) and the vertical propagation of planetary waves into the stratosphere.

As discussed below, the presence of planetary waves in the wintertime stratosphere serves to damp the westerly zonal mean flow and reduce the meridional temperature gradient. Thus, because of the greater topography and land-sea temperature contrast in the Northern Hemisphere, the aggregate influence of the planetary waves supports a weaker mean stratospheric polar vortex than in the Southern Hemisphere. Consequently, the mean stratospheric polar vortex in the Northern Hemisphere is weak enough to satisfy the Charney and Drazin (1961) criterion during the entire winter season, whereas the mean stratospheric polar vortex in the Southern Hemisphere is only weak enough during the late spring-early summer and fall. (In observations, the Southern Hemisphere polar vortex is rarely affected by planetary wave forcing during the fall season because it tends to be very broad, encompasses a substantial amount of atmospheric mass, and therefore is less affected by a given wave forcing (McIntyre 1982).)

So, how exactly does a vertically propagating planetary wave influence the zonal mean flow and temperatures in the stratosphere? As a planetary wave propagates upward through the stratosphere, it increases in amplitude as the surrounding ambient density decreases. Eventually, the wave reaches an altitude at which its amplitude becomes large enough for nonlinear effects to dominate, and the wave breaks and causes irreversible displacements, filamentation, and even splitting of the polar vortex (Haynes 2005). These deformations of the polar vortex are usually associated with a sudden stratospheric warming, a dramatic warming of the winter pole in the stratosphere (sometimes 40 K or more at 50 hPa) over the period of a few days (e.g., McIntyre 1982). Consistent with thermal wind balance, the rapid warming of the pole is associated with a rapid weakening of the stratospheric zonal-mean zonal flow, which in some cases can reverse its orientation to easterly.

To understand why planetary wave breaking in the stratosphere is associated with polar warming and a weakening of the stratospheric zonal flow, the conventional Eulerian mean zonal momentum and thermodynamic equations can be interpreted within the context of wave-mean flow interaction theory. The equations are again derived from quasi-geostrophic Beta-plane theory and use log-pressure ($z = -H \ln(p/p_s)$) as the vertical coordinate. Following the notation in Holton (2004), overbars denote a zonal mean, and primes denote deviations (eddies) from that zonal mean.

$$\frac{\partial \overline{u}}{\partial t} - f_0 \overline{v} = -\frac{\partial (\overline{u'v'})}{\partial y} + \overline{X} \qquad \text{(A.3)}$$

$$\frac{\partial \overline{T}}{\partial t} + N^2 H R^{-1} \overline{w} = -\frac{\partial (\overline{v'T'})}{\partial y} + \overline{J}/c_p \qquad \text{(A.4)}$$

The conventional Eulerian mean zonal momentum equation (A.3) describes a steady-state balance between the Coriolis force, eddy momentum flux convergence, and friction; the conventional Eulerian mean thermodynamic equation (A.4) describes a steady-state balance between adiabatic temperature changes due to vertical motion, eddy heat flux convergence, and diabatic effects.

In practice, the conventional Eulerian mean equations are cumbersome for assessing temperature changes because of the near cancellation of the vertical motion and eddy heat flux terms in (A.4). So, an algebraic manipulation of (A.3) and (A.4) known as the transformed Eulerian mean (TEM) is often used to shift the effects of the eddy heat flux into the zonal momentum equation.

$$\frac{\partial \overline{u}}{\partial t} - f_0 \overline{v}^* = \rho_0^{-1} \nabla \cdot \mathbf{F} + \overline{X} \qquad \text{(A.5)}$$

$$\frac{\partial \overline{T}}{\partial t} + N^2 H R^{-1} \overline{w}^* = \overline{J} / c_p \qquad \text{(A.6)}$$

$$F_y = -\rho_0 \, \overline{u'v'} \qquad F_z = \rho_0 f_0 R \overline{v'T'} / (N^2 H) \qquad \text{(A.7)}$$

(A.5) is the TEM zonal momentum equation, (A.6) is the TEM thermodynamic equation, and (A.7) is the definition of the Eliassen-Palm (EP) flux vector **F**. The meridional component of the EP flux vector is proportional to the southward eddy momentum flux, and the vertical component of the EP flux vector is proportional to the poleward eddy heat flux.

The TEM equations (A.5)–(A.7) describe a mean meridional circulation (residual circulation) in which the vertical motion $\overline{w}^*$ is only governed by diabatic effects in the steady state. All effects of eddies are confined to the divergence of the EP flux, which induces a westerly acceleration on the zonal-mean zonal flow where it is positive. The divergence of the EP flux is zero for steady, conservative waves (e.g., Edmon et al.

1980). So, in order for eddies to have any irreversible effect on the atmosphere, there must be wave transience, wave dissipation, or both. (Increasing wave activity and wave dissipation are associated with EP flux convergence.) Thus, planetary wave breaking in the stratosphere can be thought of either as irreversible deformations of the polar vortex or as simply EP flux convergence.

Using the TEM framework, the influence of planetary waves on the stratosphere can be summarized as follows. Vertically propagating planetary waves exert an easterly force (EP flux convergence) on the stratospheric zonal flow as they break in the extratropical stratosphere. Initially, the introduction of the EP flux convergence induces two meridional circulation cells of opposite orientation, one above and one below the forcing region. As the system approaches steady state, the upper circulation cell damps away, and the lower circulation cell shrinks meridionally and expands vertically (Haynes et al. 1991; Haynes 2005). Consequently, the steady-state residual circulation is confined directly below the EP flux convergence region, a principle that is commonly referred to as “downward control.”

The residual circulation associated with the planetary wave breaking in the extratropical stratosphere is characterized by rising motion and adiabatic cooling equatorward of the wave forcing and sinking motion and adiabatic warming poleward of the forcing. Thus, as planetary wave breaking weakens the stratospheric zonal flow, the resulting residual circulation reduces the meridional temperature gradient to maintain thermal wind balance. From this perspective, the meridional overturning circulation induced by planetary wave breaking in the extratropical stratosphere causes the stratosphere to deviate from radiative equilibrium.

APPENDIX B: EQUATORIAL PLANETARY WAVE DYNAMICS

Equatorial planetary waves dominate the climatological-mean tropical general circulation and are characterized by an equatorially trapped Rossby wave response to the west of a region of localized convective heating and a Kelvin wave response to the east of the heating. Why is this equatorial wave pattern so favorable in the atmosphere? This appendix examines key solutions of the shallow water equations on an equatorial Beta plane to provide some theoretical perspective.

The shallow water equations on an equatorial Beta plane are given by (B.1) – (B.3), where ϕ is the geopotential height and c is a constant gravity wave phase speed based on the mean fluid depth (e.g., Matsuno 1966). The equations have been linearized about a basic state of rest and represent the shallow water versions of the horizontal momentum and continuity equations.

$$\frac{\partial u}{\partial t} - \beta y v + \frac{\partial \phi}{\partial x} = 0 \tag{B.1}$$

$$\frac{\partial v}{\partial t} + \beta y u + \frac{\partial \phi}{\partial y} = 0 \tag{B.2}$$

$$\frac{\partial \phi}{\partial t} + c^2\left(\frac{\partial u}{\partial x} + \frac{\partial v}{\partial y}\right) = 0 \tag{B.3}$$

Following Matsuno (1966), the equations are non-dimensionalized using a length scale of $(c/\beta)^{1/2}$ and a time scale of $(1/c\beta)^{1/2}$:

$$\frac{\partial u}{\partial t} - yv + \frac{\partial \phi}{\partial x} = 0 \tag{B.4}$$

$$\frac{\partial v}{\partial t} + yu + \frac{\partial \phi}{\partial y} = 0 \tag{B.5}$$

$$\frac{\partial \phi}{\partial t} + \frac{\partial u}{\partial x} + \frac{\partial v}{\partial y} = 0 \tag{B.6}$$

The steady-state response of (B.4)–(B.6) to a localized forcing Q is given by the solution of (B.7)–(B.9). Here, Q represents an imposed diabatic heating rate from localized convection. To aid in the solution, damping terms with timescale ε have been added into the momentum and continuity equations to represent Rayleigh friction and Newtonian cooling, respectively.

$$\varepsilon u - yv + \frac{\partial \phi}{\partial x} = 0 \tag{B.7}$$

$$\varepsilon v + yu + \frac{\partial \phi}{\partial y} = 0 \tag{B.8}$$

$$\varepsilon \phi + \frac{\partial u}{\partial x} + \frac{\partial v}{\partial y} = -Q \tag{B.9}$$

A solution of (B.7)–(B.9) for a localized region of diabatic heating centered on the Equator is shown in Figure B.1 (from Gill 1980). Figure B.1 depicts the lower tropospheric pressure and wind responses. The solution has a simple baroclinic structure, so the upper tropospheric pressure and wind responses are of opposite sign to those in Figure B.1.

To the east of the heating region (centered at $x = 0$, $y = 0$), the solution in Figure B.1 resembles an equatorial Kelvin wave with lower tropospheric easterly flow to the east of the heating region. The Kelvin wave response is characterized by 1) pure gravity wave momentum balance in the zonal direction (i.e., the flow is directed toward the lowest pressure in the heating region) and 2) geostrophic balance in the meridional direction (i.e., the pressure minimizes on the Equator at each longitude to the east of the heating region). Thus, the Kelvin wave response in Figure B.1 is allowed by the change in sign of Earth's planetary vorticity across the Equator. Note that the Kelvin wave response damps out to the east of the heating region, consistent with the damping timescale ε and the phase speed of the Kelvin wave.

To the west of the heating region, the solution in Figure B.1 resembles an equatorially trapped Rossby wave with lower tropospheric cyclones positioned to the northwest and southwest of the heating region. The Rossby wave response is nearly non-divergent and geostrophic and is characterized by strong equatorial westerly flow into the heating region. Because the phase speed of the Rossby wave is ~1/3 of that of the Kelvin wave, the Rossby wave response in Figure B.1 extends only ~1/3 of the distance from the heating center as the Kelvin wave response.

Within the heating region, the solution in Figure B.1 describes the superposition of the Rossby and Kelvin wave patterns. The equatorial zonal winds associated with the Rossby and Kelvin wave responses converge into the heating region, so the heating region is characterized by rising motion that maximizes in the mid-troposphere (not shown). But surprisingly, the meridional winds in the heating region are poleward and diverge from the Equator.

The lower tropospheric poleward flow in the heating region is implied from the shallow water vorticity equation (B.10), which can be derived from (B.7) and (B.8) in the limit of no damping.

$$y\left(\frac{\partial u}{\partial x}+\frac{\partial v}{\partial y}\right)+v=0 \tag{B.10}$$

(B.10) can be rewritten as (B.11), using (B.9) in the limit of no damping.

$$v = yQ \tag{B.11}$$

Or in dimensional form:

$$\beta v = f\frac{\partial w}{\partial z} \tag{B.12}$$

(B.11) and (B.12) indicate that vortex stretching in the lower troposphere (i.e., $Q > 0$) must be balanced by the poleward advection of Earth's planetary vorticity. Note that this relationship is analogous to Sverdrup balance in oceanographic contexts.

Overall, the results in Figure B.1 strongly resemble the observed pattern of equatorial planetary waves during seasons when the climatological distribution of convective heating is centered on the Equator (e.g., Dima et al. 2005; Dima and Wallace 2007). In seasons when the climatological convective heating is centered off the Equator (e.g., Northern Hemisphere summer), the solution of (B.7)–(B.9) produces an equatorial planetary wave response that is more hemispherically asymmetric (see Gill 1980).

Although the shallow water equations provide a first-order theoretical understanding of the observed equatorial planetary wave pattern, the results presented in this appendix are highly idealized. In the real atmosphere, tropical convective heating is not specified but rather results from complicated feedbacks between convection, moist processes, air-sea interaction, and the general circulation. Additionally, equations linearized about a basic state of rest cannot be strictly used to interpret the basic state of the tropical general circulation. Nonetheless, Figure B.1 provides a useful paradigm through which to interpret the results of this dissertation.

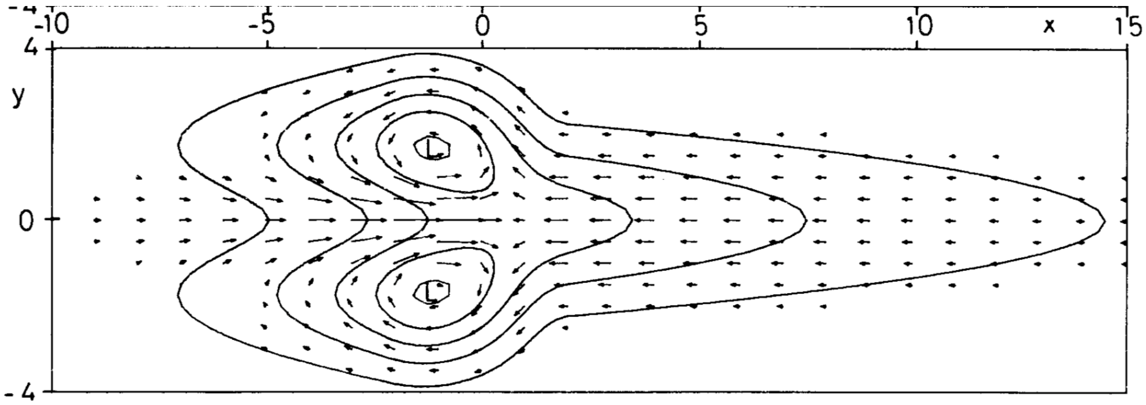

Figure B.1: (from Gill 1980) Steady-state solution of the shallow water equations on an equatorial Beta plane to an imposed heating centered at $x = 0$ and $y = 0$. The contours represent negative values of lower tropospheric pressure, and the vectors represent lower tropospheric winds.